AN INFRARED RADIOMETER FOR MILLIMETER ASTRONOMY

GRAEME JOHN SMITH

B. Sc. Physics, University of Lethbridge, 1999

A Thesis
Submitted to the Council on Graduate Studies
of the University of Lethbridge
in Partial Fulfilment of the
Requirements of the Degree

MASTER OF SCIENCE

LETHBRIDGE, ALBERTA
DECEMBER, 2000

Abstract

The performance of existing and planned millimeter and submillimeter astronomical arrays is limited by fluctuations in the amount of atmospheric water vapor along the antenna's line of sight. Correcting the resulting phase distortion of the received signals is seen as a significant technological challenge. Measurements of the variation in the line-of-sight water vapor abundance at the level of 1 micron precipitable water vapor on a time scale of 1 second and at arbitrary antenna positions are required. This thesis describes the design of, and preliminary results obtained with, a water vapor monitor operating at infrared wavelengths which shows considerable promise for this application. Improvements in, and future plans for, the second generation water vapor monitor currently under development is also discussed.

Contents

List of Figures

List of Tables

Chapter 1

Introduction

1.1 Overview

The 21^{st} century will see the introduction of very large baseline millimeter wavelength radio telescope interferometers that are capable of resolving features on the order of milli-arcseconds. As these telescopes operate on the principle of interferometry, they must accurately measure the time delay between reception of various parts of an electromagnetic wavefront at different antennae composing the radio telescope array. Any variation in the propagation speed of an electromagnetic wave on its way to the antenna array, due to atmospheric inhomogeneities, will distort the wavefront and lead to misinterpretation of the signals from astronomical sources. The electronic instrumentation has advanced to the point where the factor which now limits the attainable spatial resolution of large millimeter radio interferometers is the variation in the line-of-sight water vapor abundance which causes variations in the electromagnetic path length and hence interferometric phase.

Previous approaches to atmospheric phase compensation include the *fast switching* and *paired array* techniques [1]. In the *fast switching* approach, a radio antenna is repeatedly moved from the astronomical target source to a nearby calibration point source such as a quasar. Observed deviations of this point source from the expected circular symmetry of the Airy diffraction profile then correspond to atmospheric phase distortions which can be determined and compensated for in the signals from the target source. This approach has the advantage of giving a true measure of phase distortion since the quasar is known to be a point source. If every antenna of the array is switched in this way, then the phase error for each can be determined. There are several drawbacks to this approach, however. The calibration measurements are done along a different line-of-sight than that of the target source and hence involve different atmospheric paths. Observations of the target source are therefore interrupted by the calibration measurements and, since suitable calibration sources may not be available close to the target source, this process may result in long calibration cycles during which the atmosphere is assumed to be stable.

In the *paired array* approach, observation of the calibration point source is done on a continuous basis with a few of the antennae comprising the array; this avoids interrupting the observation of target source incurred with the *fast switching* approach. Once again, however, the line-of-sight used to obtain the phase error information differs from that of the target source. Furthermore, at a cost of ~$10 million per antenna, dedication of even a small number of antennae to phase compensation represents an expensive solution to the problem.

Due to the dominant role of water vapor in the phase delay of electromagnetic

radiation, a new approach has been developed for astronomical phase correction which uses multi-channel radiometric observation of the 183 GHz water vapor emission line [2]. In this approach the radio telescope antenna is used for simultaneous observation of astronomical sources and atmospheric water vapor emission. This technique offers the advantage of sampling the water vapor emission from the same atmospheric column that the astronomical signals pass through and may be implemented at every antenna in the array. The drawbacks in this case are the risk of introduction of radio frequency noise due to the presence of a local oscillator in the telescope receiver cabin and the relatively low signal levels due to a small spectral bandwidth (1 GHz) of each radiometric channel and the inherently low radiant emission of the atmosphere in this spectral region.

This thesis describes an infrared technique for measuring water vapor column abundance and presents the results from the trial run of a prototype instrument constructed at the University of Lethbridge and tested at the James Clerk Maxwell Telescope (JCMT) on Mauna Kea in December of 1999. This passive mode of observing atmospheric water vapor emission poses no threat of radio frequency interference to an astronomical receiver and takes advantage of a wider spectral bandwidth and greater radiant emission from atmospheric water vapor in the infrared region. Use of a liquid nitrogen (LN_2) cooled photoconductive detector provides both high sensitivity and high operating speed .

Section 1.2 describes the relationship between atmospheric water vapor abundance and electromagnetic path length variation and gives a formula for this conversion. Section 1.3 details the benefits of measuring water vapor in the infrared and contrasts this approach with radio frequency radiometric techniques while Section 1.4 lists some potential draw-

backs. Section 1.5 presents a calculation of temporal resolution. Section 1.6 discusses the phase compensation requirements of the Atacama Large Millimeter Array (ALMA) which is representative of the new generation of large millimeter wavelength interferometers.

1.2 Tropospheric Phase Delay

The troposphere is the lowest layer of the atmosphere; it extends to an altitude of approximately 10 km and contains, besides the major constituents N_2 and O_2, various trace gases such as H_2O, CO_2 and N_2O. Due to the decreasing temperature in this layer, water vapor exists primarily at low altitudes, but yet in concentrations great enough to contribute to phase delay even from high altitude observing sites such as Mauna Kea, Hawaii (~ 4000 m) and Chajnantor, Chile (~ 5000 m).

Due to their large dipole moment and asymmetric top geometry, water vapor molecules interact with electromagnetic radiation throughout the submillimeter and infrared spectral regions, becoming particularly important at wavelengths below 1 cm. The resulting absorption, and hence phase delay as expressed by the Kramers-Kronig relation [3], increases the refractive index of the atmosphere from unity, and must be accounted for if diffraction limited performance is to be obtained from large radio interferometer arrays. If tropospheric water vapor was well mixed, the phase delay of an electromagnetic wave passing through the atmosphere would be constant across its wavefront resulting only in a uniform signal attenuation and phase delay. Due to complex hydrodynamic processes, variable tropospheric temperatures and the ability of water to exist in all three phases in the lower atmosphere,

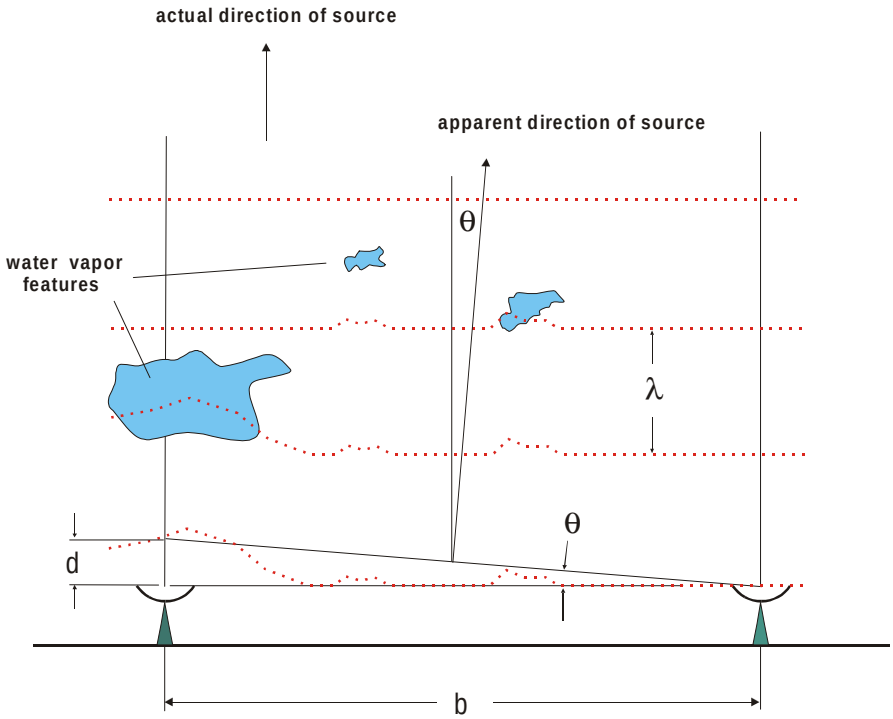

Figure 1.1: Variations in atmospheric water vapor abundance cause distortion in the wavefront of an electromagnetic wave.

however, the concentration of tropospheric water vapor is highly variable even over small distances ($\sim$ m) and short time intervals ($\sim$ s). This variability poses a problem for the upcoming generation of large radio telescope arrays, such as ALMA, with baselines on the order of 10 km. If the amount of water vapor above each antenna of an array can be measured accurately and rapidly, then its effects on phase variations, and hence interferometer angular resolution, can be compensated.

Figure 1.1 shows an illustration of the phase delay produced by variations in water vapor density in the atmosphere above a dual element radio interferometer. Using the quantities shown in the figure, the instantaneous apparent angular location of an astronomical source, θ, as determined by the radio interferometer can be expressed in terms of

the baseline of the interferometer, b, and the additional electromagnetic path length, d, or, equivalently, the phase change of the electromagnetic wave, ϕ, caused by water vapor through

$$\theta = \frac{d}{b} = \frac{\phi\lambda}{2\pi b} \tag{1.2.1}$$

where ϕ is in radians. The phase change, ϕ, of an electromagnetic wave of wavelength λ due to propagation through an atmosphere characterized by an altitude dependent refractive index due to water vapor, $n_{H_2O}(h)$, is given by

$$\phi = \frac{2\,\pi \int_0^\infty n_{H_2O}(h)\; dh}{\lambda} \tag{1.2.2}$$

which can be written as

$$\phi = \frac{2\,\pi \langle n \rangle_{H_2O}\, h_{atm}}{\lambda} \tag{1.2.3}$$

using an average atmospheric index of refraction due to water vapor $\langle n \rangle_{H_2O}$ and effective atmospheric height h_{atm}. From equation 1.2.1, the corresponding additional electromagnetic path length due to water vapor, d, is then

$$d = \frac{\lambda\,\phi}{2\,\pi} = \langle n \rangle_{H_2O}\, h_{atm} \tag{1.2.4}$$

The angular resolution of a radio interferometer depends on the degree to which the phase relationship between the signals from different antennae can be resolved. Using the above relationships, rms variations in the perceived direction of a source, θ_{rms}, can be given in terms of an equivalent rms phase noise, ϕ_{rms}, or equivalently, an rms path length variation, d_{rms}, specified at a given operating wavelength.

Since changes in the refractive index of the atmosphere at microwave frequencies are due to variations in atmospheric water vapor abundance, the excess electromagnetic path length, d, has been related to the vertical column abundance of water vapor, w, expressed in units of millimeters of precipitable water vapor (mmpwv) by [1] :

$$d = \frac{1.7\times10^3}{T_{atm}} \times w \qquad 1.2.5$$

where T_{atm} is the average temperature of the atmosphere in K. For an atmospheric temperature of $260\,K$, the excess path becomes

$$d \simeq 6.5 \times w \qquad 1.2.6$$

and, using equation 1.2.4, the associated wavelength dependent phase variation is then

$$\phi = \frac{13\pi}{\lambda} \times w \qquad 1.2.7$$

This conversion factor has been verified experimentally for astronomical purposes [4] and is now in widespread use in the radio-astronomical community [5].

1.3 Advantages of an Infrared Approach

A necessary requirement for the accurate radiometric measurement of atmospheric water vapor abundance at infrared wavelengths is for water vapor emission to be spectrally isolated from other infrared active atmospheric molecular species. Previous measurements taken from the summit of Mauna Kea have shown that atmospheric emission in the 20 μm

($\sim 500\,\mathrm{cm}^{-1}$) spectral region is due to water vapor alone and evidence in support of this claim is included in this section.

An infrared approach to water vapor measurement is attractive for several reasons. Firstly, since strongly absorbing atmospheric molecular species emit as blackbody radiators, the spectral radiance from atmospheric water vapor is far greater at infrared wavelengths than at radio frequencies as can be seen by evaluating the Planck formula at typical atmospheric temperatures. Secondly, considering the simple case where the flux available to a radiometer (infrared or radio frequency) is proportional to the integral of spectral radiance over a spectral range defined by the bandpass of the system, the total flux available to an infrared system is much greater since it uses a spectral bandwidth several orders of magnitude larger than radio frequency systems. This increased flux can then be translated into more sensitive measurements, faster operation, smaller instrument size or some combination thereof as compared to radio frequency radiometers. Thirdly, photoconductive detectors operating at infrared wavelengths offer high operating speeds, stability, and simple instrumentation. Finally, as previously mentioned, an infrared radiometer is an entirely passive device and is free of radio frequency interference. It may thus be placed in close proximity to sensitive radio frequency instrumentation without risk of noise induction.

In view of the above considerations, an infrared approach to water vapor measurement is expected to yield a sensitive, high speed and compact device which can easily be incorporated on both existing and future radio telescope antennae.

1.3.1 Spectral Isolation of Water Vapor Emission

In order to measure water vapor abundance radiometrically it is essential to select a spectral range in which water vapor alone contributes to atmospheric emission and, if possible, to have that region near the peak of the Planck curve to maximize the sensitivity of the observations. Infrared atmospheric emission above the summit of Mauna Kea has previously been measured using a Fourier transform spectrometer [6] over the spectral range 455 to 635 cm^{-1}. Figure 1.2 is an excerpt from these data and shows the emission from 455 to 516 cm^{-1} (lowest curve) and computer simulated emission from N_2O, CO_2 and H_2O (upper three curves) modeled for the atmosphere above Mauna Kea. The water vapor column abundance during acquisition of the measured spectra was 0.43 mm pwv and the column abundance parameters used for the synthetic emission spectrum of N_2O, CO_2 and H_2O were $2.67 \times 10^{-3}\,\mathrm{kg\,m^{-2}}$, $3.20\,\mathrm{kg\,m^{-2}}$, and $0.83\,\mathrm{kg\,m^{-2}}$, respectively.

As seen from the figure, there is an absence of emission from CO_2 and N_2O for the entire spectral region shown and, furthermore, the measured atmospheric emission spectra are well described by emission from H_2O alone. Since, as shown in the following section, this region lies near the peak of the Planck curve for an atmospheric temperature of $\sim 260\,\mathrm{K}$, it is a prime spectral region in which to conduct water vapor radiometry, provided the necessary optical components (filters and detectors) can be obtained.

A secondary consideration in the selection of a spectral range is the degree of saturation of the emission lines. As described in Chapter 2, unsaturated lines give the most sensitivity to water vapor column abundance since the integrated line intensity grows

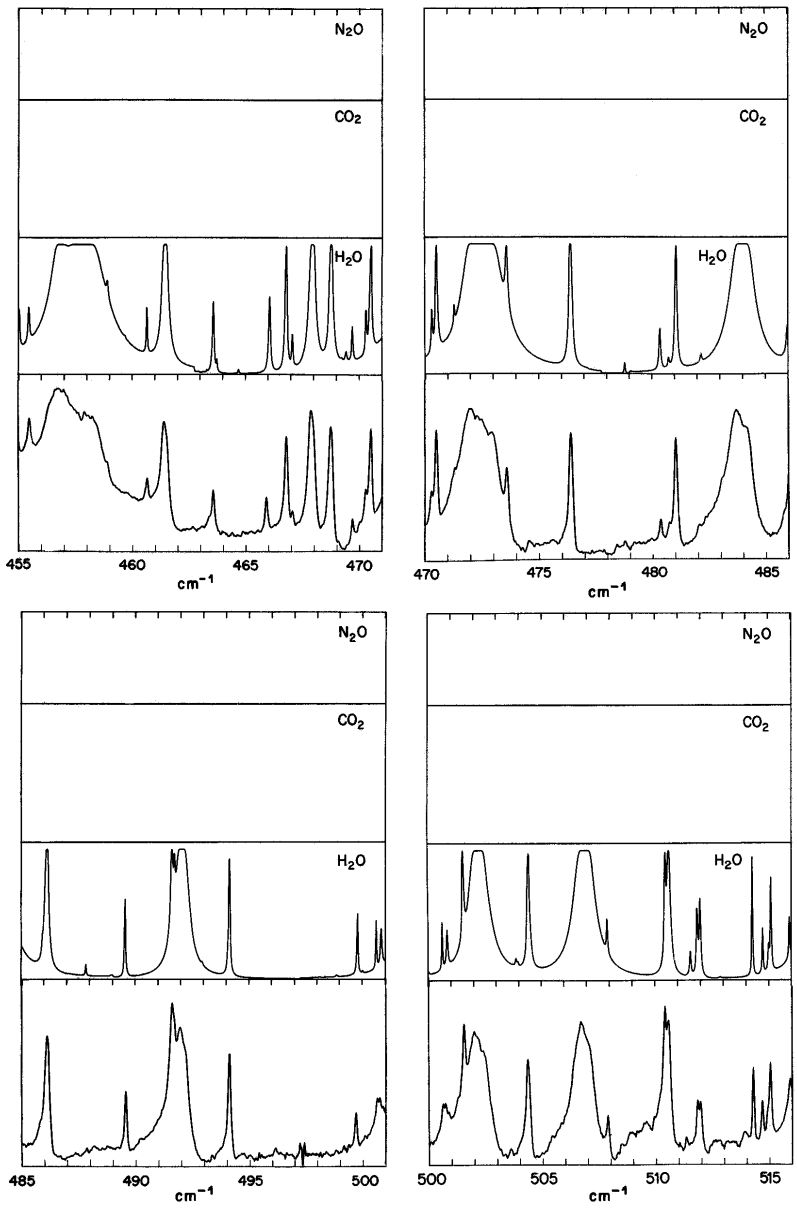

Figure 1.2: Measured and computer simulated infrared atmospheric emission above Mauna Kea showing the spectral isolation of water vapor in the spectral region near $\sigma = 500$ cm^{-1} ($\lambda = 20$ μm). Upper three curves are computer simulated emission from N_2O, CO_2 and H_2O using column abundances of 2.67×10^{-3} kg m^{-2}, 3.20 kg m^{-2} and 0.83 kg m^{-2}, respectively. The lowest curve is the measured atmospheric emission under conditions of 0.43 mm *pwv*..

approximately linearly with abundance in this regime. After the onset of saturation, on the other hand, the integrated line intensity exhibits a square root dependence on water vapor abundance corresponding to growth primarily in the wings of the line. The use of a spectral range containing as many unsaturated lines as possible is then desirable for high sensitivity water vapor radiometry. As described in Chapter 3, the infrared filter available for the prototype radiometer had a spectral passband of $462 - 505$ cm^{-1}; as seen from Figure 1.2, although this region contains a mixture of both weak and strong absorption features, the majority are unsaturated and hence this region is well suited to the sensitive radiometric measurement of water vapor.

1.3.2 Radio Frequency Interference

The heterodyne detection occurring in radio frequency water vapor monitors requires the presence of a local oscillator. Since the mixing process is nonlinear and the local oscillator signal is strong compared to astronomical sources, there is a risk of radio frequency interference with other heterodyne receivers mounted on the telescope. An infrared radiometer, on the other hand, uses a DC biased photoconductor operating in a passive mode, and thus generates no radio frequency interference. The highest modulating frequency occurring in the prototype infrared radiometer was the 200 Hz chopping frequency of the optical chopper.

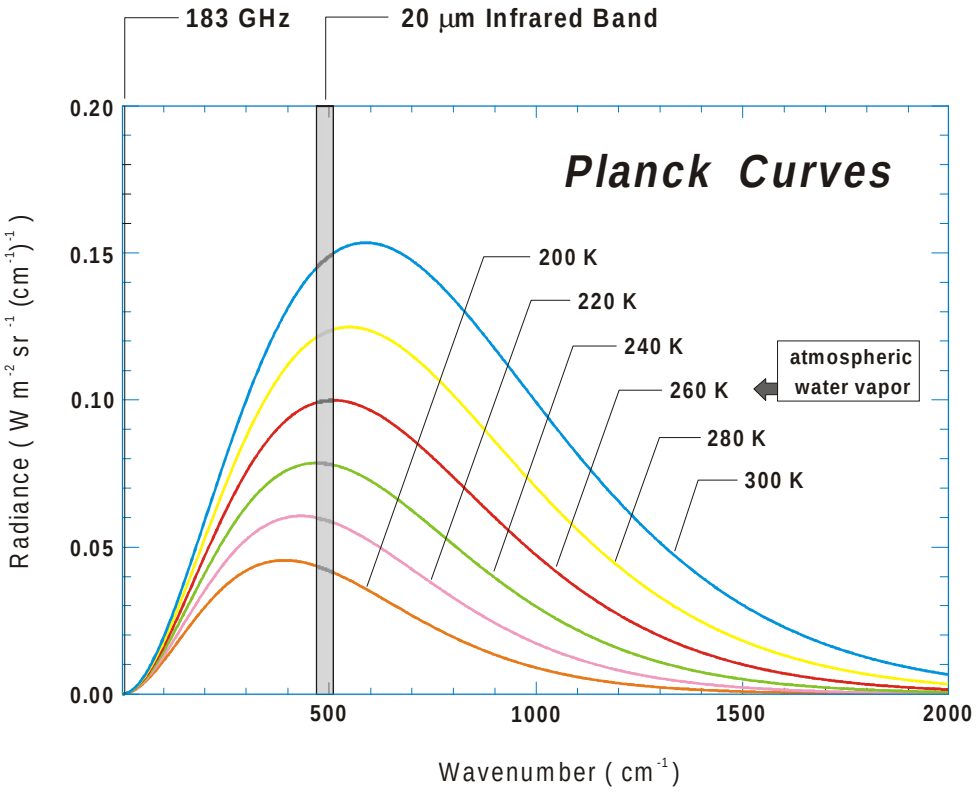

Figure 1.3: Blackbody emission curves evaluated for a range of atmospheric temperatures.

1.3.3 Radiance Comparison

The total flux, Φ, in Watts, collected by a water vapor radiometer is the product of the throughput, $A\,\Omega$, and the radiance, L:

$$\Phi = A\,\Omega\,L \tag{1.3.1}$$

where A is the aperture area, Ω is the solid angle of acceptance of the aperture and L is the spectral radiance of water vapor integrated over the spectral bandpass of the system under consideration. Although atmospheric water vapor emission as measured by both a

183 GHz and 20 μm infrared radiometer will not be fully saturated for column abundances on the order of $\sim 1\,\mathrm{mm}\,pwv$, saturated emission will be assumed for the comparison of the two systems. In this case the spectral radiant emission from atmospheric water vapor will be given by the Planck function,

$$L_\sigma\left(T_{atm}\right) = B_\sigma\left(T_{atm}\right) = \left(2\ h\ c^2\ 100^4\ \sigma^3\right)\left(e^{\frac{hc100\sigma}{kT_{atm}}} - 1\right)^{-1} \tag{1.3.2}$$

with units of $\mathrm{W\,m^{-2}\,sr^{-1}(cm^{-1})^{-1}}$ and where T_{atm} is the temperature of the atmosphere in K and σ is wavenumber in $\mathrm{cm^{-1}}$.

As shown in Figure 1.3, at typical atmospheric temperatures of $\sim 260\,\mathrm{K}$, maximum emission occurs at a wavelength of $\sim 20\,\mu$m ($500\,\mathrm{cm^{-1}}$) and is approximately three orders of magnitude greater than at radio frequencies. For example, for an atmospheric temperature of 260 K, the Planck spectral radiances at $500\,\mathrm{cm^{-1}}$ and $6.1\,\mathrm{cm^{-1}}$ (183 GHz) are

$$L_{500\,cm^{-1}} = 9.98 \times 10^{-2}\ \mathrm{W\,m^{-2}sr^{-1}(cm^{-1})^{-1}} \tag{1.3.3}$$

$$L_{6.1\,cm^{-1}} = 7.87 \times 10^{-5}\ \mathrm{W\,m^{-2}sr^{-1}(cm^{-1})^{-1}} \tag{1.3.4}$$

and hence

$$\frac{L_{500\,cm^{-1}}}{L_{6.1\,cm^{-1}}} = 1270 \tag{1.3.5}$$

Offsetting the advantage of the greater spectral radiance available in the infrared is the fact that water vapor monitors operating at radio frequencies use the antenna dish itself as the collecting aperture; using the 15 m diameter JCMT antenna as an example, the collecting area is

$$A_{GHz} = \frac{\pi \cdot 15^2}{4} = 176 \text{ m}^2 \tag{1.3.6}$$

The prototype instrument described in this thesis, on the other hand, was constructed with a primary optic 125 mm in diameter. The collecting area in this case is

$$A_{IR} = \frac{\pi\,(0.125)^2}{4} = 1.23 \times 10^{-2} \text{ m}^2 \tag{1.3.7}$$

and the collecting area of the radio dish is seen to be $\sim 14,300$ times larger.

As discussed in Section 3.1, the field of view of the prototype radiometer provided sampling of a 10 m patch of atmosphere at a range of 1 km and thus corresponds to a solid angle of

$$\Omega = \frac{A}{r^2} = \frac{\pi d^2}{4r^2} = \frac{\pi(10)^2}{4(1000)^2} = 7.9 \times 10^{-5} \text{ sr} \tag{1.3.8}$$

Assuming the 183 GHz ($\lambda = 1.6$ mm) system operates at the diffraction limit of the JCMT antenna, the field of view of the antenna subtends an angle

$$\theta = \frac{1.22\ \lambda}{d} = \frac{1.22\,(1.6 \times 10^{-3})}{15} = 1.3{\times}10^{-4} \text{ rad} \tag{1.3.9}$$

corresponding to a solid angle of

$$\Omega = \frac{\pi\,\theta^2}{4} = \frac{\pi\,(1.3{\times}10^{-4})^2}{4} = 1.3{\times}10^{-8} \text{ sr} \tag{1.3.10}$$

Given the large focal length of typical radio telescopes, however, the water vapor emitting region will occur in the near field and the solid angle given in equation 1.3.10 will not be valid. Calculation of the field of view of the radio antenna in this case will depend

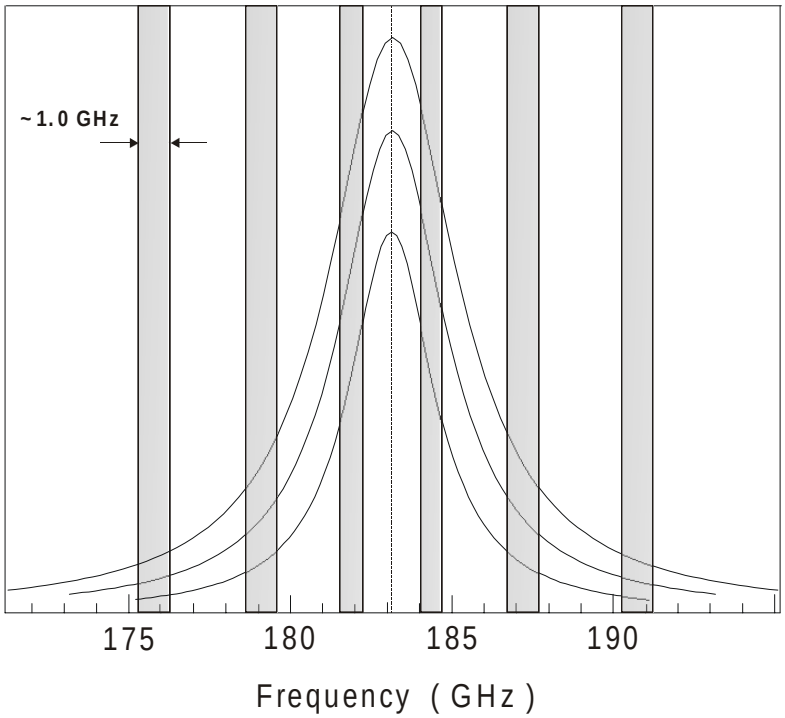

Figure 1.4: The radio frequency approach to measuring the emission of the 183 GHz water vapor line uses six discrete channels placed along the emission profile, each of which provides a different sensitivity under various degrees of line saturation.

upon the height of the emitting region and, while difficult to evaluate, will tend to approach the solid angle given by equation 1.3.8.

Assuming the water vapor emits as a blackbody, the integrated radiance is given by

$$L = \int_{\sigma_{lower}}^{\sigma_{upper}} L_\sigma \, d\sigma = \int_{\sigma_{lower}}^{\sigma_{upper}} B_\sigma \, d\sigma \qquad 1.3.11$$

which can be approximated as $L = B_\sigma \, \Delta\sigma = B_\sigma(\sigma_{upper} - \sigma_{lower})$ if the spectral radiance is considered constant over $d\sigma$.

The spectral bandwidth of the prototype infrared radiometer as defined by the

infrared filter was $\sim 450 - 500$ cm^{-1}, and thus $\Delta\sigma = 50\,\text{cm}^{-1}$.

In the 183 GHz radio frequency approach, the water vapor radiance is measured in several discrete frequency channels placed along the line profile, each on the order of 1.0 GHz (3.33×10^{-2} cm^{-1}) wide, as shown in Figure 1.4. The water vapor abundance is then inferred using computer models from the observed radiances in these channels, taken either individually or in combination [2]. A single measurement of water vapor abundance in this approach is thus obtained using a spectral bandwidth of $\Delta\sigma = 3.33 \times 10^{-2}$ cm^{-1}.

Using the Planck spectral radiance at 183 GHz calculated above and assuming it to be constant over the spectral bandwidth, the flux available to the 183 GHz system for a single water vapor abundance measurement is then on the order of

$$\begin{aligned}\Phi_{183\,\text{GHz}} &= A\,\Omega\,L_{183\,\text{GHz}}\,\Delta\sigma \\ &= (176)(7.9 \times 10^{-5})(7.87 \times 10^{-5})(3.33 \times 10^{-2}) \\ &= 3.6 \times 10^{-8}\ \text{W}\end{aligned} \tag{1.3.12}$$

where, as discussed above, the solid angle is taken as the same as that of the infrared system. On the other hand, the flux available to the infrared radiometer is

$$\begin{aligned}\Phi_{IR} &= A\,\Omega\,L_{500\,\text{cm}^{-1}}\Delta\sigma \\ &= (0.0123)(7.9 \times 10^{-5})(9.98 \times 10^{-2})(50) \\ &= 4.85 \times 10^{-6}\ \text{W}\end{aligned} \tag{1.3.13}$$

The above calculations are only approximate since the radiances are overestimated in both cases (the water vapor emission in reality will not be fully saturated over either

spectral bandwidth) and system efficiencies and modulation factors have not been taken into account. Even so, the total flux available to an infrared radiometer with a collecting optic on the order of 125 mm diameter is seen to be $\sim$ 2 orders of magnitude larger than that of the radio frequency approach using a 15 m diameter antenna. For a radio antenna smaller than the JCMT dish, such as at the SMA or ALMA, this factor increases further. In addition to being used to achieve a drastic reduction in instrument size, the increased atmospheric water vapor emission available to the infrared system can then be traded for an increase in measurement speed, signal-to-noise ratio or an even further reduction in instrument size.

1.4 Drawbacks of the Infrared Approach

The potential drawbacks of an infrared approach to atmospheric water vapor measurements are threefold. The first, as previously mentioned, is that a small aperture radiometer will not sample the same atmospheric column as that viewed by the antenna dish itself. To address this problem, the field of view of the smaller infrared radiometer may be designed so as to minimize this difference, for example, by sampling a patch of atmosphere of the same diameter as the radio antenna at a range within the scale height of water vapor. Another possible solution would be to install more than one infrared radiometer on a single antenna and use interpolation of the signals from each to derive an aggregate water vapor measurement.

The second possible disadvantage is that the emission from ice crystals in cir-

rus clouds is expected to have a greater impact in the infrared than at radio frequencies. The discussion is complicated by the lack of detailed information on cirrus cloud emission and the large variation of cloud and ice structures possible. Even in the event that common cloud types at the Chajnantor site, for example, interfere with infrared water vapor measurements, the best performance from ALMA will be obtained under the clearest atmospheric conditions and these are precisely the conditions under which the infrared approach is expected to excel. Perhaps the best solution to phase correction on the next generation of radio telescope arrays may be to incorporate both types of instruments to enable phase correction under a wide range of atmospheric conditions.

A third disadvantage is that water vapor emission measurements in the $20\,\mu$m spectral region becomes unusable at low altitudes due to the increased saturation of the large number of spectral lines in this region. The radio frequency approach, on the other hand, remains viable under these conditions and can be used at lower altitude radio arrays such as the VLA in New Mexico. The latest generation of radio interferometers including the Smithsonian Millimeter Array (SMA) on Mauna Kea and ALMA at Chajnantor, located at altitudes of $\sim 4000\,$m and $\sim 5000\,$m, respectively, are at sites where the infrared approach to water vapor radiometry can be expected to be effective.

1.5 Temporal Resolution

An estimate of the measurement rate needed to compensate for rapid variations of water vapor abundance above an antenna can be made by considering windspeed and

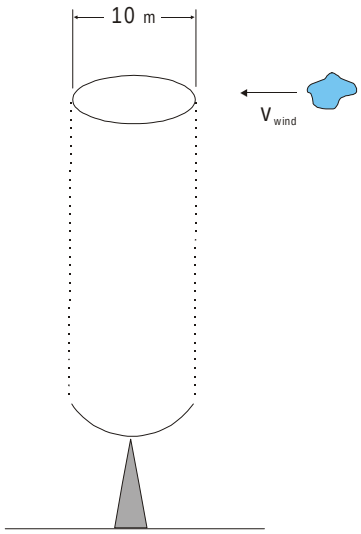

Figure 1.5: A simple model for the estimation of radiometer temporal resolution based on windspeed and antenna beam crossing time.

antenna size as depicted in Figure 1.5. If an average windspeed of $100\,\mathrm{km\,hr^{-1}}$ is assumed, the time taken for a water vapor feature to cross a nominally sized 10 m diameter antenna beam is $\sim 0.36\,\mathrm{s}$. Actual water vapor structures are more complicated than this simple model and thus a temporal resolution of 0.1 s was specified for the prototype radiometer.

1.6 Phase Compensation Requirements of ALMA

The radio telescope array currently planned for ALMA will consist of 64 antennae of 12 m diameter arranged on a 10 km diameter ring, and due to its large baseline, promises sub-milli-arcsecond imaging under the best atmospheric conditions. The water vapor column abundance, w, at Chajnantor, the site of ALMA on a high plateau in the Chilean Andes, varies between 0.5 and 4 mm pwv [5] with an average of 1 mm pwv [1]. A

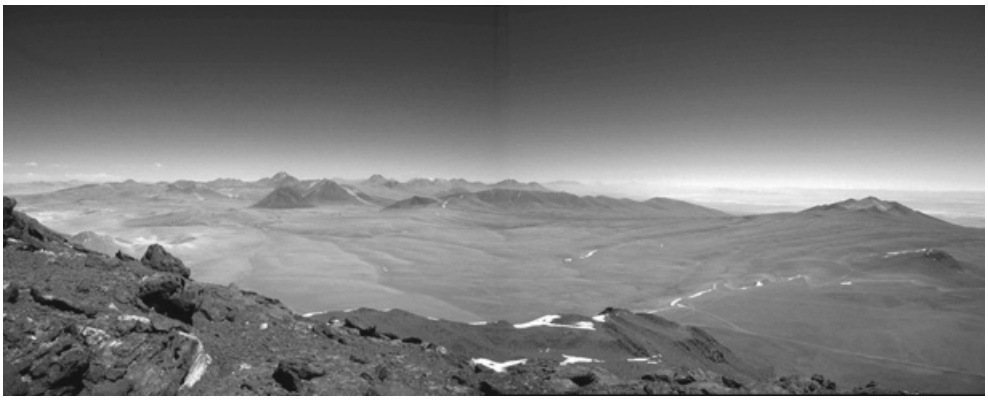

Figure 1.6: A view of the Atacama plateau, the future site of the Atacama Large Millimeter Array (ALMA).

photograph of the ALMA site is given in Figure 1.6 and an artist's representation of the ALMA array is given in Figure 1.7.

A measurement of the phase difference between signals from two antennae, obtained via correlation techniques, is expressed in terms of a visibility, V,

$$V = V_o\, e^{i\phi} \tag{1.6.1}$$

where ϕ is the phase difference between the signals at a given operating frequency and V_o is the maximum visibility occurring at zero phase delay. The effect on the average amplitude of V due to phase noise is [1]

$$\langle V \rangle = V_o\, \langle e^{i\phi} \rangle\, = V_o\, e^{-\,\phi_{rms}^2\,/\,2} \tag{1.6.2}$$

where ϕ_{rms} is the rms phase fluctuation due to variations in water vapor column abundance. For theoretical treatments this equation can be expressed in terms of the array baseline, b, using theoretical models of turbulence, for example, that due to Kolmogorov [1]. A phase error of 1 radian, for example, gives a coherence of

Figure 1.7: A representation of an arial view of the proposed ALMA array.

$$\frac{<V>}{V_o} = 0.6 \qquad 1.6.3$$

A recent ALMA Memo [7] quotes the current target electromagnetic path resolution as 50 μm, which, using the conversion factor of 6.5 given in equation 1.2.6, corresponds to a column abundance resolution of 7.7 μm *pwv*. This leads to a coherence of $\sim$ 95 % at 300 GHz or 85 % at 600 GHz. Another memo [8] puts the target path resolution at 11.5 μm (1.7 μm *pwv*), but this paper also concedes that this is '*setting the bar very high*'.

Given the greater performance expected from an infrared approach to water vapor radiometry, the '*bar*' was raised higher still by setting out to construct a prototype radiometer capable of 1 μm resolution in precipitable water vapor column abundance (6.5 μm path length error) in a 1 s integration. This thesis describes the design, construction and preliminary results obtained with the prototype radiometer at the JCMT.

Chapter 2 contains a review of the theory behind the operation of the radiometer

and includes a discussion of radiative transfer theory, water vapor line broadening, computer simulated atmospheric water vapor emission and radiosonde data showing the vertical distribution of water vapor in the atmosphere above Mauna Kea. Chapter 3 describes the design and construction of the prototype instrument and includes mechanical, electrical and optical and software aspects of this construction. Chapter 4 presents the preliminary results obtained on the trial run of the radiometer at the JCMT on the summit of Mauna Kea in Hawaii in December of 1999. Chapter 5 briefly discusses improvements and future directions of the infrared water vapor radiometer project. Chapter 6 concludes the thesis by giving a description of IDL analysis software created during the course of the thesis. A CD ROM is included with the thesis and contains IDL analysis software, raw data obtained with the prototype radiometer at the JCMT in the form of IDL *.sav* data files and the C++ control program used to operate the prototype instrument.

Chapter 2

Atmospheric Radiative Transfer and Water Vapor

2.1 Overview

The analysis of radiative transfer through a medium requires the application of radiometric principles; therefore a review of the key concepts and definitions of radiometry is given in Section 2.2. A detailed analysis of water vapor radiative transfer in the atmosphere would need to consider a multi-layer model including pressure, temperature and water vapor abundance variations with altitude and, in addition, take into account the complex spectral emission and absorption characteristics of water vapor and all other infrared-active molecular species present in the atmosphere. Such an analysis is difficult to develop analytically. In order to appreciate the general features of the dependence of water vapor infrared emission on the amount of water vapor present in the atmosphere, a review

is given in Section 2.3 of the analytical theory of radiative transfer in the simplified case of a single homogeneous atmospheric layer with a single line of absorption/emission, followed by a comparison of line broadening mechanisms applied to the case of water vapor above Mauna Kea. Having established the form of broadening expected for water vapor, the end result of the analysis is the synthesis of a *curve-of-growth* relating the radiant emission of water vapor to the abundance of emitting molecules.

Section 2.4 discusses the experimental technique used to acquire a *curve-of-growth* and its subsequent use in the prediction of instrument performance. Section 2.5 presents a computer generated model of atmospheric water vapor emission above Mauna Kea; it is then used to synthesize an artificial *curve-of-growth.* The estimated radiant emission derived from this *curve-of-growth* was used at the outset of the project to test the viability of an infrared water vapor radiometer using commercially available components. The vertical distribution of water vapor in the atmosphere has implications in regard to the optical design of the prototype radiometer; radiosonde data showing typical conditions above Mauna Kea are described in Section 2.6.

2.2 Radiometric Basics

Radiometry describes the transport of electromagnetic radiation in a physical system. The formulae encountered in radiometry involve spectral dependencies generally expressed in terms of electromagnetic frequency or wavelength. Spectral quantities in this thesis will be given in terms of *wavenumber,* σ, which specifies the reciprocal of wavelength,

$1/\lambda$, with units of cm^{-1}. Using the familiar wave equation $c = \nu\lambda$ describing the propagation of electromagnetic radiation in a vacuum, wavenumber is related to optical frequency by

$$\sigma = \frac{\nu}{c} \tag{2.2.1}$$

where ν is frequency in Hz and $c = 3 \times 10^{10}\,\mathrm{cm\,s}^{-1}$ is the speed of light in vacuum, or, alternatively, to wavelength, λ, expressed in microns (10^{-6} m) by

$$\sigma = \frac{10^4}{\lambda} \tag{2.2.2}$$

The analysis of radiative transfer is formulated in terms of spectral energy, E_σ, spectral power Φ_σ, spectral radiant intensity, I_σ, and spectral radiance, L_σ. The spectral subscript σ denotes a differential with respect to wavenumber, for example $E_\sigma = dE/d\sigma$, and thus total energy, power, intensity and radiance are obtained by integration of these quantities over a spectral range of interest. Table 2.1 lists these spectral quantities and their associated units.

Table 2.1: Radiometric quantities and associated units.

Radiometric Quantity	Symbol	Units
spectral energy	E_σ	$\mathrm{J}\ (\mathrm{cm}^{-1})^{-1}$
spectral power	Φ_σ	$\mathrm{W}\ (\mathrm{cm}^{-1})^{-1}$
spectral intensity	I_σ	$\mathrm{W\ sr}^{-1}(\mathrm{cm}^{-1})^{-1}$
spectral radiance	L_σ	$\mathrm{W\ m}^{-2}\mathrm{sr}^{-1}(\mathrm{cm}^{-1})^{-1}$

As shown schematically in Figure 2.1, the spectral intensity, I_σ, describes the emission of radiant spectral power, Φ_σ, emanating from a source area dA, or equivalently,

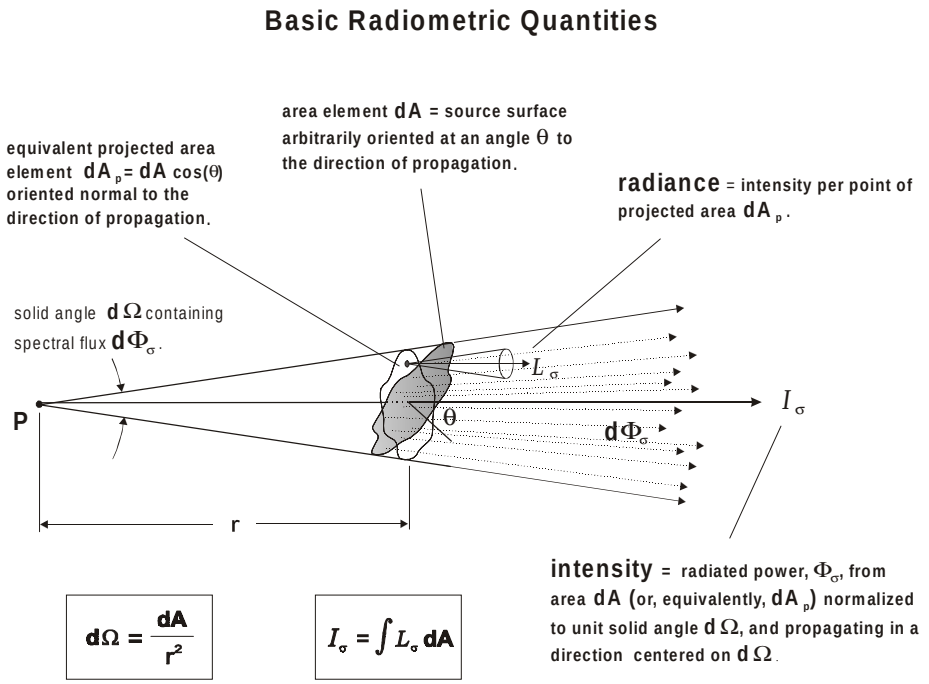

Figure 2.1: A schematic illustration of the relationships among the basic quantities of radiometry.

projected area $dA_P = dA\cos\theta$, contained within a solid angle $d\Omega$, labelled as travelling in a direction centered on solid angle $d\Omega$, and normalized to unit solid angle :

$$I_\sigma = \frac{d\Phi_\sigma}{d\Omega} \qquad 2.2.3$$

As seen in the figure, this emission is equivalent to that from a point source P at a distance r from the surface dA as shown in the figure. Spectral radiance, L_σ, normalizes the emitted spectral energy to unit *projected* area element dA_P in addition to unit solid angle :

$$L_\sigma = \frac{dI_\sigma}{dA_P} = \frac{d^2\Phi_\sigma}{dA_P\ d\Omega} \qquad 2.2.4$$

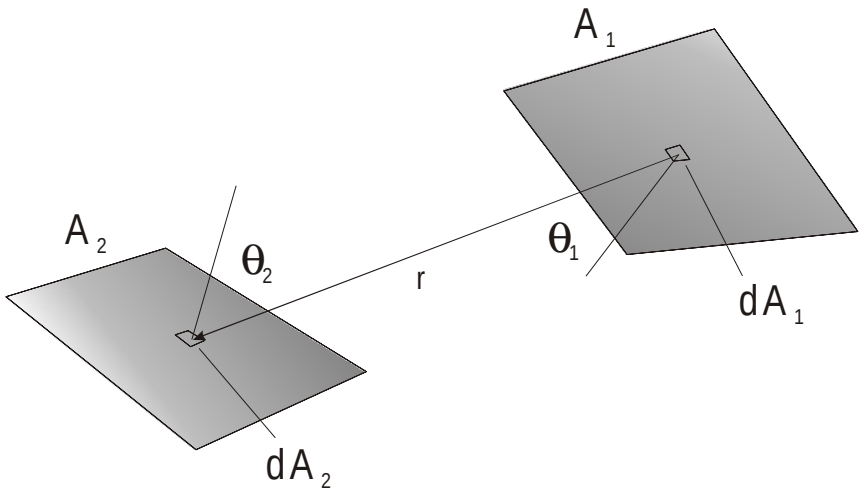

Figure 2.2: The general case of radiative transfer between two arbitrary surfaces.

Using these basic quantities, a general formula expressing the transfer of radiant energy from one physical surface to another is given by

$$d^2\Phi_{\sigma_{1,2}} = L_{\sigma_1}\frac{dA_1\cos\theta_1 dA_2\cos\theta_2}{r^2} \qquad 2.2.5$$

where $\Phi_{\sigma_{1,2}}$ is the spectral power transferred from surface A_1 to surface A_2 and L_{σ_1} is the spectral radiance of surface A_1. Area elements A_1 and A_2 are, in general, arbitrarily shaped and arbitrarily oriented surfaces whose normal vectors subtend the angles θ_1 and θ_2 with respect to the distance between differential elements dA_1 and dA_2, as shown in Figure 2.2. In this thesis only plane parallel radiative transfer will be considered (i.e., $\theta_1 = \theta_2 = 0$).

The transfer of radiant power from an atmospheric source area to a radiometer detector element via an optical system can be derived from equation 2.2.5. Using the definition of solid angle, $\Omega = A/r^2$, the transfer of spectral power from an atmospheric source area, A_s, onto a collecting aperture of area A_p, is given by

$$\Phi_\sigma = L_\sigma \, A_p \, \frac{A_s}{r^2} = L_\sigma \, A_p \, \Omega_d \tag{2.2.6}$$

where Ω_d is the solid angle subtended at the collecting aperture by the source area and L_σ is the spectral radiance of the atmospheric source area. Since the throughput of an optical system is conserved [9], this is equivalent to

$$\Phi_\sigma = L_\sigma \, A_d \, \Omega_d \tag{2.2.7}$$

where Ω_d is the solid angle subtended at the detector by the collecting aperture. This expression will be used extensively in Chapter 4.

2.3 Radiative Transfer in a Single-Layer Atmosphere

2.3.1 Absorption in a Linear Medium

If a medium absorbs linearly and the propagation direction is labelled by z, then the change in spectral intensity due to absorption can be written as [10]

$$dI_\sigma = -k_\sigma \, \rho \, I_\sigma \, dz \tag{2.3.1}$$

where k_σ is the mass absorption coefficient in $\mathrm{m^2\,kg^{-1}}$and ρ is the mass density of the medium in kg $\mathrm{m^{-3}}$. Alternatively, a linear absorption coefficient, κ_σ, can be defined with units of $\mathrm{m^{-1}}$, allowing the attenuation to be expressed as

$$dI_\sigma = -\kappa_\sigma \, I_\sigma \, dz \tag{2.3.2}$$

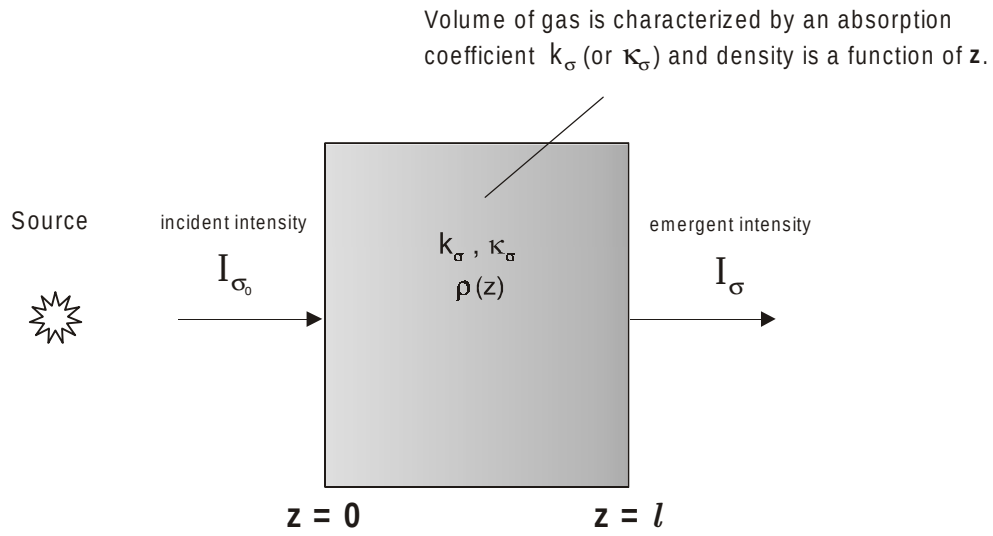

Figure 2.3: Absorption in a linear medium.

The dimensions of κ_σ or $k_\sigma \rho$ indicate that these quantities specify absorption per unit distance of propagation and thus apply to unit cross-sectional area, or equivalently, *column area.*

As depicted in Figure 2.3, a useful relation can be developed immediately for the case of the transmission of radiation through a gaseous medium of thickness l, mass density ρ, and absorption coefficient k_σ, or, alternately, κ_σ. If z again denotes the propagation direction and $I_{\sigma_0} = I_{\sigma(z=0)}$ is the normally incident intensity on the slab, integration of equations 2.3.1 and 2.3.2 from $z = 0$ to $z = l$ gives an emergent intensity of

$$I_\sigma = I_{\sigma_0}\, e^{-\int_0^l k_\sigma \rho(z) dz} dz = I_{\sigma_0}\, e^{-\int_0^l \kappa_\sigma(z) dz} \qquad 2.3.3$$

in the case of a medium of variable density, and

$$I_\sigma = I_{\sigma_0}\, e^{-k_\sigma \rho l} = I_{\sigma_0}\, e^{-k_\sigma u} = I_{\sigma_0}\, e^{-\kappa_\sigma l} \qquad 2.3.4$$

in the case of a medium of constant density. The quantity $u = \rho\, l$ is known as the *absorber amount* with units of $\mathrm{kg\,m^{-2}}$. Equation 2.3.4 can also express the general case of variable column density as in equation 2.3.3 if the constant density ρ is replaced with an averaged density

$$\rho_{av} = \frac{\int_0^l \rho\, dz}{\int_0^l dz} \tag{2.3.5}$$

The absorption coefficients k_σ and κ_σ describe the spectral absorption in the medium and are in general functions of wavenumber and density. Formulas for these coefficients will be developed in Section 2.3.6 for the case of a single molecular line.

The differential expression for absorption as given by equation 2.3.2 may be reformulated in terms of loss of spectral energy due to absorption. Using equations 2.2.4 and 2.3.2, and the fact that $dE_\sigma = d\Phi_\sigma\, dt$, the differential expression for the loss of radiant energy is given by

$$dE_\sigma = \kappa_\sigma\, L_\sigma d\Omega\, dA\, dz\, dt \tag{2.3.6}$$

and will be useful in the development of atmospheric radiative transfer discussed in Section 2.3.5.

2.3.2 Emission in a Linear Medium

As shown in Figure 2.4, the radiant emission of spectral energy, E_σ, from an infinitesimal volume element dV of a gaseous medium into a solid angle $d\Omega$ is given by

$$dE_\sigma = \epsilon_\sigma\, d\Omega\, dV\, dt \tag{2.3.7}$$

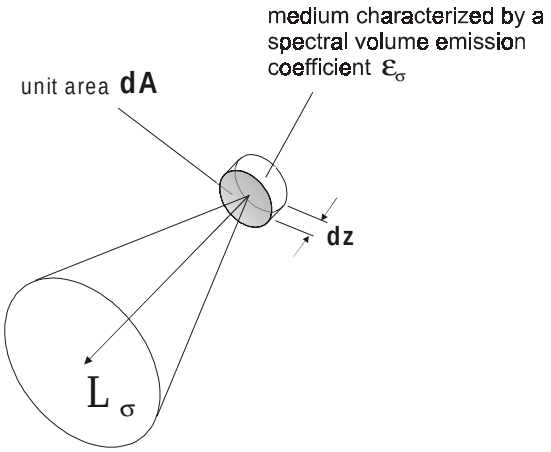

Figure 2.4: Emission from a linear medium.

$$= \epsilon_\sigma \; d\Omega \; dA \; dz \; dt \tag{2.3.8}$$

where ϵ_σ is the spectral volume emission coefficient characterizing the medium with units of J $s^{-1}m^{-3}(cm^{-1})^{-1}sr^{-1}$. The analysis of radiative transfer in the atmosphere will be carried out for the case of plane parallel geometry and hence the propagation direction parameter, z, is separated from the volume term in equation 2.3.8.

2.3.3 Atmospheric Pressure vs. Density

Equations describing radiative transfer are usually formulated in terms of particle density whereas atmospheric conditions are often given in terms of pressure. Any expression involving a mass density of particles, ρ, in kg m^3, can be written in terms of the atmospheric pressure, P, since, for any given volume of atmosphere, V, the ideal gas law leads to the conversion

$$\rho = \frac{M\,P}{R\,T_{atm}} = \frac{m_p\,P}{kT_{atm}} \qquad 2.3.9$$

where $R = 8.314\ \mathrm{J\,mol^{-1}\,K^{-1}}$ is the universal gas constant, $k = 1.38 \times 10^{-23}\ \mathrm{J\,K^{-1}}$ is Boltzmann's constant, T_{atm} is the temperature of the atmospheric volume V, M is molecular weight in $\mathrm{kg\ mol^{-1}}$, and m_p is molecule mass in kg. This relationship can apply to each atmospheric species individually; in this case M, m_p, P and ρ are the molecular weight, molecule mass, partial pressure and mass density of the species per unit volume of atmosphere, respectively. Alternatively, by taking an average of M and m_p per unit volume of atmosphere, i.e. $\langle M \rangle$ and $\langle m_p \rangle$, equation 2.3.9 expresses the conversion between total atmospheric pressure, P_{atm}, and total atmospheric mass density, ρ_{atm}.

Alternatively, a *mass mixing ratio*, W_s, particular to a given species, can be defined as

$$W_s = \frac{M}{\langle M \rangle} = \frac{m_p}{\langle m_p \rangle} = \frac{\rho}{\rho_{atm}} \qquad 2.3.10$$

and used in conjunction with equation 2.3.9 to evaluate the mass density for a particular species. This last relation is useful, for example, when the water vapor density, ρ_{H_2O}, must be extracted from radiosonde water vapor mixing ratio data expressed in grams of water vapor per kilogram of atmosphere.

2.3.4 Hydrostatic Equilibrium in the Atmosphere

Prior to the theoretical development of single line atmospheric radiative transfer, an expression for the variation of density with altitude is required since the absorption

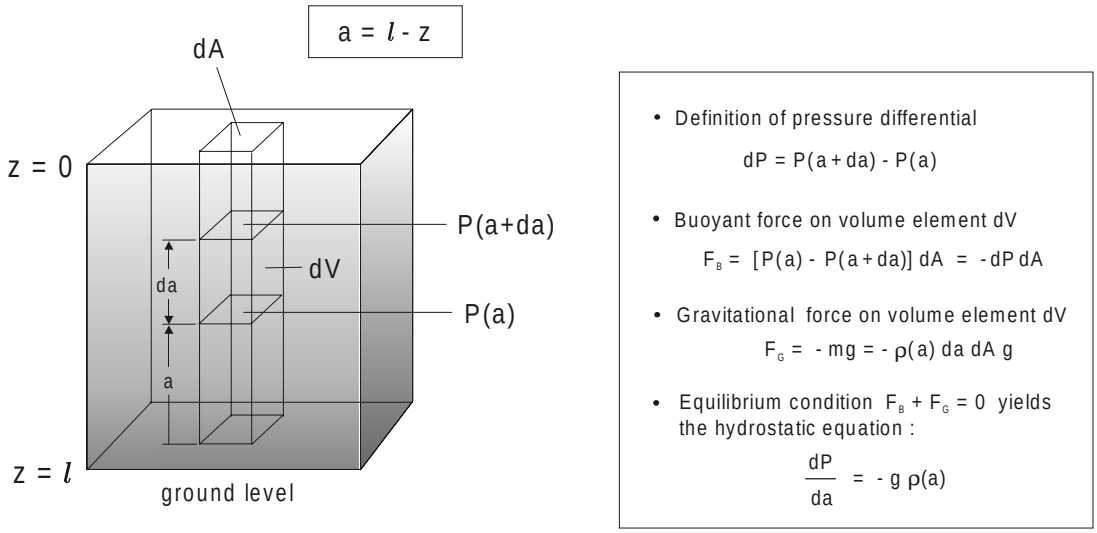

Figure 2.5: The hydrostatic equation describes the gravitationally induced vertical density profile $\rho = \rho(a)$ where a is the altutude measured from ground level. The density profile can alternately be given as $\rho = \rho(z)$ where z is the electromagnetic propagation direction used in the analysis of radiative transfer and is measured from the top of the layer.

coefficient, k_σ, will be shown to have a density dependence. A plane parallel single layer atmospheric model with a homogenous temperature but gravitationally induced pressure variation will be considered.

Considering the column of unit cross-sectional area shown in Figure 2.5, and using the propagation direction parameter, z, in place of altitude, the differential expression for hydrostatic equilibrium is

$$dP = g\,\rho\,dz \qquad 2.3.11$$

where P is pressure in $\mathrm{N\,m^{-2}}$ and $g = 9.8\,\mathrm{m\,s^{-2}}$ is the acceleration due to gravity. Using equation 2.3.9 , equation 2.3.11 becomes

$$\frac{dP}{P} = \frac{dz}{H} \qquad 2.3.12$$

where H, the *scale height*, is the altitude at which the pressure is reduced by a factor of e^{-1} from that at ground level.

$$H = \frac{R\,T_{atm}}{M\,g} \tag{2.3.13}$$

The scale height can apply to each atmospheric species individually or to the atmosphere as a whole using an average atmospheric molecular weight M_{atm}. Integration of equation 2.3.12 from $z = l$ to an arbitrary z yields

$$P\,(z) = P(l)\,e^{-\int_z^l \frac{1}{H} dz} \tag{2.3.14}$$

where $P(l)$ is the ground pressure.

Equation 2.3.14 can alternately be put in terms of density, ρ, or number density, N, by replacing $P(z)$ and $P(l)$ with $\rho(z)$ and $\rho(l)$, or $N(z)$ and $N(l)$, respectively. With a temperature T_{atm} assigned to the isothermal model atmosphere the expression for density as a function of altitude is then

$$\rho(z) = \rho(l)\,e^{-\frac{(l-z)}{H}} \tag{2.3.15}$$

2.3.5 Radiative Transfer in a Plane Parallel Atmosphere

Figure 2.6 shows a schematic of the simplified case of plane parallel radiative transfer in a single atmospheric layer subject to gravity. The model atmosphere with total path length, l, is characterized by an absorption coefficient κ_σ, emission coefficient ϵ_σ, gravitationally induced density profile $\rho(z)$ and assigned a uniform temperature T_{atm}. A

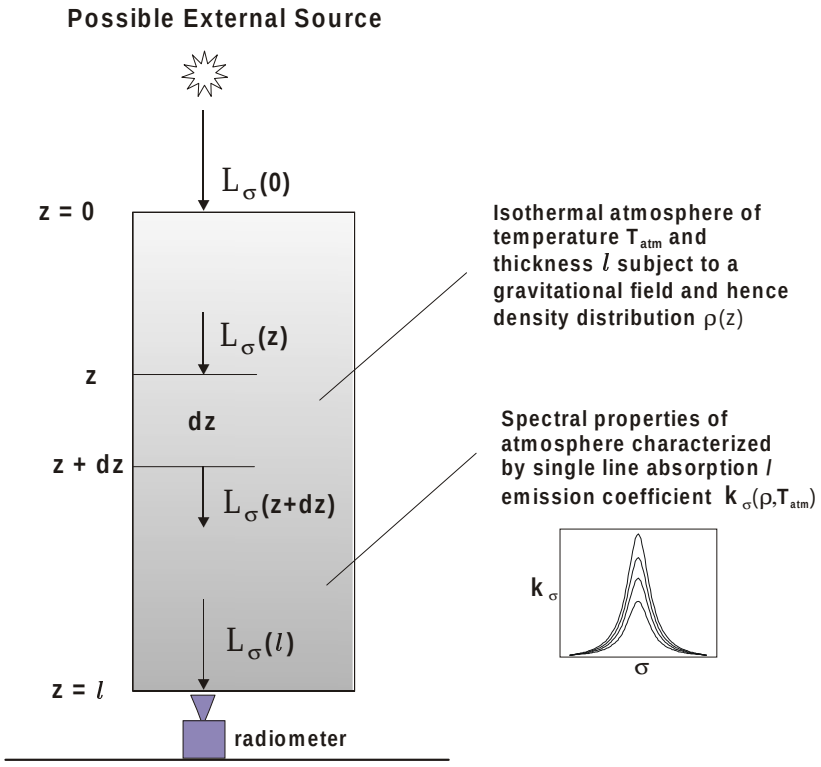

Figure 2.6: A schematic illustration of the simplified model used for the analysis of atmospheric radiative transfer. A single line of absorption/emission is considered.

possible external source is shown outside the atmosphere and a radiometer views vertically from the ground.

Using the definition of radiance given by equation 2.2.4, and noting that $d\Phi_\sigma = dE_\sigma/dt$, conservation of spectral energy applied to the section dz requires that

$$[L_\sigma(z+dz) - L_\sigma(z)]\ d\Omega\, dA\, dt\ =\ dE_{\sigma_{emitted}} - dE_{\sigma_{absorbed}} \qquad 2.3.16$$

or

$$[\tfrac{dL_\sigma}{dz}]\, dz\ d\Omega\, dA\, dt = dE_{\sigma_{emitted}} - dE_{\sigma_{absorbed}} \qquad 2.3.17$$

From equation 2.3.8, the emitted energy in this layer is

$$dE_{\sigma_{emitted}} = \epsilon_\sigma \; d\Omega \, dA \, dz \, dt \tag{2.3.18}$$

and, using equation 2.3.6, the energy absorbed is

$$dE_{\sigma_{absorbed}} = \kappa_\sigma \, L_\sigma \; d\Omega \, dA \, dz \, dt \tag{2.3.19}$$

combining equations 2.3.17 through 2.3.19 gives

$$\frac{dL_\sigma}{dz} = -\kappa_\sigma L_\sigma + \epsilon_\sigma \tag{2.3.20}$$

which is known as the equation of radiative transfer. The opacity, $\chi(z)$, can be defined as

$$\chi(l) = \int_{z=0}^{z=l} \; \kappa_\sigma dz \tag{2.3.21}$$

Using this notation, $d\chi = \kappa_\sigma \, dz$ and the equation of radiative transfer becomes

$$\frac{dL_\sigma}{d\chi} = J_\sigma - L_\sigma \tag{2.3.22}$$

where J_σ is the source function

$$J_\sigma = \frac{\epsilon_\sigma}{\kappa_\sigma} \tag{2.3.23}$$

Equation (2.3.22) can be integrated by multiplying both sides by e^χ,

$$\frac{dL_\sigma}{d\chi} \; e^\chi + L_\sigma \; e^\chi = J_\sigma \; e^\chi \tag{2.3.24}$$

or, equivalently,

$$\frac{d}{d\chi}(L_\sigma \; e^\chi) = J_\sigma \; e^\chi \tag{2.3.25}$$

Integrating from $\chi = 0$ to an arbitrary χ yields

$$\int_0^{\chi} \frac{d}{d\chi}(L_\sigma\ e^{\chi})\ d\chi = \int_0^{\chi} J_\sigma\ e^{\chi}\ d\chi \qquad 2.3.26$$

$$[L_\sigma\ e^{\chi}]_0^{\chi} = [J_\sigma\ e^{\chi}]_0^{\chi} \qquad 2.3.27$$

With $L_{\sigma_0} = L_{\sigma(\chi=0)}$ denoting the radiance vertically incident on the top of the atmosphere, evaluation of the definite integral yields

$$L_\sigma\ e^{\chi} - L_{\sigma_0} = J_\sigma(e^{\chi} - 1) \qquad 2.3.28$$

and after division by e^{χ}, the radiance observed by the radiometer on the ground, L_σ, can be written as

$$L_\sigma = L_{\sigma_0}\ e^{-\chi} + J_\sigma(1 - e^{-\chi}) \qquad 2.3.29$$

The principle of local thermodynamic equilibrium (LTE) states that, for a given atmospheric layer, the absorption due to the molecular species located in that layer must be equal to its emission if the temperature of the layer is to remain constant. Kirchoff's law then allows the source function to be taken as the Planck function,

$$J_\sigma = \frac{\epsilon_\sigma}{\kappa_\sigma} = B_\sigma(T) \qquad 2.3.30$$

where $B_\sigma(T)$ is the Planck radiance, which, in terms of wavenumber, is

$$B_\sigma\,(T) = (2\,h\,c^2\,100^4\,\sigma^3)\left(e^{\frac{hc100\sigma}{kT_{atm}}} - 1\right)^{-1} \qquad 2.3.31$$

with units of $\mathrm{W\,m^{-2}sr^{-1}(cm^{-1})^{-1}}$ and is evaluated at the temperature of the layer, $T = T_{layer}$, in K.

If it can be assumed that the radiometer does not observe a significant celestial object, the spectral radiance that is incident on the outside of the atmosphere, L_{σ_0}, is then due to the equivalent 3 K cosmic background radiation of space, which, if evaluated using equation 2.3.31, is seen to be negligible at infrared wavelengths. The radiance observed by the radiometer is then solely due to emission of the atmosphere. Using the mass absorption coefficient, k_σ, and assuming this coefficient to have a dependence on density, ρ, which itself is a function of altitude, z, the expression for the radiance becomes, from equation 2.3.29,

$$L_\sigma = B_\sigma(T_{atm})(1 - e^{-\int k_\sigma \rho(z)\, dz}) \qquad 2.3.32$$

Using the averaged, but still exact, expression for density obtained by substituting equation 2.3.15 into equation 2.3.5, the observed radiance is then

$$L_\sigma = B_\sigma(T_{atm})(1 - e^{-k_\sigma \rho_{av} l}) \qquad 2.3.33$$

An atmospheric molecular species under fully saturated conditions ($k_\sigma \rho_{av} l >> 1$) is then seen to emit at a maximum radiance given by the Planck radiance, evaluated at the atmospheric temperature in which the species resides.

Having established an expression for the radiance of a single spectral line observed by a radiometer on the ground, attention is now turned to the form of k_σ which reflects the amount of absorption, and, by Kirchoff's law the amount of emission, in the model atmosphere. The form of k_σ is shown to depend on the broadening mechanism of the transition under investigation.

2.3.6 Broadening Mechanism

For the case of absorption due to a single spectral line, the mass absorption coefficient, k_σ, can be expressed as

$$k_\sigma = S\, f(\sigma - \sigma_0) \tag{2.3.34}$$

where $f(\sigma - \sigma_0)$ is a normalized shape function, or *line broadening profile*, which has the property

$$\int_{-\infty}^{\infty} f(\sigma - \sigma_0)\, d\sigma = \int_{0}^{\infty} f(\sigma - \sigma_0)\, d\sigma = 1 \tag{2.3.35}$$

and is determined from the line broadening mechanism. The formula for f contains a parameter, γ, the *half width at half maximum* or HWHM, which specifies the distance, in wavenumbers, from the line center, σ_0, to the points on either side of the line center where the absorption falls to half its maximum value, as shown in Figure 2.7.

The parameter S in equation 2.3.34 is known as the *integrated line strength*

$$S = \int_{-\infty}^{\infty} k_\sigma\, d\sigma = \int_{0}^{\infty} k_\sigma\, d\sigma \tag{2.3.36}$$

with units of $\mathrm{m^2\,kg^{-1}cm^{-1}}$ and its value for any particular transition is available from data tabulated in the literature [11] specified at a standard temperature of 296 K. In light of equation 2.3.4, the line strength for various gases can be experimentally determined using a vapor cell of path length, l, and homogeneous sample of density ρ through the relation

$$S = \int_{0}^{\infty} \frac{1}{\rho l} \ln\left(\frac{I_{\sigma_0}}{I_\sigma}\right)\, d\sigma \tag{2.3.37}$$

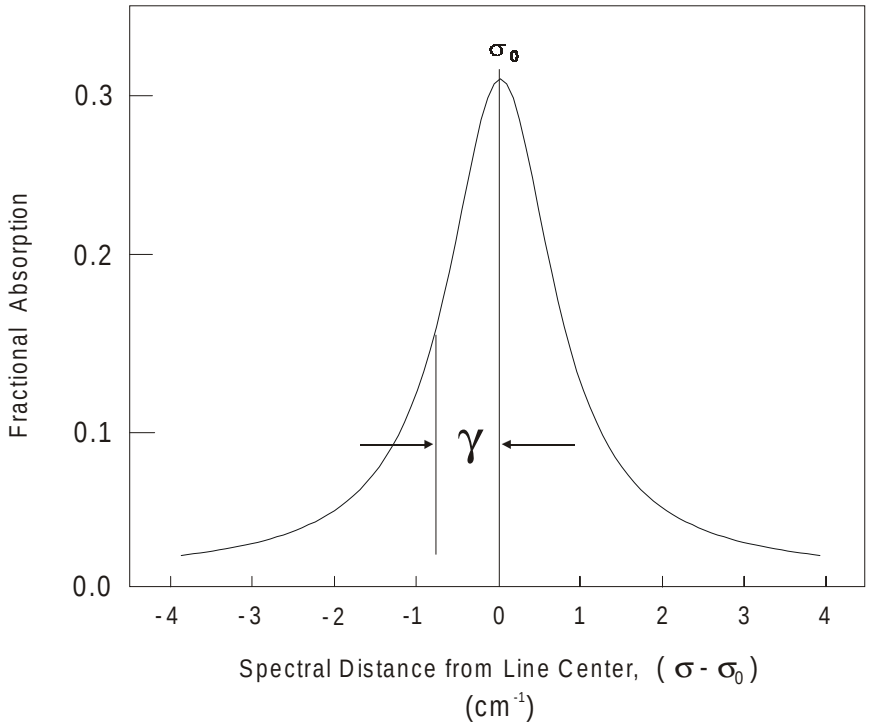

Figure 2.7: A generic line profile is characterized by a parameter, γ, giving the distance, in wavenumbers, from the line center, σ_o, to the point where absorption falls to half that at the line center. γ is refered to as the half width at half maximum (HWHM).

The line strength weights the area of the normalized broadening profile for a given absorber abundance while the shape of the broadening profile reflects the broadening conditions that are in effect. As the broadening profile changes shape in response to different broadening conditions, the integrated area remains constant. The line strength, S, is thus independent of the width of the line profile and is a fundamental parameter describing a specific transition.

There are essentially three mechanisms which cause the emission from a quantum transition to have a finite width. The first is the *natural width* of a line which arises because the quantum states of a molecule have a variability in energy, ΔE, which is related to the

lifetime of the state, Δt, through the Heisenberg relationship $\Delta E\,\Delta t \simeq \hbar$. The variability in the frequency of emission [12], expressed in terms of wavenumber, can be written

$$\Delta\sigma = \frac{\Delta E}{hc} \tag{2.3.38}$$

where h is Planck's constant. The effects of natural broadening, being less than $0.001\,\mathrm{cm}^{-1}$ for the strongest molecular transitions [13] [14], will not be significant in comparison to other atmospheric broadening mechanisms and can be neglected.

The second broadening mechanism is due to the Doppler shift in emission frequency caused by the motion of the emitting molecule towards or away from the observer. The distribution of molecular speeds in an atmospheric layer of temperature T are described by the Maxwell-Boltzmann (MB) probability distribution

$$P(\mathrm{v}) = 4\pi\mathrm{v}^2\left(\frac{m_{molecule}}{2\pi kT}\right)^{3/2}\exp\left(\frac{-m_{molecule}\,\mathrm{v}^2}{2kT}\right) \tag{2.3.39}$$

where v is the velocity of the molecule, $m_{molecule}$ is its mass in kg, k is Boltzmann's constant and the temperature is given in K. The resulting Doppler shifts will then also be described by a statistical distribution and the Doppler line broadening expression, derived using the MB distribution, is [10]

$$k_{\sigma_D} = \frac{S}{\gamma_D\sqrt{\pi}}\exp\left(\frac{\sigma-\sigma_o}{\gamma_D}\right)^2 \tag{2.3.40}$$

where γ_D is the Doppler HWHM,

$$\gamma_D = \frac{\sigma_o}{c}\left(\frac{2kT}{m_{molecule}}\right)^{1/2} = \frac{\sigma_o}{c}\left(\frac{2RT}{M}\right)^{1/2} \tag{2.3.41}$$

The Doppler broadening mechanism becomes increasingly important at high altitudes where the atmospheric pressure is low and the atmospheric temperature, and hence mean molecular speed, is high.

The third broadening mechanism, dominant at lower altitudes, is known as *Lorentz* broadening and arises from interruptions in the oscillations of quantum transitions due to collisions between molecules. The frequency of the interruptions is dependent on the pressure and, to a lesser extent, the temperature of the gas. A Fourier analysis of the finite length wave-trains constituting the emission from quantum transitions in a homogeneous volume of emitters, and taking into account the Poissonian nature of the perturbations [12], yields the pressure broadened, or Lorentz, lineshape

$$k_{\sigma_L} = \frac{S\gamma_L}{\pi} \frac{1}{(\sigma-\sigma_o)^2 + \gamma_L^2} \qquad 2.3.42$$

where γ_L is the Lorentzian HWHM. Using the kinetic theory of gases, γ_L can be related [12] to the pressure, P, and temperature, T, of the molecular species through the relation

$$\gamma_L = \frac{1}{4\pi\tau c} = \gamma_o \frac{P}{P_o} \sqrt{\frac{T_o}{T}} \qquad 2.3.43$$

where τ is the mean time between collisions of the molecules and γ_o is the HWHM tabulated in the literature at a specific pressure and temperature. In the case of an altitude dependent pressure $P = P(z)$, the Curtis-Godson approximation,

$$P_{CG} = \frac{\int P(z)\, W_s\ \rho(z)\, dz}{\int W_s\ \rho(z)\, dz} \qquad 2.3.44$$

can be used in equation 2.3.43. A similar calculation may be applied to the temperature, but since equation 2.3.43 exhibits only a square root dependence on temperature, and

furthermore, that the temperature falls off roughly linearly with altitude, the effects of an altitude dependent temperature are less significant.

Figure 2.8 shows a comparison of the shapes of the Lorentz and Doppler profiles. Each has been normalized to unit area and thus represents the same amount of total absorption but it will be noticed that the Lorentz profile has much larger wings and hence the total absorption, or, by Kirchoff's law, emission, due to a single Lorentz broadened line requires integrating out to much larger distances from the line center than in the case of a Doppler broadened line.

2.3.7 Broadening Regime for Water Vapor

The analysis thus far has not been specific about the atmospheric molecular species involved in radiative transfer. The broadening mechanisms discussed in the previous section are sensitive to temperature and pressure, and, since these quantities are functions of altitude, the vertical distribution of the atmospheric molecular species under consideration has a direct bearing on which broadening mechanism(s) are of importance. The molecular species of interest for this project is water vapor, and since this molecular species exists primarily at altitudes below $\sim 10\,\mathrm{km}$, the half widths of the Lorentz and Doppler profiles will be compared to establish their relative importance at a high altitude observing site such as Mauna Kea.

As will be shown in Section 2.6, radiosonde data reveal that water vapor exists in significant amounts to an altitude of approximately $1 - 2\,\mathrm{km}$ above the summit of Mauna

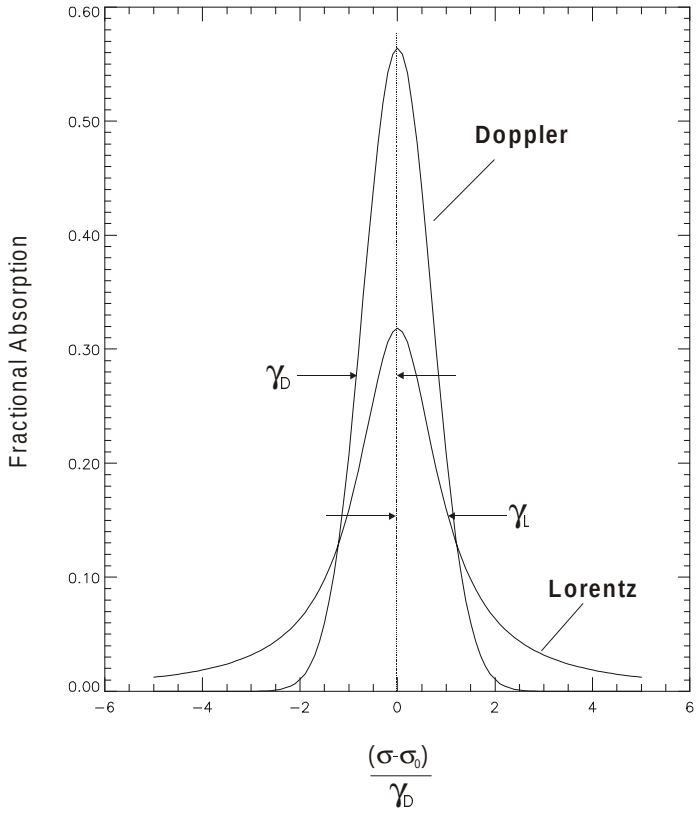

Figure 2.8: A comparison of the Lorentz and Doppler area normalized line broadening profiles. The Lorentz profile is seen to extend to larger distances from the line center than in the Doppler case for the same total amount of absorption.

Kea. Using these radiosonde derived data, an atmospheric temperature of $\sim 260\,\mathrm{K}$ and an atmospheric pressure of $\sim 600\,\mathrm{mb}$ (60 kPa) may be assigned to this region. A typical water vapor line has a width of $\gamma_o \sim 0.1\,\mathrm{cm}^{-1}$ ($\sigma_o = 500\,\mathrm{cm}^{-1}$, $P_o = 101.3\,\mathrm{kPa}$, $T_o = 296\,K$) [11], and, with $M_{H_2O} = 0.018\ \mathrm{kg\,mol}^{-1}$, the following half widths can be calculated for the Lorentz and Doppler broadening of water vapor using equations 2.3.41 and 2.3.43:

$$\gamma_D = \frac{\sigma_o}{c}\sqrt{\frac{2RT}{M_{H_2O}}} = \frac{500}{3\times10^8}\sqrt{\frac{(2)(8.314)(260)}{0.018}} = 8.2\times10^{-4}\,\mathrm{cm}^{-1} \qquad 2.3.45$$

$$\gamma_L = \gamma_o\frac{P}{P_o}\sqrt{\frac{T_o}{T}} = (0.1)\frac{60}{101.3}\sqrt{\frac{296}{260}} = 6.3\times10^{-2}\,\mathrm{cm}^{-1} \qquad 2.3.46$$

For atmospheric water vapor observed from Mauna Kea, Lorentz broadening is seen to dominate over Doppler broadening. In the remainder of the analysis the broadening coefficient will thus be assumed to be Lorentzian, i.e.,

$$k_\sigma = k_{\sigma_L} \tag{2.3.47}$$

2.3.8 Radiance from a Single Water Vapor Line

The expression for the total radiance seen by a radiometer on the ground is found by integrating equation 2.3.33 over a spectral range of interest. For the case where the integral is taken over all wavenumbers the total radiance is

$$L = \int_0^\infty B_\sigma(T_{atm})\,(1 - e^{-\,k_\sigma\ \rho\ l})\,d\sigma \tag{2.3.48}$$

With k_σ expressing the Lorentz broadened absorption due to a single line as given by equation 2.3.42, the result of the spectral integration can be evaluated analytically and is known as the Ladenberg-Reiche equation [14]

$$L = 2\pi\,\gamma_L\,x\,e^{-x}[J_0(x) + J_1(x)] \tag{2.3.49}$$

where $J_0(x)$ and $J_1(x)$ are the Bessel Functions of order zero and one, respectively, and imaginary argument. The quantity x is given by

$$x = \frac{S\,u}{2\pi\,\gamma_L} \tag{2.3.50}$$

where

$$u = \int_0^l \rho(z)\,dz = \rho_{av}\,l \tag{2.3.51}$$

is the absorber amount along an atmospheric path length l containing an average density of absorber ρ_{av}.

An *optically thin* limit is applicable to an atmosphere with a low opacity $\chi = k_\sigma \, \rho \, l$, as defined in equation 2.3.21. An expression for the ground level radiance may be obtained either by using a small x approximation of equation 2.3.49, or directly from equation 2.3.48 by taking $\chi_\sigma \ll 1$, in which event $e^{-\chi} \approx 1 - \chi = 1 - k_\sigma \rho l$. The spectral integration then yields

$$L = S \, \rho_{av} \, l \int_0^\infty B(T_{atm}) \, d\sigma \qquad 2.3.52$$

In the case of large opacity, the radiance can be shown to have the form [14]

$$L = 2\sqrt{S \, \gamma_L \, \rho_{av} \, l} \int_0^\infty B(T_{atm}) \, d\sigma \qquad 2.3.53$$

The integration over wavenumber occurring in equation 2.3.48 is for the range $[0, \infty]$ but in practice, for a band limited optical system, this integral and the integrals of the limiting cases in equations 2.3.52 and 2.3.53 are evaluated over the passband of the system determined by the combined detector/filter response.

As indicated by equation 2.3.52, in the case of low opacity a linear relationship exists between the observed radiance and the absorber abundance, ρl. A water vapor radiometer is then seen to be most sensitive to growth in emission when the water vapor abundance is small and this is precisely the regime in which the infrared radiometer is expected to be valuable to high altitude submillimeter observatories.

2.3.9 *Curve-of-Growth* Synthesis

The radiance observed by a radiometer plotted as a function of the abundance of the emitting species, or absorber amount, is known as a *curve-of-growth.* An IDL program was written to illustrate the growth in integrated emission of a single Lorentz broadened line as a function of increasing path length, l, while keeping density, pressure, temperature and line strength constant. A Lorentz half width, γ_0, of 0.1 cm^{-1} and a normalized Planck radiance of 1 were arbitrarily selected for use in the numerical illustration. Figure 2.9 shows the growing Lorentz profile and the resulting integrated *curve-of-growth.*

When the integrated emission and absorber amount are plotted using logarithmic scales, the curve clearly shows the two limiting power law behaviors described by equations 2.3.52 and 2.3.53, i.e., a weak and a strong regime. In the weak regime, the area under the spectral line grows linearly with increasing absorber abundance. As the absorber abundance increases, the line eventually saturates as it reaches the Planck curve corresponding to the local atmospheric temperature. Further increase in absorber abundance results in a widening of the spectral line and, when the line is heavily saturated, the integrated area increases as the square root of the abundance.

In order to enhance sensitivity, the spectral bandpass of a practical infrared radiometer should include many lines of water vapor emission. Such a region may comprise a complicated mixture of weak and saturated lines. Although it cannot be described analytically, the resulting *curve-of-growth* from a spectral region containing many lines will have the general form as that displayed in Figure 2.9. Data obtained from the prototype instru-

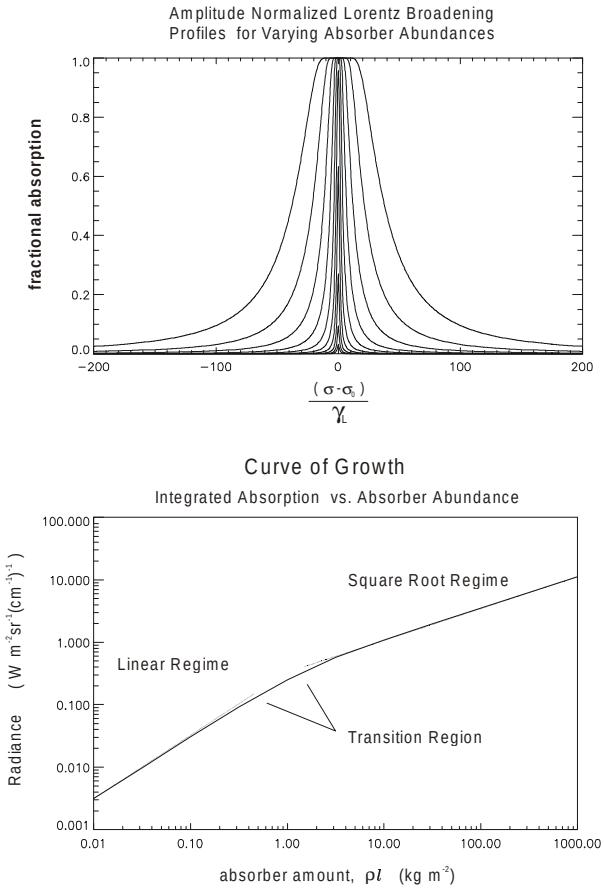

Figure 2.9: A curve of growth (bottom graph) can be synthesized by integrating the emission of a Lorentz broadened line (top graph) as it responds to an increasing absorber amount.

ment and presented in Chapter 4 confirm the presence of two distinct regimes of growth corresponding to a constant power law description in low and high water vapor abundance conditions.

2.4 Application of the *Curve-of-Growth*

Data from a calibrated water vapor radiometer providing phase calibration for an interferometer array would have the form of signal as a function of time. As demonstrated

in the following section, data in the form of a *curve-of-growth* can be used to predict the performance of a radiometer. Section 4.8 will also show the usefulness of the *curve-of-growth* in calibrating the radiometer.

2.4.1 Obtaining a *Curve-of-Growth* Via Sky-Dipping

To obtain a *curve-of-growth*, the amount of absorber viewed by a radiometer must be varied in a known way and plotted against the corresponding signal. In a laboratory setting, for example, a variable length multi-pass vapor cell could be used to vary the observed absorber amount in a well defined way while keeping the broadening conditions constant. In the case of the atmosphere, there is no way to arbitrarily set the water vapor abundance but the method of *sky-dipping* provides a convenient method of varying the effective absorber amount seen by a radiometer. If the vertical pressure, temperature and absorber amount profiles can be assumed to be the same for a local section of atmosphere, then, as in the laboratory setting, the observed absorber amount can be varied by a controlled variation of path length by acquiring signals from a radiometer as it is swept through a range of zenith angles.

Referring to Figure 2.10, for an atmosphere of effective height h, the effective path length along a line of sight defined by zenith angle θ is given by

$$l = \frac{h}{\cos\theta} \qquad 2.4.1$$

Since 1 airmass corresponds to the atmospheric height h, the path length may be written

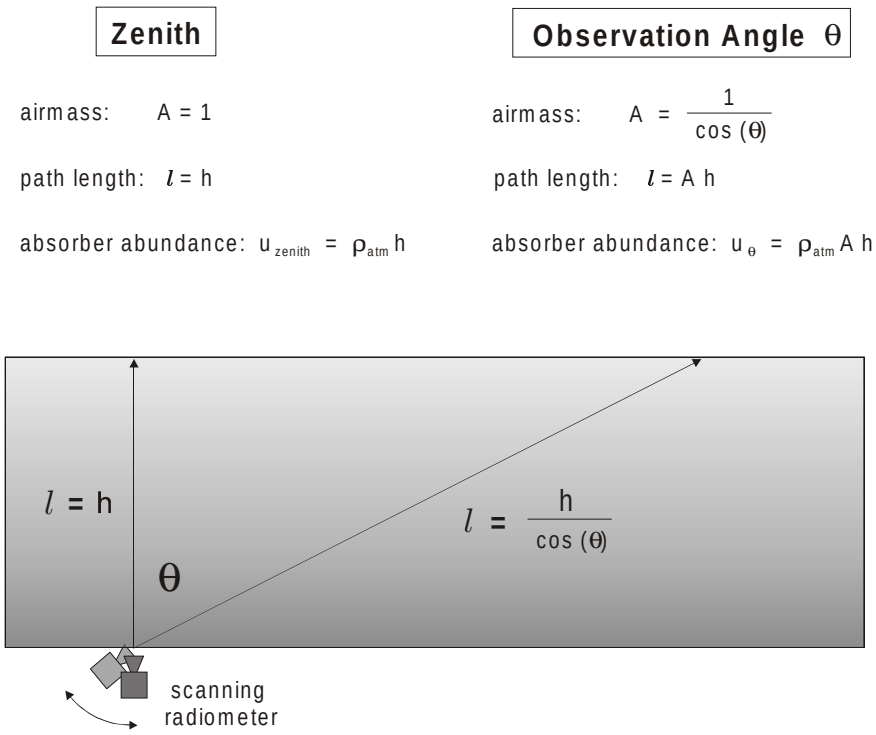

Figure 2.10: A *curve-of-growth* is obtained by the technique of *sky-dipping,* in which the radiometer scans a range of zenith angles through an assumed horizontally homogeneous atmosphere.

$$l = Ah \tag{2.4.2}$$

where A is airmass. If the atmosphere is considered to be horizontally homogeneous, and is characterized by an average density ρ_{atm}, then the absorber amount, u_θ, along the line-of-sight at any zenith angle, θ, will be related to the zenith absorber amount, u_{zenith}, by

$$u_\theta = \rho_{atm}\, A\, h \tag{2.4.3}$$

This relation may be incorporated into equations 2.3.48 through 2.3.53 to give the observed radiance as a function of zenith angle, or, equivalently, airmass, A, since

$$airmass = A = \tfrac{1}{\cos(\theta)} \tag{2.4.4}$$

The absorber amount u has standard SI units of $\mathrm{kg\,m^{-2}}$ since, as seen in equation 2.3.51 or 2.4.3, it specifies the mass of observed absorber normalized to a line-of-sight column of unit cross-sectional area. When applied to a vertical column of atmosphere, the absorber amount is referred to as a *column abundance*, w. Liquid water has a density of $1\ \mathrm{g\,cm^3}$ and hence a $1\,\mathrm{mm}$ thick layer of water on a $1\,\mathrm{m^2}$ surface area has a mass of $1\,\mathrm{kg}$. The units of column abundance, i.e. $\mathrm{kg\,m^{-2}}$, when applied to a vertical column of water vapor are then equivalent to a depth per unit area in $\mathrm{mm}\,pwv$. In the case of water vapor, a *curve-of-growth* is then labeled on the horizontal axis with absorber amount given as column abundance, w, in $\mathrm{mm}\,pwv$.

2.4.2 Radiometer Performance Derived From a *Curve-of-Growth*

If the infrared detector of the prototype radiometer responds linearly, its output signal will be related to the observed radiance via multiplication by a calibration constant called the instrumental responsivity with units of $V\,W^{-1}$. The quantity plotted on the vertical axis of a *curve-of-growth* can then be either the radiometer signal or the corresponding radiance. The quantity on the horizontal axis is absorber amount. The differential of this curve relates the error in the observed radiance to an error in absorber amount, as a function of absorber amount. In practice, the error in the measured radiometer signal (V) is determined by repeated observation of the blackbody references. The error in radiance is then derived by dividing this measured signal by the instrumental responsivity as will be discussed in Section 4.6. As demonstrated in Figure 2.11, the error in absorber amount is then found by projection of the radiance error onto the absorber amount axis. This error

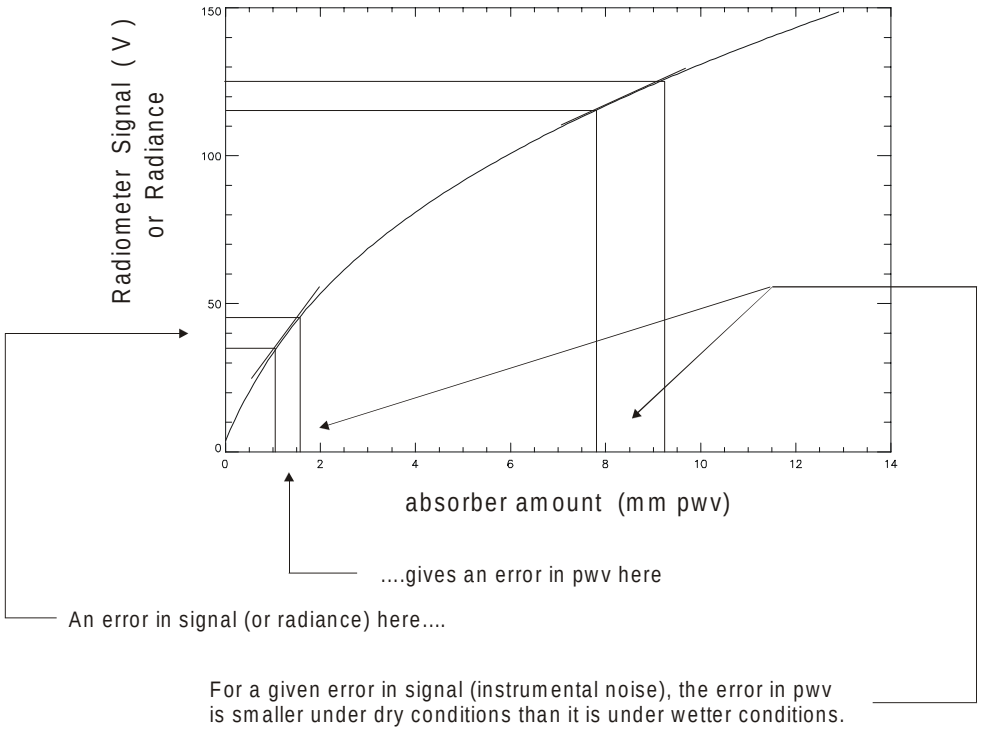

Figure 2.11: An illustration of the use of a *curve-of-growth* for calculating the resolution in absorber amount (i.e. precipitable water vapor) from the instrumental noise of the radiometer. This procedure can be reversed and used to specify radiometer noise performance for a target absorber amount resolution. The vertical axis of the *curve-of-growth* can be radiometer signal, or, after conversion via the instrumental responsivity, radiance. In the case where the *curve-of-growth* has been obtained from a spectral integration of computer synthesized emission spectra, the vertical axis is already in radiance.

can then be compared to the resolution requirements of radio telescope observatories such as ALMA as discussed in Chapter 1.

In the case where a numerical model of an atmosphere is available, an artificial *curve-of-growth* may be synthesized from it and, reversing the above procedure, may be used to estimate a radiometer detection performance necessary for a desired absorber amount resolution.

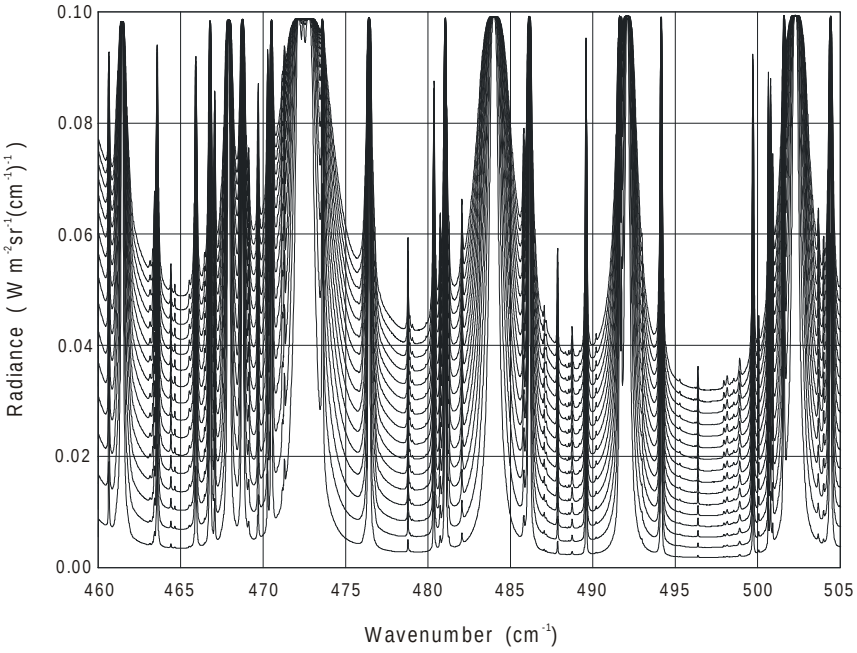

Figure 2.12: Computer simulated water vapor emission above Mauna Kea for a variety of column abundances ranging from $0.25 - 4.00$ mm pwv in steps of 0.25.

2.5 Computer Simulated Atmosphere Above Mauna Kea

The trial of the prototype radiometer was to be conducted at the JCMT and therefore a multi-layer model atmosphere [6] was used to simulate the water vapor emission above this site for the spectral region $450 - 500$ cm^{-1} for a variety of column abundances from 0.25 to 4.0 mm pwv. This simulation, shown in Figure 2.12, shows a mixture of strong and weak emission features.

Figure 2.13 shows the *curve-of-growth* determined from a spectral integration under the individual curves in Figure 2.12. The derivative of this *curve-of-growth* relates a variation of pwv to a variation of radiance as previously discussed. As seen from the figure,

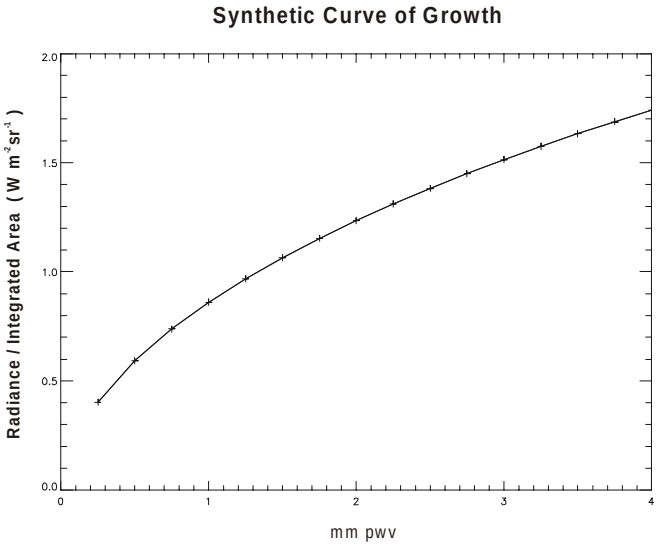

Figure 2.13: C*urve-of-growth* synthesized from the simulated emission above Mauna Kea shown in Figure 2.12.

the estimated emission radiance from the atmosphere under the condition of 1 mm *pwv* is approximately 0.85 $\mathrm{Wm^{-2}sr^{-1}}$ and the derivative of the *curve-of-growth* at 1 mm *pwv* is $\sim$ 0.45 $\mathrm{W\,m^{-2}sr^{-1}mm}\,pwv^{-1}$. These values were used in an initial feasibility study to estimate the performance required of the prototype infrared radiometer; this calculation will be reviewed in Section 3.2.

2.6 Distribution of Water Vapor in the Atmosphere

Ideally, the infrared radiometer should sample a volume that corresponds to the beam of the radio antenna for which phase correction is required. The effective volume of atmosphere sampled by a diffraction-limited radio telescope corresponds to a cylinder of the same diameter extending to the outer limit of the atmosphere. The infrared water vapor

radiometer, on the other hand, is a very compact device with a small collecting optic on the order of a few tens of centimeters. The challenge was to design the prototype such that it samples, as far as possible, the cylindrical beam of the radio antenna. It was therefore decided to design the field of view of the radiometer such that it sampled a patch of sky equal in size to the radio antenna at a range not shorter than the effective scale height of water vapor. As the prototype was to be tested at the JCMT, an estimate of the effective scale height of water vapor above Mauna Kea was required and radiosondes launched from the nearby Hilo airport provided such data.

If water existed only in the vapor phase, and in an isothermal atmosphere, then the vertical distribution would be given by the hydrostatic expression derived in section 2.3.4. Rewriting equation 2.3.15 in terms of particle density, N, and altitude, a, the vertical distribution of water vapor molecules is then given by

$$N(a) = N(0)\, e^{-\frac{a}{H}} \tag{2.6.1}$$

where $N(a)$ is the number density of water vapor molecules at an altitude a above the summit, $N(0)$ is the number density at the summit and H is the previously discussed scale height,

$$H = \frac{R\,T}{M_{H_2O}\,g} \tag{2.6.2}$$

applied to water vapor. Evaluation of equation 2.6.2 using a mean atmospheric temperature of 260 K yields a scale height for water vapor of 12.7 km, but since water vapor condenses out at temperatures below 273 K, the actual distribution could not be expected to follow equation 2.6.1. An *effective* scale height can be defined as the altitude at which the number

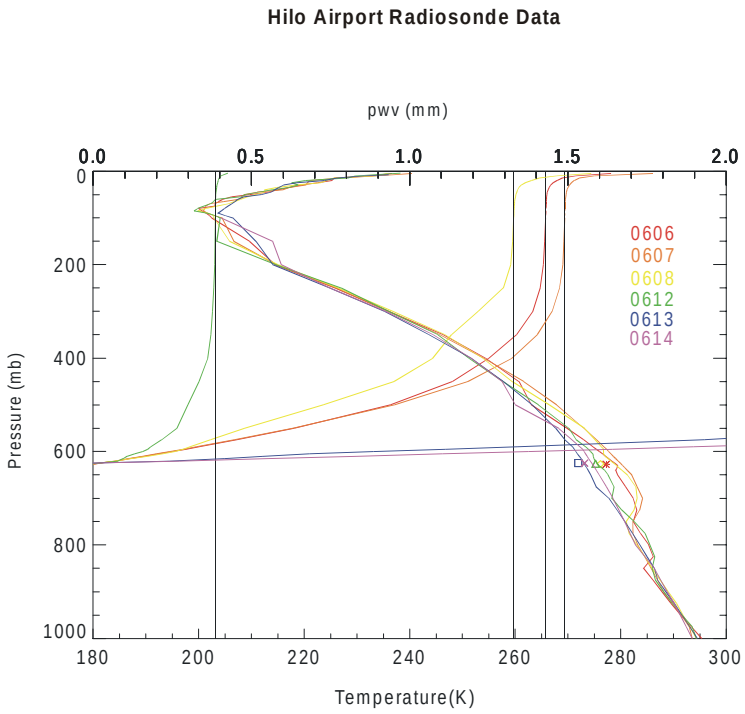

Figure 2.14: Radiosonde data for the atmosphere in the region of Mauna Kea giving atmospheric temperature and precipitable water vapor as a function of atmospheric pressure. Curves starting at the lower right in the figure represent pressure-temperature profiles. Curves starting from the left in the figure represent pressure-pwv profiles.

density of water vapor molecules, integrated from ground level, falls to e^{-1} of the total integrated amount. This quantity can be evaluated numerically from radiosonde data such as that from the Hilo radiosondes. This effective scale height can be expected to be highly variable as it reflects the changing conditions above Mauna Kea but typical values of the numerically derived scale height can be taken as a good criterion for the sampling range of the prototype radiometer.

The Hilo airport is situated approximately 43 km to the east of Mauna Kea and radiosondes are launched from this location twice a day, at 2 p.m. and 2 a.m. local Hawaiian

time. These radiosonde data are accessible on the web at:

http://hokukea.soest.hawaii.edu/current/raob/ito/text/

An example of a week of such data is shown in Figure 2.14 where integrated pwv (curves starting from the left) and atmospheric temperature (starting from the lower right) are plotted as a function of atmospheric pressure. It is seen from this figure that the integrated precipitable water vapor is largely contained in a region below $\sim 500\,\mathrm{mb}$. It is also seen that the total column abundance varied widely during this week; the driest day had a total column abundance of 0.4 mm pwv, another group of three days had an average value of ~ 1.4 mm pwv, and on two days the pwv was indeterminate, as evidenced by the two almost horizontal curves representing heavily overcast conditions.

Evaluating the scale height formula with an average atmospheric molecular mass of $0.028\,\mathrm{kg\,mol^{-1}}$ and an average atmospheric temperature of 260 K yields

$$H = \frac{RT}{m_{atm}\,g} = \frac{8.314 \cdot 260}{0.028 \cdot 9.8} = 7.88\,\mathrm{km} \qquad 2.6.3$$

Using this scale height and the typical atmospheric pressure at the summit of 626 mb, the altitude at which the pressure drops to 500 mb can be derived via the hydrostatic equation:

$$a = -H\,\ln(\tfrac{P}{P_s}) = -(7.88)\ln(\tfrac{500}{626}) = 1.77\,\mathrm{km} \qquad 2.6.4$$

Given the approximate nature of the above calculation, an effective water vapor scale height was taken as 1 km. The infrared radiometer was therefore designed to sample an area of $\sim 10\,\mathrm{m}$ diameter, the typical size of a radio antenna, at a range of 1 km. These

values then establish an optical field of view for the design of the prototype radiometer (Section 3.4.1).

Chapter 3

Radiometer Design and Construction

3.1 Overview

This chapter presents details of the design and construction of the prototype radiometer. The starting point in the design process were the following four input parameters presented in the preceding chapters: 1) the expected atmospheric water vapor radiance of ~ 0.85 W m^{-2}sr^{-1} obtained via computer simulation (Section 2.5), 2) the atmospheric sampling criterion of a 10 m diameter patch of sky at a range of 1 km, chosen to match as closely as possible the atmospheric column of the proposed ALMA radio antennae at the effective scale height of water vapor (Section 2.6), 3) a working spectral range of $\sim 450-500$ cm^{-1} within which water vapor infrared emission could be expected to be isolated from that due to other atmospheric species (Section 1.3.1) and 4) the desire to measure the column

abundance of water vapor to a resolution of $\sim 1\,\mu\mathrm{m}\,pwv$ in an integration time of $\sim 1\,\mathrm{s}$ (Section 1.5).

The first step was to conduct a feasibility study to establish the viability of an infrared approach to water vapor measurement. Assuming certain component characteristics such as the spectral bandpass of the infrared filter and sensitivity of commercially available detectors, this calculation determined the approximate size of the optics required for the prototype and is reproduced in Section 3.2. The remainder of the chapter describes in detail the design and construction of the prototype including optical, electronic, mechanical and software aspects. Section 3.3 begins with an overall view of the radiometer system which consisted of three principle components; an instrument platform, an electronics package and a laptop computer executing the control software; each of these parts of the system is then discussed in detail. Section 3.4 describes the design of the instrument platform which included optical components, blackbody references, detector dewar and detector preamplifier. Section 3.5 describes the electronic instrumentation and Section 3.6, the instrument control software.

3.2 A Preliminary Feasibility Calculation

The spectral region of $\sim 450 - 500\,\mathrm{cm}^{-1}$ was the target spectral region for the prototype radiometer. The radiance from water vapor above Mauna Kea predicted by the computer model for this spectral region under conditions of $1\,\mathrm{mm}\,pwv$ was 0.85 mW. The atmospheric sampling criterion, defining a field of view for the prototype, was chosen to

sample a 10 m diameter patch at a range of 1 km. A primary mirror diameter of 125 mm was chosen as a good compromise between collecting area, cost and the compact design envisioned for the radiometer but was subject to revision pending the outcome of the signal-to-noise calculation. Using these figures, a preliminary calculation was made to ensure that an infrared approach was feasible using commercially available infrared detectors and filters under the somewhat pessimistic assumption of 10 % optical efficiency. The calculation proceeded as follows.

The collecting area was

$$A = \tfrac{\pi}{4}\,(0.125)^2 = 1.2\ \times 10^{-2}\ \mathrm{m}^2 \qquad 3.2.1$$

Using the sampling criterion of a 10 m diameter patch at a range, R, of 1 km, the field of view of the radiometer was

$$\Omega = \tfrac{A_{sample}}{R^2} = \tfrac{\frac{\pi}{4}(10)^2}{(1000)^2} = 7.9\ \times 10^{-5}\ \mathrm{sr} \qquad 3.2.2$$

The predicted radiance of water vapor above Mauna Kea was $\sim 0.85\ \mathrm{W\,m^{-2}sr^{-1}}$ (Section 2.5). The total optical efficiency, η, was assumed to be 10 % which yielded a total collected power

$$\Phi = \eta\, L_{H_2O}\ A\ \Omega\ =\ 8.2 \times 10^{-8}\ \mathrm{W} \qquad 3.2.3$$

Discussions with detector manufacturers indicated that a photoconductor sensitivity performance of $D^* = 2 \times 10^9\ \mathrm{cm}\sqrt{\mathrm{Hz}}\ \mathrm{W}^{-1}$could be expected for a mercury-cadmium-telluride (MCT) detector element operating in the region of $500\,\mathrm{cm}^{-1}$. With an area of $1\,\mathrm{mm}^2$, the detector noise-equivalent-power (NEP) was

$$NEP = \frac{\sqrt{Area}}{D^*} = \frac{\sqrt{1\times10^{-2}}}{2\times10^{9}} = 5\times10^{-11}\ \mathrm{W}\sqrt{\mathrm{Hz}}^{-1} \qquad 3.2.4$$

The resulting signal-to-noise ratio in a 1 s interval became

$$S/N = \frac{\Phi}{NEP} = \frac{8.2\times10^{-8}}{5\times10^{-11}} \simeq 1600 \qquad 3.2.5$$

The derivative of the computer synthesized *curve-of-growth* (Figure 2.13), relating the error in observed water vapor radiance to the error in precipitable water vapor for the case of Mauna Kea was 0.45 $\mathrm{W\,m^{-2}sr^{-1}(mm}\,pwv)^{-1}$ under conditions of 1 mm pwv. Using the signal-to-noise ratio of 1600 calculated above and the predicted radiance of 0.85 $\mathrm{W\,m^{-2}sr^{-1}}$, this translated to an error in precipitable water vapor,w, of

$$\Delta\, w = \frac{\frac{0.85}{1600}}{0.45} = 1.2\ \mu\mathrm{m}\ pwv \qquad 3.2.6$$

for a $1\,\sigma$ detection in a 1 s integration.

This preliminary calculation indicated that the challenging measurement resolution of $\sim 1\ \mu$m pwv could be achieved using a collecting optic 125 mm in diameter and using a commercially available LN_2-cooled MCT photoconductive detector, band limited to the spectral range $450 - 500\ \mathrm{cm^{-1}}$.

The infrared filter required to define the spectral bandpass of the system could be accomplished either by a bandpass type filter or, alternatively, an edge filter used in conjunction with the sharp long wavelength detector cut-off characteristic of MCT detectors. These filters are not commercially available, but fortunately an experimental filter with a passband of $462 - 505\ \mathrm{cm^{-1}}$ was purchased from the University of Reading Infrared

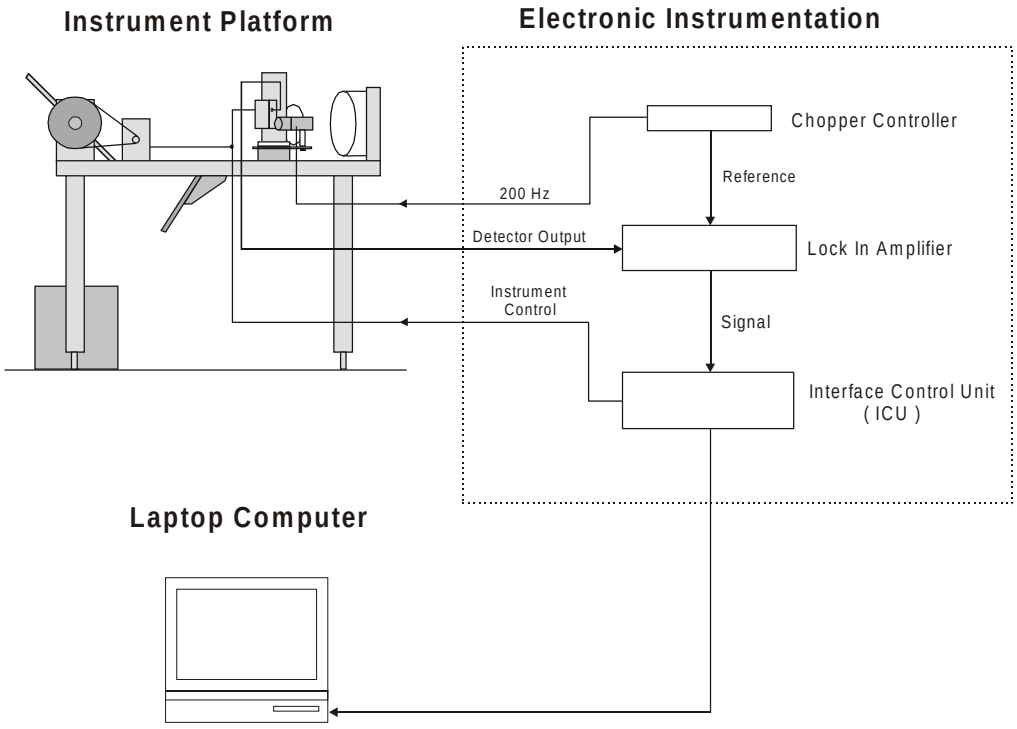

Figure 3.1: An overall view of the prototype radiometer showing the three principle parts of the system; the instrument platform, the electronic instrumentation and the laptop control computer.

Multilayer Laboratory, and this provided the last element needed for the construction of the prototype infrared water vapor radiometer.

3.3 An Overall System View of the Radiometer

Figure 3.1 shows an overall view of the water vapor radiometer which is comprised of three principle components; an instrument platform, the electronic instrumentation and a laptop control computer. The electronic instrumentation consists of a chopper wheel driver unit, a lock-in amplifier and an interface control unit (ICU) which houses power supplies, an A/D converter for the signal output from the lock-in and a parallel port computer interface.

Finally, a laptop computer runs the control software. The design and construction of each of these components is discussed below.

3.4 The Instrument Platform

The instrument platform contained all the optical components, two blackbody references and LN_2-cooled infrared detector dewar assembly with detector preamplifier and reflective optical chopper. The optical system consists of a flat scanning mirror directing light to an off-axis paraboloid having a focal point on the detector. The scanning mirror provided a range of observable zenith angles from 0 to 70.38^o and hence *curves-of-growth* could be obtained representing an airmass range from $1 - 3$.

The cold blackbody consisted of an open flask of LN_2 placed on the floor directly below the scanning mirror assembly and into which was placed a disc of $Eccosorb^{TM}$ [15], a common absorber at submillimeter wavelengths, so as to eliminate reflections from the mirror-like bottom of the flask. While the temperature of the ambient blackbody changed with time, the temperature of the cold blackbody at the reduced atmospheric pressure on the summit of Mauna Kea could be taken as a constant 73 K.

The ambient blackbody consisted of an aluminum plate coated with a thermally conductive epoxy ($Epo - Tek$ 920) matrix of carbon black (2 % by weight carbon black) whose surface was imprinted with a uniform grid of square pyramidal indentations by means of a plastic mold. The emissivity of this material in the spectral region of 20 μm has been measured to be greater than 0.99 [16]. The plate was mounted with insulating support

brackets on the underside of the platform. The temperature of the plate was to have been measured with a sensor embedded in the center. Unfortunately this sensor was later discovered to have produced erroneous readings. Ambient temperature readings recorded from the JCMT outside air temperature sensor were then assigned to the ambient blackbody reference in the subsequent analysis. A detailed top and side view of the instrument platform is shown in Figure 3.2.

3.4.1 Parabolic Primary Mirror Design

An off-axis paraboloid was chosen as the primary focusing optic so as to avoid occultation of the optical beam by a secondary mirror assembly and hence maximize the optical energy collected for a given primary mirror diameter. This approach also resulted in a simple and compact radiometer design. The diameter of the paraboloid was chosen to be 125 mm (Section 3.2); due to the previously determined field of view requirement and the standard 1 mm^2 detector element, the focal length was fixed by the conservation of the optical throughput of the system.

Referring to the schematic of the optical system shown in Figure 3.3, conservation of the throughput of the optical system requires that

$$A_d \, \Omega_d = A_p \, \Omega_p \tag{3.4.1}$$

where A_d is the area of the detector, Ω_d is the solid angle viewed by the detector, A_p is the area of the paraboloid and Ω_p is the solid angle subtended by the 10 m diameter atmospheric

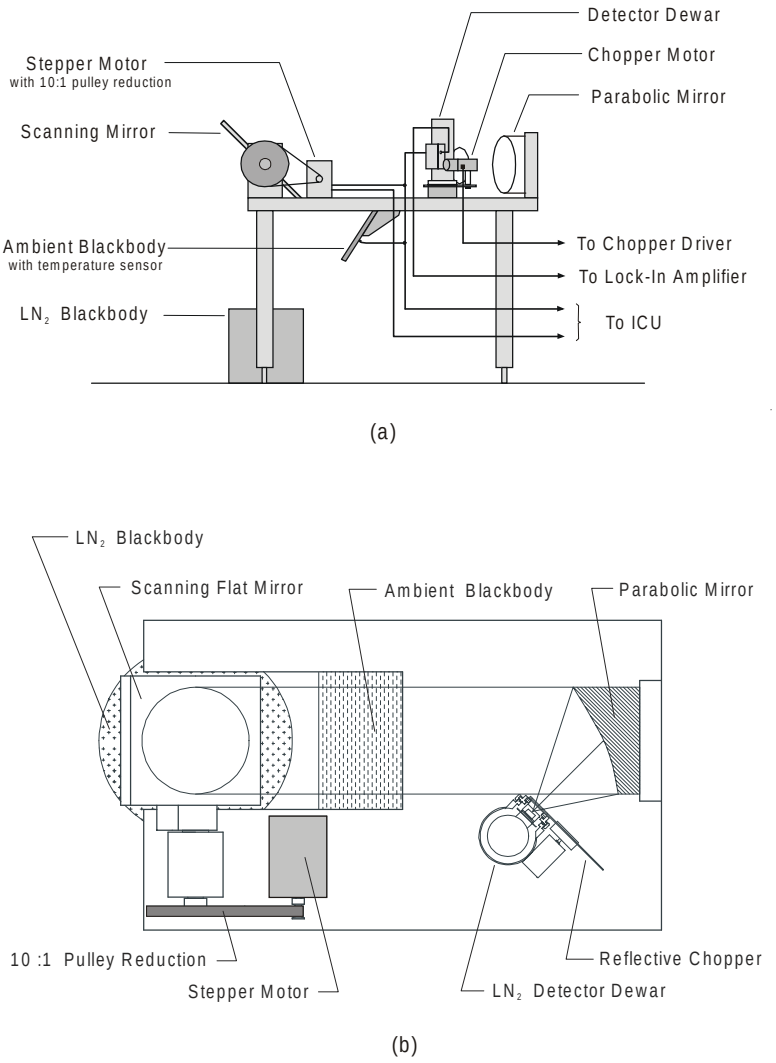

Figure 3.2: Side view (a) and top view (b) of the instrument platform.

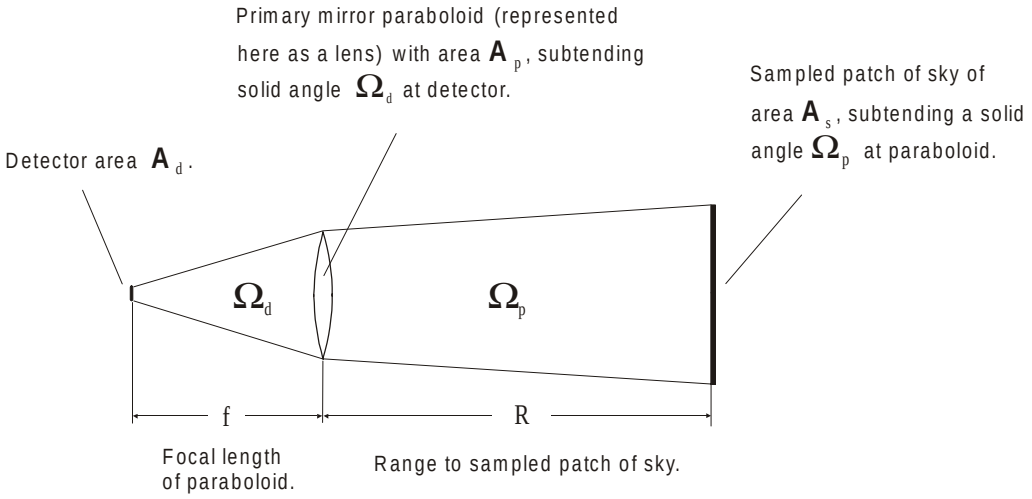

Figure 3.3: A schematic of the equivalent optical system of the prototype radiometer.

sampling area at the paraboloid. A good approximation of the solid angle subtended by a sampled area A_s at the paraboloid at a distance R is $\Omega_p = A_s/R^{\,2}$, and, similarly, the solid angle subtended by the paraboloid at the detector is $\Omega_d = A_p/f^{\,2}$. Equation 3.4.1 can then be rearranged to specify a focal length

$$f = R\sqrt{\frac{A_d}{A_s}} = R\sqrt{\frac{d_d^2}{d_s^2}} \qquad 3.4.2$$

where d_d is the diameter of the detector element and d_s is the diameter of the source area (i.e. 10 m). Here the effective area of the 1 mm^2 square detector element is taken as a circle of diameter $d_d = 1\,\mathrm{mm}$. The focal length of the paraboloid is then seen to be determined by d_d, d_s, and R, all of which having been previously determined, and is independent of the diameter of the paraboloid. Inserting values into equation 3.4.2 yields a focal length of

$$f = (1000)\sqrt{\frac{(0.001)^2}{(10)^2}} = 0.1\,\mathrm{m} \qquad 3.4.3$$

Having established a nominal focal length consistent with the desired radiometer

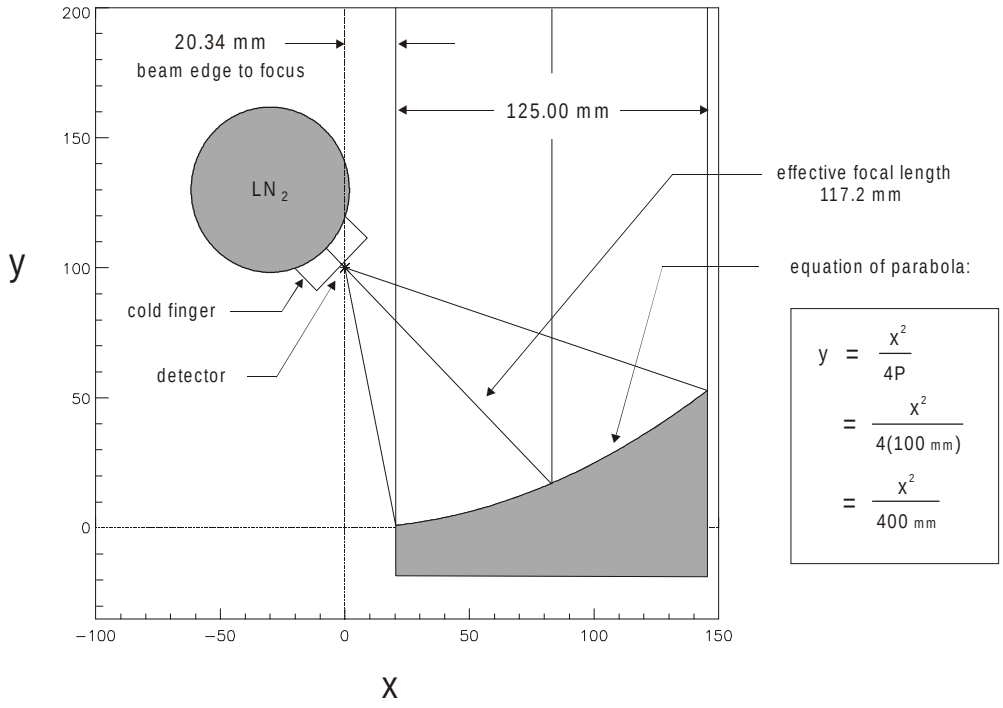

Figure 3.4: Details of the IDL-assisted final design of the parabolic primary mirror.

field of view, it remained to choose an off-axis throw angle, which, due the focal length, implied a certain clearance from the focal point to the edge of the optical beam. The dewar assembly had to be placed such that the focus of the paraboloid is at the detector element while the dewar itself is kept from interfering with the optical beam. Angles of throw much greater than about 45 degrees would provide a greater clearance for the dewar assembly but would result in an unreasonably deep paraboloid. The focal length calculated above and the previously determined paraboloid diameter of 125 mm were taken as target figures for the final design of the paraboloid but were subject to small revisions that the choice of throw angle, detector field of view and dewar clearance demanded.

An IDL program (*Parabola_Design*) was written to experiment with these trade-offs. With the paraboloid diameter set at 125 mm, the remainder of the parameters were iteratively adjusted while keeping the F-number of the paraboloid as close to unity as possible so as to avoid the difficulties associated with the manufacture of deep paraboloids. The graphical output of this program showing the final arrangement is given in Figure 3.4.including the equation for the paraboloid in the coordinate system shown with x, y and 400 having units of millimeters. A summary of the optical properties of the paraboloid is given in Table 3.1.

Table 3.1: Summary of paraboloid design parameters.

Design Parameter	Value
diameter	125 mm
focal length	117.2 mm
F-number	0.937
focal point offset from beam edge	20.34 mm

The parabola was diamond turned from a solid block of aluminum by *Lumonics Inc.*, (Ottawa), and was fabricated with an additional 25 mm of material below the x axis, as shown in the figure, to allow mounting holes to be drilled in the rear of the mirror itself. The paraboloid was bolted flat against a 25 mm thick aluminum mounting plate without provision for adjustment. An X-Y dewar assembly mounting platform provided focus adjustment in a horizontal plane while the vertical position of the dewar was adjusted by machining the thickness of the mounting flange supporting the detector dewar. Figure 3.5 provides a detail of the top view of the final design of the optical system and shows the close tolerances required to keep a 125 mm diameter optical beam while simultaneously

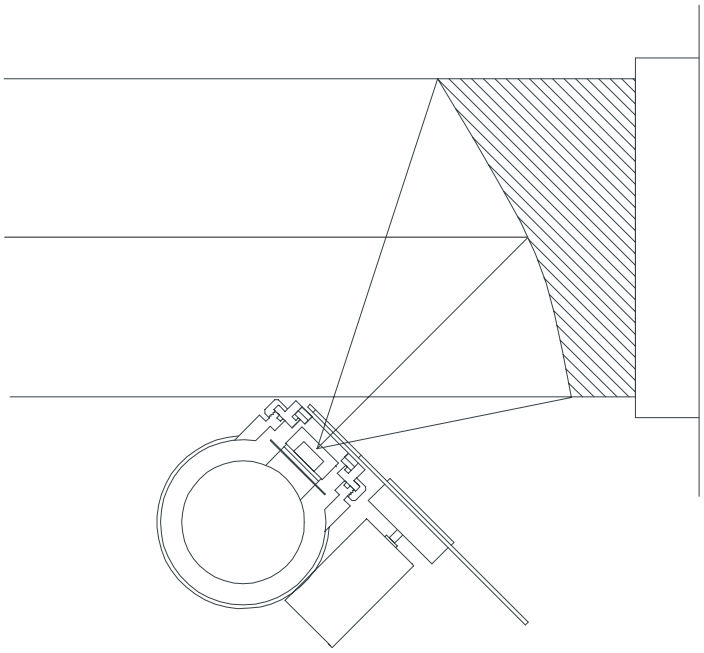

Figure 3.5: A top view detail of the optical system showing the placement of the detector dewar at the focus of the parabolic primary mirror.

accommodating the requirements of the detector dewar assembly. A protective shroud was incorporated around the top and sides of the paraboloid and provided a degree of protection from the environment.

3.4.2 Scanning Mirror Assembly

The scanning mirror assembly was designed to provide *curves-of-growth* for an airmass range of $1 - 3$. Since, as discussed in Section 2.4.1, $airmass = 1/\cos(zenith\ angle)$, this range corresponds to a zenith angle range from $0 - 70.38^o$. The scanning mirror was actuated via a 200 step/rev stepping motor (400 step/rev in half stepping) followed by a $10:1$ pulley reduction arrangement as shown in Figure 3.6. The control computer tracked

the position of the scanning mirror by counting step pulses issued to the driver unit. A reference position was provided by an optical switch mounted on the scanning mirror axle block with the interrupting blade fastened to the large pulley of the scanning mirror axle in such a way as to provide interruption of the opto-switch when the mirror viewed the nadir. Upon system start up, the computer drove the scanning mirror toward the nadir until the reference signal was obtained. The scanning mirror position register in the control program was then reset to zero. Subsequent mirror movement was then tracked by the computer via this register.

The 10-turn potentiometer was attached to the stepper motor axle shaft so as to provide a secondary (analog) means of monitoring the scanning mirror position. The 10-revolution range of the stepper motor axle provided a one turn range of the scanning mirror axle and, hence, was more than twice that needed to provide observations from $1-3$ airmasses. This enabled the 10-turn potentiometer to be operated in the center of its rotational range. Nevertheless, a means had to be provided to prevent the computer from driving the motor beyond the limits of the potentiometer in the event of a failure of the control program. As also seen in Figure 3.6, a limit switch was placed on the axle block on the opposite side from the opto-switch and two round-headed screws were installed on the inner face of the drive pulley 95^o apart so as to actuate the switch if the scanning mirror left the range of allowed movement. The normally high signal from the limit switch was ANDed with the step pulses issued by the control program at the input of the stepper driver unit to provide a hardware level emergency lock-out function.

The dimensions of the flat scanning mirror were chosen slightly oversized so as to

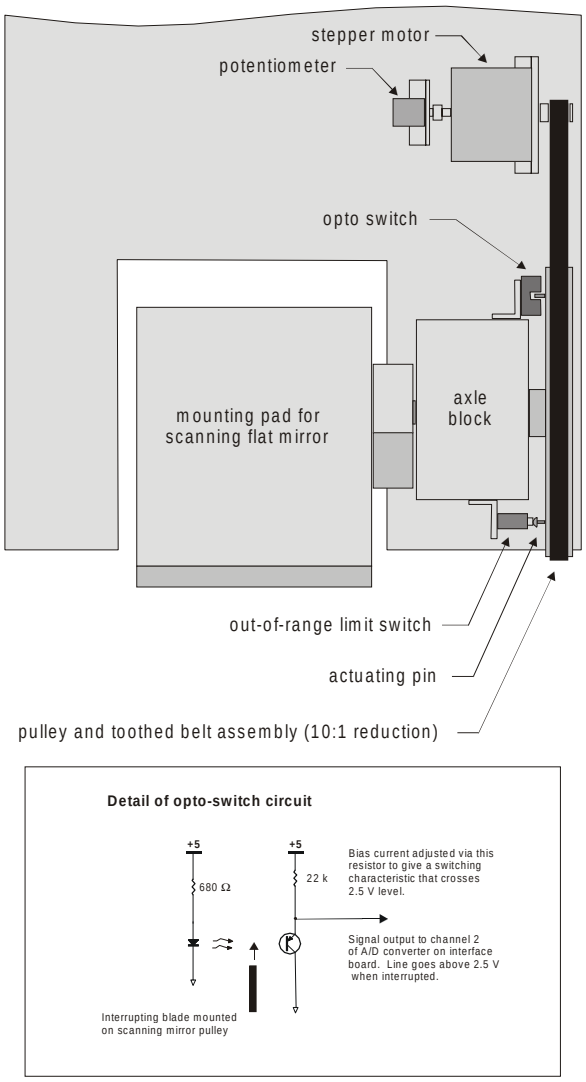

Figure 3.6: A top view of the scanning mirror assembly showing the nadir reference position opto-switch and out-of-range limit switch. A detail of the opto-switch circuit is shown in the inset.

accommodate the divergence of the optical view from the paraboloid due to the field of view of the instrument, as well as any small misalignment of the optical axis. The field of view of the instrument was

$$\theta \simeq \frac{1/2 \cdot 10\, m}{1000\, m} = 5 \times 10^{-3} \text{ rad} \tag{3.4.4}$$

The distance along the optical axis from the surface of the parabolic primary mirror to the center of the flat mirror was 460 mm and hence over this range the optical beam diverged a distance of

$$d = 460 \cdot 5 \times 10^{-3} = 2.3 \text{ mm} \tag{3.4.5}$$

beyond the perimeter of a 125 mm diameter circle as projected onto the surface of the scanning mirror. In sizing the mirror width, a clearance of 12.5 mm was allotted to each side of the projected 125 mm paraboloid diameter, making the mirror width 150 mm. The projected distance of the optical beam along the scanning mirror in the vertical direction when at its maximum relative angle of 45^o with respect to the optical axis of the system is a factor of $\sqrt{2}$ times the projected paraboloid diameter. To this was added a clearance of $\sqrt{2} \times 12.5$ mm making the long dimension of the scanning mirror 212 mm. The mirror was fabricated from optical glass and coated with a layer of aluminum followed by a coating of SiO a few nanometers thick for protection against the environment.

3.4.3 Infrared Detector

The infrared detector was a mercury-cadmium-telluride (MCT) device, supplied by *Kolmar Technologies Inc.* [17], designed for operation at 77 K. The detector specifications

supplied by the manufacturer are listed in Table 3.2:

Table 3.2: Infrared detector characteristics.

Detector Parameter	Value
active area	1 mm^2
responsivity	45.33 V/W
cut off wavelength (max)	22.15 μm
resistance @ 77 K	32 Ω
nominal bias voltage	0.45 V
D* (@10kHz)	2.88 x 10^9 cm$\sqrt{\text{Hz}}\text{W}^{-1}$

The specifications indicate a 10 % response cutoff wavelength of 22.15 μm (451 cm^{-1}) and this makes it a reasonable match with the infrared filter as discussed in Section 3.4.4. The resistance of the device was measured to be 32 Ω at 77 K and the optimal bias voltage of 0.45 V quoted by the manufacturer corresponds to a bias current of 14 mA. Verbal communication with the manufacturer suggested that slightly better performance could be attained by increasing this value provided the breakdown voltage of 0.8 V for the device was not exceeded. Performance tests in the laboratory revealed no appreciable increase in signal-to-noise with increasing bias voltage and the recommended bias current of 14 mA became the target current for the preamplifier design.

3.4.4 Optical Filter

The narrow-band, infrared interference filter from the University of Reading, UK, was supplied with a response curve for normally incident radiation and is shown in Figure 3.7. In practice, the filter response should be modified to take into account a wavelength shift that occurs for radiation incident at an arbitrary angle. Since radiation from the parabola

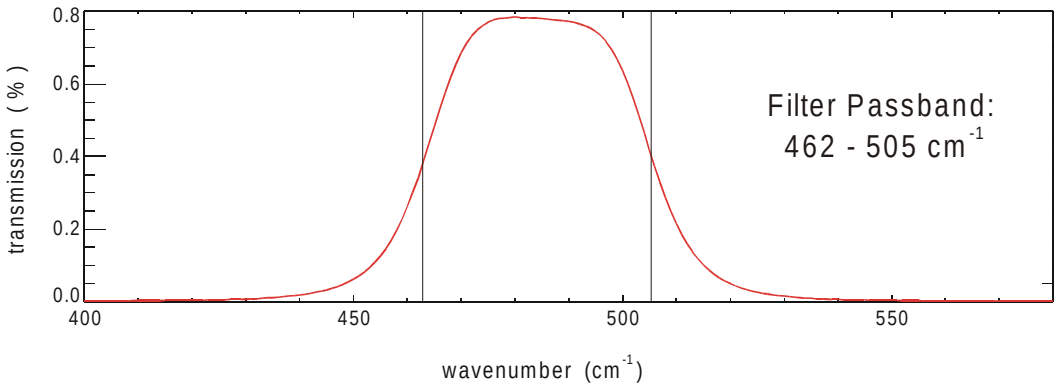

Figure 3.7: The spectral response of the infrared passband filter.

enters the filter as a rapidly converging beam, the circular area of the filter could be divided into annuli and the contribution from each corrected for wavelength and weighted by area. The total filter response would then be taken as the sum of these. Without a detailed knowledge of the optical and thermal properties of the filter required to perform the above calculation, the normally incident bandpass response of $462 - 505\,\mathrm{cm}^{-1}$ was assumed for the filter.

3.4.5 Detector Element Mounting Details

A cross-section of the detector mounting arrangement on the cold finger of the dewar is shown in Figure 3.8 and includes the placement of the infrared filter and optical window. Also seen in the figure is the chopper blade which was fabricated from mirror-finish stainless steel with the reflective side facing the detector element. The chopper motor and LN_2 dewar are mounted on a common base plate.

The detector and filter are both contained in a two piece copper flange mounted on the dewar cold finger and are thus both held at $73\,K$ (the boiling point of LN_2 on the summit of Mauna Kea). The outer part of the two-piece unit holds the infrared filter against the inner part which houses the detector in a light-tight enclosure. A thin copper washer is seated in the recess on the outermost face of the assembly and functions as the field defining aperture. The size of the hole in the aperture was determined by trial and error in the lab so as to produce a 60^o field of view.

The optical window was fabricated from a thin ($\sim$ 75 μm) polypropylene sheet which provides excellent transmission at a wavelength of 20 μm. The sheet was uniformly stretched in a cylindrical jig, sandwiched between two steel washers using superglue as an adhesive on both sides, trimmed around the circumference and then placed within an aluminum flange as seen in the figure. An O-ring provided the vacuum seal of the flange against the inner steel washer and a retaining cap secured the flange against another O-ring seal on the dewar body. The optical window was held in place by atmospheric pressure.

3.4.6 Optical Chopping Blade and Dewar Assembly

The optical chopping blade was fabricated from a mirror finish stainless steel using the process of *spark erosion machining.* This process eliminates any stress induced flaws and, combined with the mirror-like finish of the steel, produced a blade with a high quality optical surface. The reflective side faced the dewar and provided the detector with an alternating view of the radiation from the paraboloid and an unfocused view of itself (i.e. a

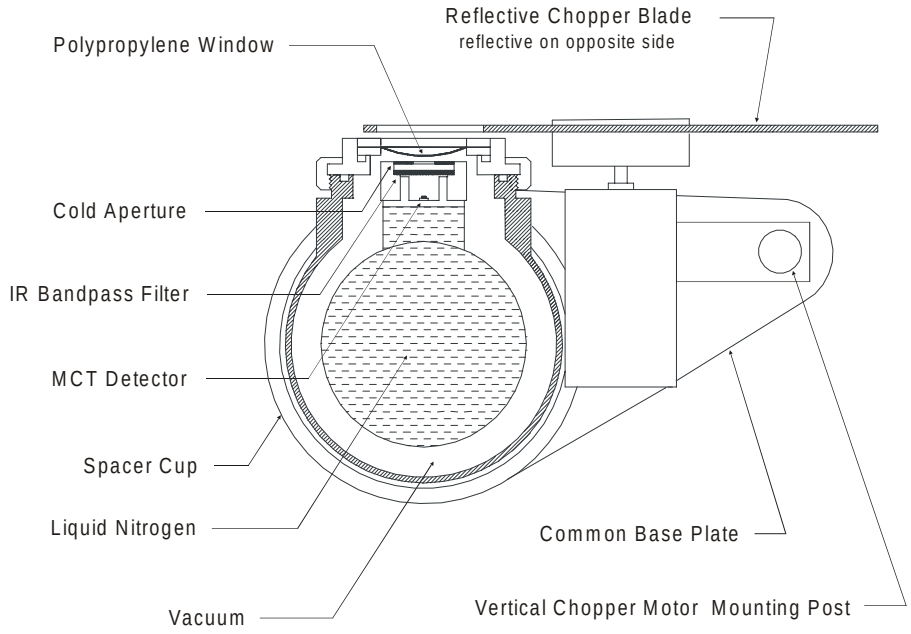

Figure 3.8: Detail of detector dewar showing mounting arrangement for MCT detector element, infrared filter and reflective chopper.

73 K environment) together with the emission from a very low emissivity ambient surface. This design was chosen to produced a chopped signal of higher stability than would be expected from a non-reflective blade experiencing the same temperature variations. The chopper wheel was machined with 5 slots which, when rotated at 40 revolutions per second, provided a 200 Hz modulation of the optical beam. The chopper blade motor was mounted on a vertical post so as to provide Z axis position adjustment. The post was mounted, along with the dewar, on a common base plate, as seen in Figure 3.8, which allowed the entire assembly to be moved as a whole in focus adjustment.

The dewar+chopper assembly was then fixed on an optical X-Y mounting platform, the X axis of which coincided with the optical axis of the parabola, as seen in Figure 3.5. The final focus position was achieved by adjustment of the X,Y, and Z positioning of the

detector assembly with the detector viewing a hot plate of diameter 150 mm at a distance ~ 4 m.

3.4.7 Detector Preamplifier Construction

The requirements for the detector preamplifier were that it be low noise, compact in size and have a temperature compensated biasing arrangement since the instrument was intended for outdoor operation over an anticipated temperature range on Mauna Kea from -10 to $+20^oC$. The LN_2 dewar was supplied by *Kolmar Technologies Inc.* and included a small housing for a preamplifier incorporated on the side. The dimensions of the housing were $38 \times 70 \times 19$ mm and the preamplifier board, connector hardware and some cabling had to fit within this volume. Figure 3.9 shows a photograph of the preamplifier construction.

The low noise requirement of the preamplifier was important since a large gain was used in the initial stage of amplification. Since the cold resistance of the MCT detector element was $32\,\Omega$, the thermal voltage noise contribution was minimal; thus a low voltage noise preamplifier with similarly small input resistances would result in a low overall noise figure. The *LinearTechnology* LT 1028 operational amplifier (op-amp) has one of the smallest voltage noise specifications among commercially available op-amps ($\sim 1\,\mathrm{nV\,Hz^{-1/2}}$ at 200 Hz) and is particularly suited to low-impedance source applications where its relatively high current noise ($\sim 1\,\mathrm{pA\,Hz^{-1/2}}$ at 200 Hz) does not contribute significantly to the overall noise figure.

A constant current biasing arrangement was used with the detector to provide a

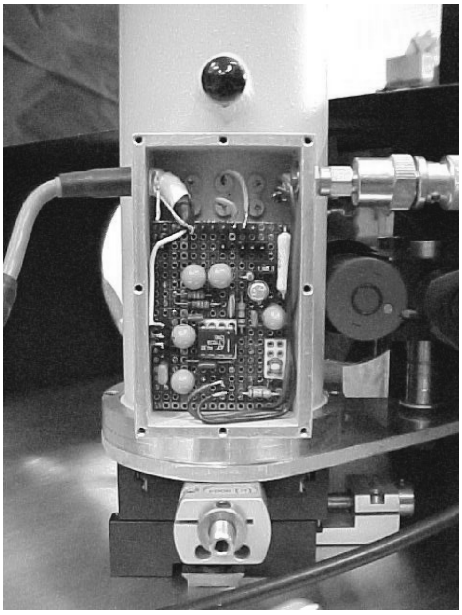

Figure 3.9: A view of the rear of the detector dewar showing the preamplifier installation.

linear relation between optical input and voltage output. The op-amp was operated in a non-inverting mode and configured with a gain of 2000. A bandpass of $\sim 20\,\mathrm{Hz} - 2000\,\mathrm{Hz}$ was selected to provide $-3\,dB$ cut-off points an order of magnitude on either side of the modulation frequency of 200 Hz. A schematic of the preamplifier is given in Figure 3.10.

Low resistance values were needed for R_{in}^{+} and R_{in}^{-} at the preamplifier input to match the low source impedance of the detector element and to avoid voltage noise due to the op-amp input noise current. The conflicting requirement was that a physically small, and therefore relatively small value, input coupling capacitor, C_{in}, had to be used to form the input high pass filter with a break frequency a decade below the 200 Hz modulation frequency. C_{in} consisted of two $100\,\mu$F tantalum capacitors in parallel and, with $R_{in}^{+} = 50\,\Omega$, the lower $-3\,dB$ cut-off frequency was

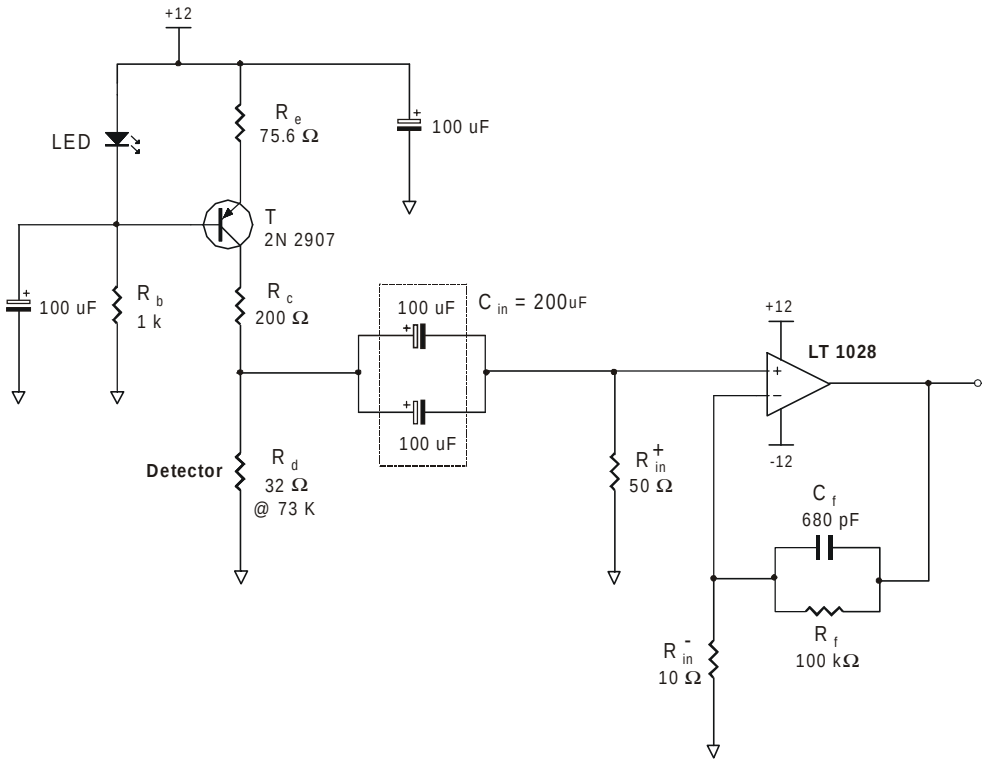

Figure 3.10: A schematic of the preamplifier.

$$f_l = \frac{1}{2\pi R_{in} C_{in}} = \frac{1}{2\pi(50)(200\times10^{-6})} \;=\; 16 \text{ Hz} \tag{3.4.6}$$

To produce a gain of ~ 2000 in the passband of the preamplifier a feedback resistance of $R_f = 100\,\text{k}\Omega$ was required. A feedback capacitor $C_f = 680\,\text{pF}$ resulted in an upper cut-off frequency

$$f_u = \frac{1}{2\pi R_f C_f} = \frac{1}{2\pi(100\times10^{3})(680\times10^{-12})} \;=\; 2340\,\text{Hz} \tag{3.4.7}$$

During construction of the preamplifier it was noted that combining resistors in series or parallel to synthesize a specific resistance resulted in a substantially increased noise figure of the preamplifier, possibly due to thermo-electric effects in the solder joints.

Single resistance values as close as possible to the target values were therefore used in the fabrication of the preamplifier. This construction philosophy was particularly important in the detector biasing portion of the circuit.

The preamplifier incorporated temperature compensation in the constant current generator biasing the detector since the radiometer was to operate over a wide range of temperatures. The operation of this part of the circuit, seen in the upper left of Figure 3.10, was as follows. A well defined voltage drop of 1.80 V is first established across the LED by biasing it well into conduction with the 1 kΩ resistor, R_b. Assuming the temperature characteristic of the pn junction of the LED is the same as that of the pn base-emitter junction of the $2N2907$ pnp transistor, T, the voltage at the emitter of the transistor was 12 V−1.8 V+0.6 V= 10.8 V and independent of temperature. A temperature independent voltage of 1.2 V was thus established across R_e. The current through the detector, I_d, was then determined by R_e using

$$I_d = \frac{1.2\,V}{R_E} \qquad 3.4.8$$

In the final circuit a 75.5 Ω 1 % metal film resistor was selected for R_e, resulting in a bias current of 15.3 mA, close to the optimal value suggested by the manufacturer.

The inclusion of the 200 Ω resistor, R_c, was necessary to decrease the power dissipation of the transistor T. During final testing of the preamplifier in the laboratory it was found that operation without R_c resulted in a 65^{o}C case temperature versus 54^{o}C with R_c included (the transistor can operate with a maximum case temperature of 200^{o}C). Since the atmospheric pressure, and hence cooling efficiency, on the summit of Mauna Kea is

approximately $\sim 60\,\%$ that in Lethbridge, it was decided to include R_c in the bias circuit to give an extra margin of safety.

3.4.8 Preamplifier Noise

The constant current source circuitry used to bias the detector element was considered to be subject to refinement in subsequent versions of the radiometer whereas the detector and op-amp configuration is expected to remain unchanged. A preamplifier noise analysis without including contributions by the constant current source will then give an indication of the minimum noise level attainable using the LT 1028 op-amp and the values for R_d, R_{in}^+, R_{in}^-, and R_f shown in Figure 3.10.

The thermal voltage noise density generated by the detector element at the input of the op-amp is

$$\begin{aligned} e_1 &= e_{n_{\text{detector}}}\left(\frac{R_{in}^+}{R_{in}^+ + R_d}\right) \\ &= \sqrt{4kTR_d}\left(\frac{50}{50+32}\right) \\ &= \sqrt{(4)(1.38\times 10^{-23})(77)(32)}\left(\frac{50}{82}\right) \\ &= 0.22\,\text{nV Hz}^{-1/2} \end{aligned} \tag{3.4.9}$$

That due to R_{in}^+ is

$$\begin{aligned} e_2 &= e_{n_{R_{in}^+}}\left(\frac{R_d}{R_{in}^+ + R_d}\right) \\ &= \sqrt{4kTR_{in}^+}\left(\frac{32}{50+32}\right) \\ &= \sqrt{(4)(1.38\times 10^{-23})(293)(50)}\left(\frac{32}{82}\right) \\ &= 0.35\,\text{nV Hz}^{-1/2} \end{aligned} \tag{3.4.10}$$

That due to R_{in}^- is

$$\begin{aligned} e_3 &= e_{n_{R_{in}^-}}\left(\frac{R_f}{R_{in}^- + R_f}\right) \\ &= \sqrt{4kTR_{in}^-}\left(\frac{100\times10^3}{10+100\times10^3}\right) \\ &= \sqrt{(4)(1.38\times10^{-23})(293)(10)}\,(1) \\ &= 0.4\,\mathrm{nV\,Hz^{-1/2}} \end{aligned} \tag{3.4.11}$$

The last thermal noise contribution is that due to R_f,

$$\begin{aligned} e_4 &= e_{n_{R_f}}\left(\frac{R_{in}^-}{R_{in}^- + R_f}\right) \\ &= \sqrt{4kTR_f}\left(\frac{50}{50+100\times10^3}\right) \\ &= \sqrt{(4)(1.38\times10^{-23})(293)(100\times10^3)}(0.5\times10^{-3}) \\ &= 0.02\,\mathrm{nV\,Hz^{-1/2}} \end{aligned} \tag{3.4.12}$$

The voltage noise density generated by the op-amp input current noise of $1\,\mathrm{pA\,Hz^{-1/2}}$ (200 Hz) at the + terminal of the op-amp is

$$\begin{aligned} e_5 &= i_n^+\left(\frac{R_d\,R_{in}^+}{R_{in}^+ + R_d}\right) \\ &= (1\times10^{-12})\left(\frac{(32)(50)}{32+50}\right) \\ &= 0.02\,\mathrm{nV\,Hz^{-1/2}} \end{aligned} \tag{3.4.13}$$

and that at the - terminal of the op-amp is

$$\begin{aligned} e_6 &= i_n^-\left(\frac{R_d\,R_{in}^+}{R_{in}^+ + R_d}\right) \\ &= (1\times10^{-12})\left(\frac{(50)(100\times10^3)}{50+100\times10^3}\right) \\ &= 0.05\,\mathrm{nV\,Hz^{-1/2}} \end{aligned} \tag{3.4.14}$$

Finally, the voltage noise density of the op-amp itself at 200 Hz is

$$e_7 = e_{n_{op-amp}} = 1\,\mathrm{nV\,Hz^{-1/2}} \tag{3.4.15}$$

The total voltage noise density referred to the input of the op-amp is then

$$\begin{aligned} e_T &= \sqrt{e_1^2 + e_2^2 + e_3^2 + e_4^2 + e_5^2 + e_6^2 + e_7^2} \\ &= 1.15\,\mathrm{nV\,Hz^{-1/2}} \end{aligned} \tag{3.4.16}$$

By using low resistance values at the input stage of the preamplifier, the dominant source of noise is seen to be that due to the op-amp, e_7, and indicates the fundamental noise limit to which future preamplifier designs using the same MCT detector element may strive. Assuming that any future design of the detector bias current generator will contain at least one transistor in the bias current path, the voltage noise density developed across the detector element due to shot noise will be, at a minimum,

$$\begin{aligned} e_{n_{shot}} &= \sqrt{2qI_d}\,R_d = \sqrt{(2)(1.6\times10^{-19})(0.014)}\,(32) \\ &= 2.1\,\mathrm{nV\,Hz^{-1/2}} \end{aligned} \tag{3.4.17}$$

where q is the electron charge. The current noise of the bias circuit is thus seen to be the dominant noise component of the preamplifier.

Considering the specific detectivity of the MCT detector element, $D^* = 2.88 \times 10^9\,\mathrm{cm\sqrt{Hz}\,W^{-1}}$, and responsivity, $R = 45\,\mathrm{V\,W^{-1}}$, as reported by the manufacturer, the detector noise may be calculated theoretically using the detector area, $A_d = 1\,\mathrm{mm^2}$:

$$e_{n_{\mathrm{detector}}} = \frac{R\sqrt{A_d}}{D^*} = \frac{(45)\sqrt{0.01}}{2.88\times10^9} = 1.6\,\mathrm{nV\,Hz^{-1/2}} \tag{3.4.18}$$

This noise voltage density is just slightly greater than the minimum possible instrumentation noise density calculated in equation 3.4.16 and indicates that, with a sufficiently low noise bias current generator, detector-limited performance is obtainable using the LT1028.

At a system level, noise associated with power supplies, wiring and environmental factors must also be considered. Given the relatively high current drawn by the preamplifier, operation with batteries would have been impractical since they would require frequent recharging. Mains-derived power supplies, on the other hand, offer convenient operation but may not give the required noise performance. The preamplifier was therefore tested for noise using both batteries and transformer-based supplies powered from the mains ($120\,VAC$) both with and without additional 60 Hz filtering in an attempt to equal the noise performance available from batteries.

The noise measurements were obtained using a FFT spectrum analyzer (Stanford Research Systems, model SR760, FFT spectrum analyzer) with the detector viewing an ambient temperature source. The results of the spectrum analyzer noise comparison are shown in Figure 3.11; the preamplifier gain of 2000 has been accounted for and the noise density is referred to the input of the op-amp.

As seen in Figure 3.11, noise spikes at harmonics of 60 Hz were present with both batteries and the mains derived power supplies, but to a larger degree in the latter case. Since the optical signals were modulated at 200 Hz, it was important to have a low noise voltage at this frequency. The use of a lock-in amplifier ensures that noise spikes at other frequencies would not adversely affect the performance of the instrument. It can also be seen that the noise performance at the modulation frequency of 200 Hz was $\sim 8\,\mathrm{nV\,Hz^{-1/2}}$ for both the filtered 120 VAC-derived and battery supplies. The filtered $120VAC$-derived power supply, detailed in Section 3.5.3, was therefore chosen for use in the final design.

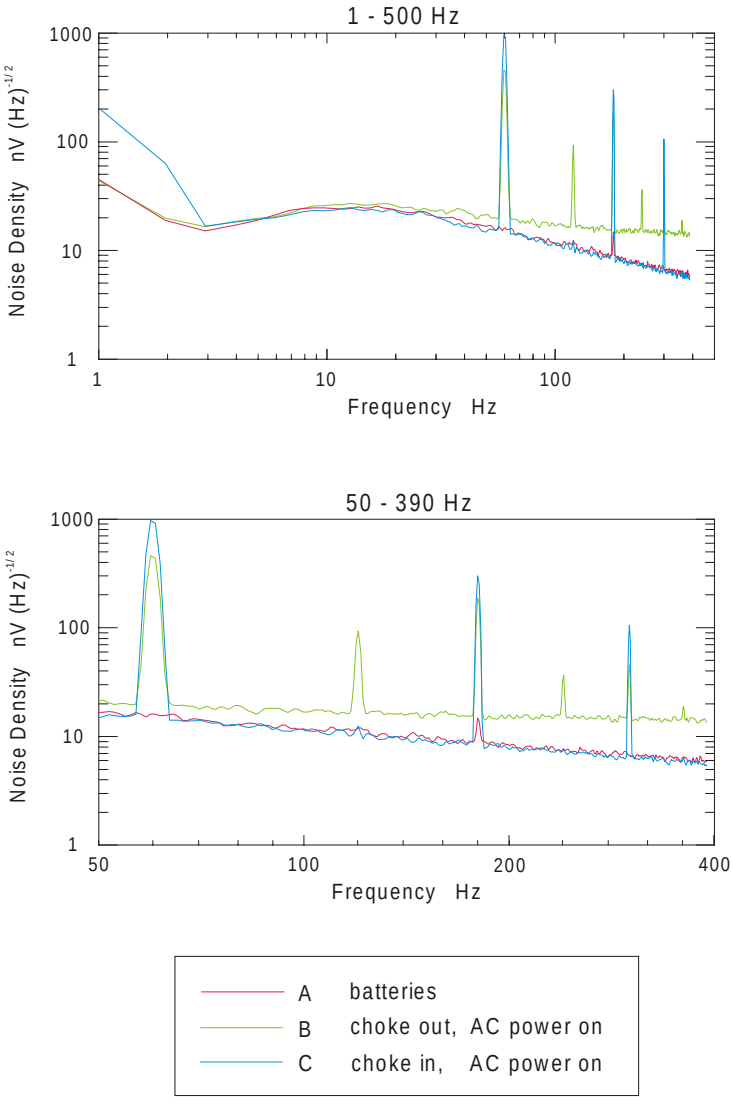

Figure 3.11: The noise performance of the preamplifier using batteries (red), and 120VAC-derived power including (blue) and excluding (green) a 60 Hz electrical filter.

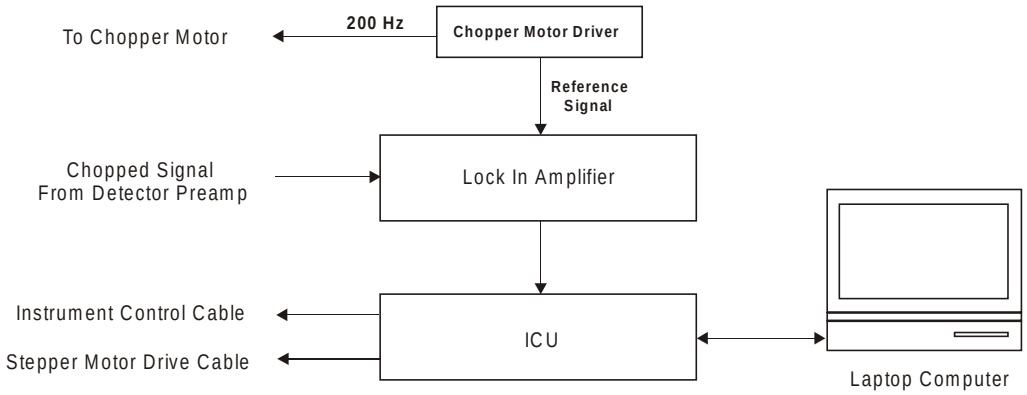

Figure 3.12: A schematic of the electronic components of the radiometer.

3.5 Electronic Instrumentation

Aside from the detector preamplifier, which was part of the detector dewar, the remainder of the electronic instrumentation consisted of the components shown in Figure 3.12. The instrument control unit, ICU, contained all the power supplies used by the system and managed the interface between the laptop computer, the instrument platform and the lock-in amplifier. The chopper motor controller unit operated independently of the ICU and provided a reference signal for the lock-in amplifier. Each of the components in the figure will be discussed in detail in the following sections.

3.5.1 Chopper Motor Driver

The chopper motor driver unit was a Stanford Research Systems SR 540 closed loop controller operated at a fixed modulating frequency of 200 Hz .

3.5.2 Lock-In Amplifier

The lock-in amplifier was a model EG&G 5208 single channel LIA with a ratiometric output from -10 to $+10$ VDC. The lock-in amplifier time constant, τ, and sensitivity were set to 10 ms and 100 mV, respectively, for all data acquired for this thesis. The external reference frequency was provided by the chopper driver unit.

3.5.3 The Interface Control Unit (ICU)

The ICU was comprised of three subunits; the computer interface board, the power supplies, and a commercial stepper motor drive for the scanning mirror mechanism. The laptop computer issued control commands to the ICU via 8 lines of the parallel port and were subsequently processed by the ICU into various aspects of instrument control. The analog signal from the detector/lock-in amplifier was digitized within the ICU and transmitted back to the computer over three additional lines of the parallel port configured as a serial interface. As seen in Figure 3.12, two cables connected the ICU to the instrument platform; a stepper motor drive cable and an instrument control cable (which also contained the power supply for the preamplifier). The two cables were used to minimize noise pickup on the detector power supply from the high current stepper motor drive signals. The signal from the detector was then sent to the lock-in amplifier over a coaxial cable. Figure 3.13 shows an interior detail photograph of the ICU. The power supplies are visible in the left partition, the computer interface board in the center partition, and the stepper motor drive unit in the right partition.

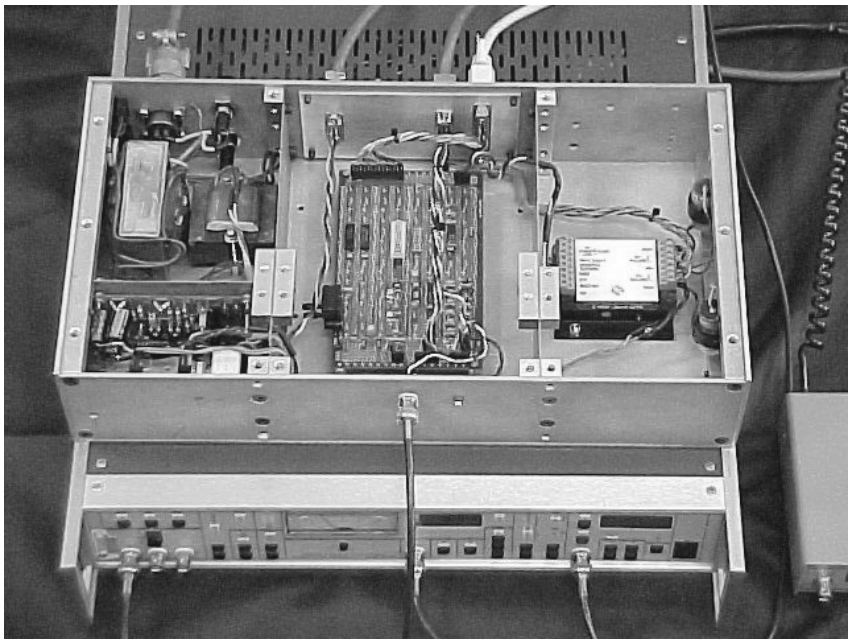

Figure 3.13: An interior view of the ICU showing the construction as comprised of three electromagnetically isolated sections.

Power Supply

Power supplies were required for three subsystems of the instrument; the detector preamplifier, the stepper motor driver and the computer interface board. The supplies were housed within the ICU and were constructed using generic LM 317/337 adjustable voltage regulator circuits deriving power from a standard 120 VAC outlet. A schematic diagram of the power supplies is given in Figure 3.14.

The power supplies were constructed as two separate circuits, each with its own transformer, in order to separate the higher current supply required for the stepper motor driver from the low noise supply required for the detector preamplifier. The preamplifier power supply was ± 12 VDC and constituted the first power circuit. The stepper motor

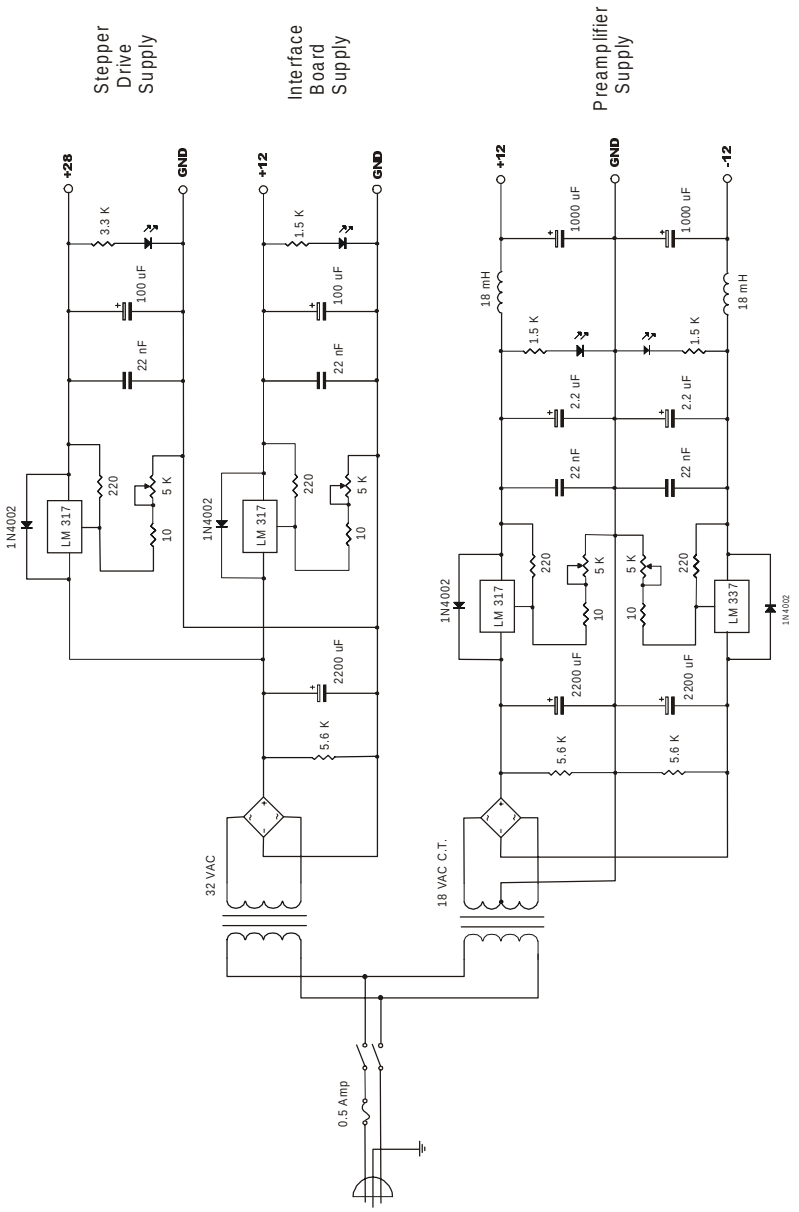

Figure 3.14: The radiometer power supplies. The preamplifier supply was isolated from the higher current stepper motor and interface board supplies for better noise performance.

driver unit required a minimum +28 VDC whereas the computer interface board required +5 VDC; the power for both of these subunits was derived from a common supply and constituted the second power circuit. The transformer for the stepper motor drive/computer interface board was selected to give a +32 VDC filtered output to meet the needs of the stepper driver. The +5 VDC required for the interface board was also derived from the +32 VDC by first regulating to +12 VDC using an *LM* 317 regulator located in the power supply partition of the ICU, and subsequently to +5 VDC, using an *LM* 7805 device located on the computer interface board itself. This two stage reduction was implemented so as to prevent possible overheating that might have been incurred in a single device, keeping in mind the reduced atmospheric pressure on the summit of Mauna Kea. The +28 VDC supply for the stepper motor driver unit was derived using another *LM* 317 located in the power supply partition of the ICU.

The noise performance of the preamplifier power supply was sufficient to give the $\sim 8\,\mathrm{nV\,Hz^{-1/2}}$ discussed in Section 3.4.8. The resolution of the 12-bit A/D converter on the computer interface board, and thus the tolerable noise on the output of the *LM* 7805, was half an LSB or 0.5 mV. In order to verify the noise performance of this supply, the output from the A/D converter was monitored while a constant DC input voltage was applied to an input channel. A constant digitization of the output was observed in the laboratory with an occasional dithering of the least significant bit, indicating a noise level of ˜1 $\mathrm{mV\,Hz^{-1/2}}$.

As previously discussed, batteries were considered for the preamplifier supply but equal noise performance was obtained by filtering the output from the ±12 VDC mains derived supply using large value inductors and capacitors configured as a low pass filter as

seen in Figure 3.14. Using the values of the inductor (18 mH) and the capacitor (1000 μF), the break frequency of the low pass filter occurred at

$$f_{-3dB} = \frac{1}{2\pi\sqrt{LC}} = \frac{1}{2\pi\sqrt{(18\times10^{-3})(1000\times10^{-6})}} = 37.5\,\text{Hz} \qquad 3.4.19$$

and was sufficient to reduce the noise to a level of $\sim 8\,\text{nV}\,\text{Hz}^{-1/2}$ at the optical modulation frequency of 200 Hz.

Interface Board

The interface board contained both digital and analog electronic functions and was constructed on a high quality *Schroff*^{TM} gold plated wire wrap board. The board included two separate ground planes which were used for analog and digital grounds. A parallel port interface with the control computer was chosen based on past experience with this approach, the availability of a previously developed parallel port C++ communications library, and the portability provided by this approach in the sense that this form of communication can be used with virtually any computer. The interface board circuitry was divided into an analog section that performed data acquisition and a digital section that translated the parallel port signals into various control functions. A schematic of the interface board is shown in Figure 3.15.

The analog input section of the interface board consisted of an A/D converter, a reference voltage generator and an eight channel CMOS analog multiplexer used to expand one of the A/D input channels by a factor of eight. The A/D converter was an *LTC* 1293*A*

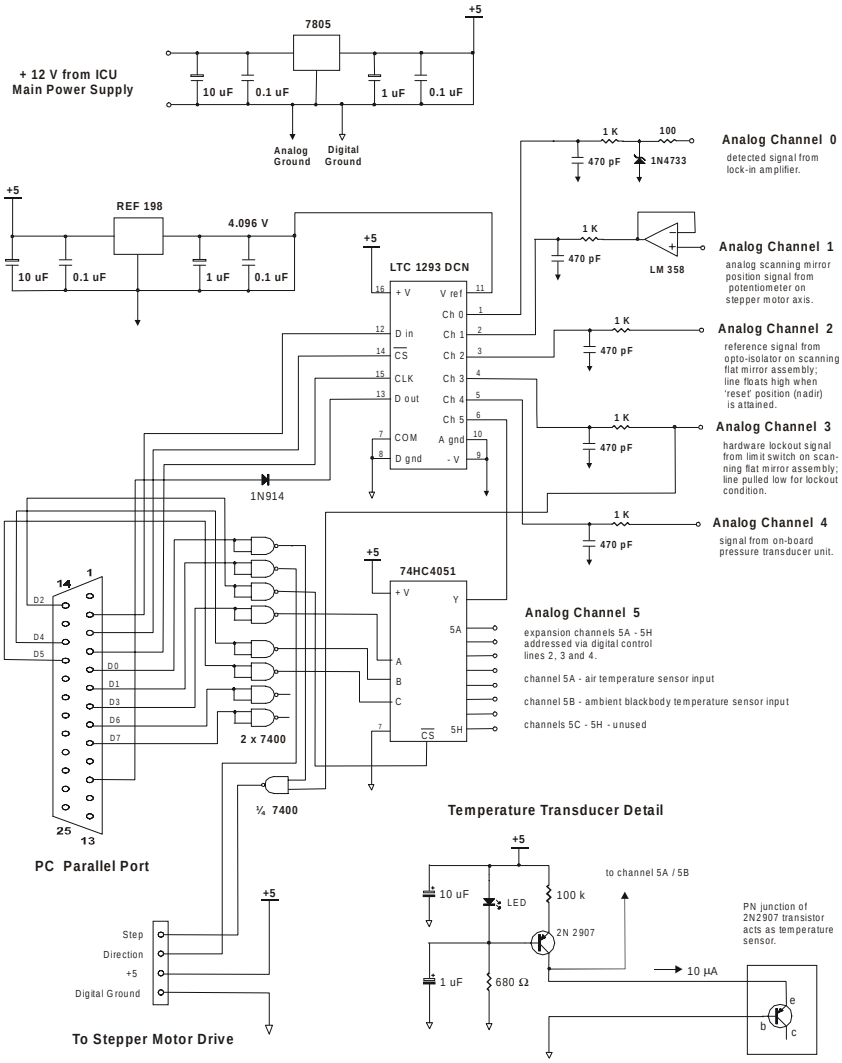

Figure 3.15: A schematic of the interface board circuitry.

which provided six selectable channels of 12 bit resolution. A 4.096 V reference voltage was supplied by an Analog Devices *REF* 198 resulting in a $4.096\,V\,/\,2^{12} = \pm 1\,\mathrm{mV}$ resolution.

The previously developed C++ parallel port communications library enabled the control program to acquire analog data by invoking the single library function **ADCRead-Chan(x),** where **x** is the channel number 0 through 5. The CD 4051 CMOS analog multiplexer was attached to channel 5 of the A/D and expanded the analog input capability to 13 channels. These additional channels were labeled as 5a through 5h. Access to the expanded channels was achieved by specifying a three bit address using the digital output command, discussed below, and then performing the acquisition from analog channel 5 with the above library command. Six of the analog input channels were used for status information from the instrument platform and one for acquisition of the detector signal via the lock-in amplifier. The remaining six channels were unused but available for future development.

The seven analog input functions and their channel assignments are summarized in Table 3.3. **Channel 0** is the signal from the detector/lock-in amplifier. The remainder of the signals require some additional explanation and are described in turn.

Channel 1 - Potentiometer The scanning mirror was actuated by a stepping motor whose positioning is controlled and tracked by the control program. Stepper motors are susceptible to losing steps, however, and a backup means of measuring the rotational position of the scanning mirror was implemented by attaching a 10-turn precision potentiometer to the stepper motor shaft as described in Section 3.4.3. The control program read the

Table 3.3: Summary of analog input functions.

Channel	Name	Description
0	Detector Signal	the detector signal from the lock in amplifier
1	Potentiometer	the output from the motor axis potentiometer
2	Reference	the signal from an opto switch sensing reference position
3	Out-of-Range	the signal from a limit switch sensing out of bounds
4	Pressure	the output of an on-board atmospheric pressure sensor
5a	Ambient Temperature	the signal from the ambient blackbody temperature sensor
5b	Air Temperature	the signal from the outside air temperature sensor
5c - 5h		Unused

potentiometer voltage through analog **channel 1**, calculated the mirror position in degrees (or airmass) and displayed the result as *actual position* on the user interface of the control computer. Also displayed was the *theoretical position*, as determined by the internal tracking of the motor step count. Discrepancies between the two alerted the user to a problem with motor tracking. In practice, the digital control of the stepper motor never failed to operate correctly and this dual mode position readout was of greatest value in the software development phase of the project.

Channel 2 - Reference Upon either system power-up or selection of the *initialization* function from the user interface, the control program drove the scanning mirror toward the nadir. The optical switch mounted on the pulley wheel signaled when the mirror had reached nadir. The control program alternately issued a step command followed by a read of analog **channel 2** until this line went high. The signal from the interrupter was a ramp function from low ($\sim 1.8\,V$) to high ($\sim 3.9\,V$) as the interrupting blade entered the switch and turned off the pull-down phototransistor. The transition voltage level is a variable set by the software and this gave flexibility in the fine adjustment of the nadir reference position.

Channel 3 - Out-of-Range The control software monitored the signal from the out-of-range limit switch during all subroutines involving step commands issued to the stepper motor driver and disabled the motor actuation program in the event of an internal tracking error. The range of operational motion of the scanning mirror was 90^o (providing 180^o of beam steering in the sky) but 2.5 degrees of tolerance was allowed on either side of this. The switches were wired such that the input to **channel 3** was pulled down to ground from +5 V by the closing of the limit switch.

Channel 4 - Pressure A $Sen-Sym$ model ASCX-15AN absolute atmospheric pressure sensor with integral output signal conditioning was included on the interface board and occupied analog **channel 4**. The output from the sensor was linear and two calibration points were established using the output voltages corresponding to the pressure readings from a mercury manometer in Lethbridge and from the JCMT atmospheric pressure sensor on Mauna Kea.

Channel 5 - Ambient/Air Temperature Metal case $2N2907$ pnp transistors controlled by independent driver circuits on the interface board were to have been used as temperature transducers for the ambient blackbody. However, the transistors comprising the constant current source circuit were found to be *extremely* sensitive to their case temperature and produced anomalous temperature data.

The control program used eight lines of the control computer parallel port to provide digital control signals to the ICU. The control program was able to set or reset the lines using the library function **SetDIO(x,y)** where **x** is the digital channel number (0

through 7) and **y** is the logical value (0 or 1). Two digital control outputs were required for control of the scanning mirror stepper motor (*step pulse* and *direction*) and four digital outputs were required for addressing the expanded set of analog input channels via the CMOS multiplexer.

As seen in the interface board schematic diagram, the scanning mirror motor controller *direction* bit is assigned to digital output **channel 1** and is wired directly to this input. A logical 1 on this line caused the scanning mirror to be driven downward. The *step* bit is assigned to digital **channel 0** and is first ANDed with the output from the Out-of-Range data line in order to disable the control program from actuating the motor at the hardware level. Four additional lines are required to address the extra analog input channels provided by the analog multiplexer. A logical 0 on digital **channel 2** provides the chip select input to the multiplexer and must be sent prior to a read from analog channel 5. Digital channels **3**, **4** and **5** provide the addressing for analog channels **5a** through **5h** with digital channel **3** being the least significant bit.

The parallel port lines are buffered by NAND gates on the interface board in order to protect the computer parallel port circuitry. These lines are not latched on the interface board since they are internally latched inside the computer. The schematic diagram shows the wiring and labelling of the digital lines in detail. It is important to note that the buffering inverts the digital level on the interface board from that issued by the library command above. With regard to the digital output library function **SetDIO(x,y)**, a y=0 becomes a set operation (high) and y=1 becomes a reset operation (low) on the interface board. The BIOS settings of the computer must be set to *bidirectional* for the parallel port

interface to work correctly.

The levels defined for the assertion of the **Out-of-Range** and **Reference** signals were deliberately arranged so that a computer would be able to run the control software when nothing was connected to the parallel port. During the development phase, it was particularly useful to be able to test the software without having the instrument connected.

3.5.4 Motor Driver

A *SlowSyn* model 230 -T commercial stepper motor controller with optional *reduced current* and *half stepping* modes was used to drive a 200 step/revolution stepper motor. The motor was a 6 lead type but by connecting the coils in series as shown in Figure 3.16 the motor was operated in the 4 lead mode and hence required less current and dissipated less heat. The controller required a *step* pulse and *direction* signal as inputs which were derived from the interface board as described in the last section and was run in the *reduced current* mode since the unit dissipated less heat and yet provided sufficient torque to hold the scanning mirror in position in this mode. The current in either of the coil windings under these circumstances was measured to be 480 mA. If the scanning mirror needed to be moved by hand, the power to the controller was simply turned off by means of an in-line switch.

The controller was also run in the half stepping mode by means of the *full/half* input select line as seen in the figure so as to provide the highest resolution possible. In this mode 400 step pulses produced a full rotation of the motor. When account is taken of the

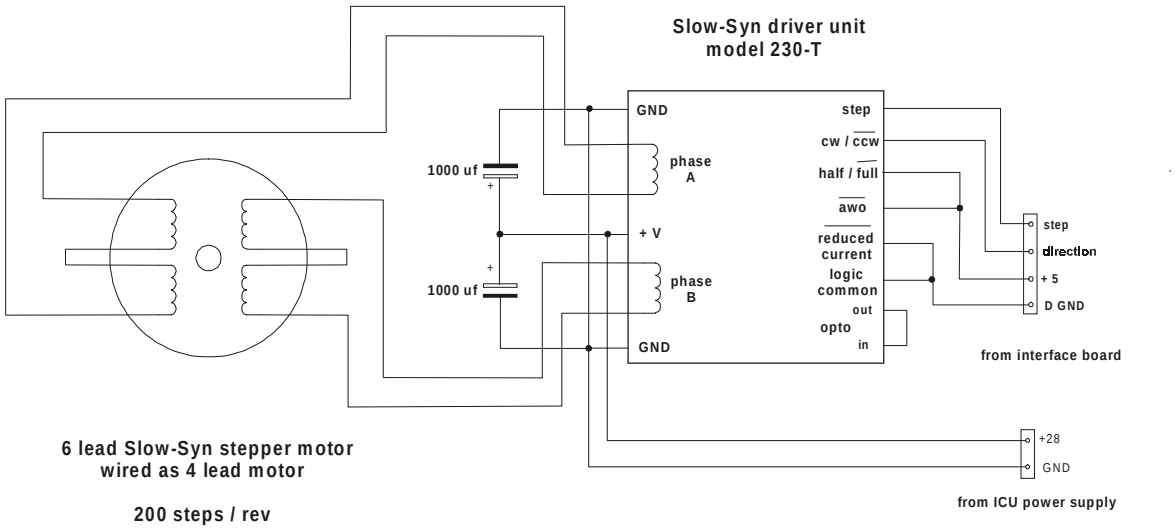

Figure 3.16: A schematic of the stepper motor driver unit.

10 : 1 pulley reduction described in Section 3.4.2 and the 2 : 1 ratio between scanning mirror rotation and angular displacement of the instrument field of view, the angular resolution provided by the scanning mirror assembly was then

$$\begin{aligned} resolution &= (\tfrac{1\ motor\ rev}{400\ steps})(\tfrac{360\ motor^o}{1\ motor\ rev})(\tfrac{2\ sky^o}{1\ mirror^o})(\tfrac{1\ mirror^o}{10\ motor^o}) \\ &= 0.18\ \tfrac{sky^o}{step} \end{aligned} \tag{3.4.20}$$

As discussed in Section 3.1, the field of view of the optical system was $\sim 0.5^o$ which, if taken as Gaussian, is seen to be spanned by 3 samples.

3.6 Control Program Software

The instrument control program was written using C++ and run under DOS since this language and environment, respectively, produced fast execution and access to

low level computer resources such as the parallel port. Past experience and the availability of previously developed code also contributed to this selection. Borland C++ version 4.5 was used for control program development and a Borland specific DOS-based GUI library was used for rapid development of the GUI interface.

3.6.1 The User Interface and Program Operation

When the instrument was powered up, the control program began operation by attempting to establish communication with the *LTC* 1293 A/D chip. If communication was not established, the program offered the option to continue, which, if selected, resulted in normal program operation. This mode of program operation was indispensable during program development.

If communication was established, the program prompted the user for the name of a data file to which all instrument activity and data would be logged. The program then executed an *initialization* routine which set the radiometer to the nadir, displayed the user interface on the computer screen, and then awaited further user input. Figure 3.17 shows the user interface main screen.

The instrument was designed to acquire data in one of three observational modes; *stare*, *continuous scan*, and *skydip*. When not acquiring data, the program could be said to be in an *idle* mode. The *initialization* procedure, identical to that automatically performed at system power-up, forced the instrument to disregard any current settings and drove the scanning mirror to the nadir until the *reference* signal was acquired as previously described.

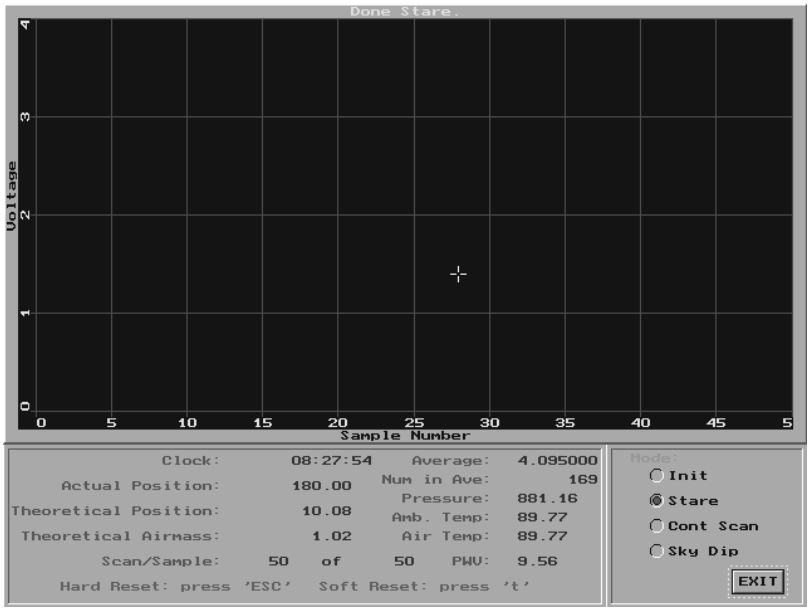

Figure 3.17: The Main screen of the control program.

The instrument then reset the internal position counter to zero and resumed the *idle* mode. This *initialization* procedure could be invoked at any time in *idle* mode.

All of the observational modes were accessed by means of the appropriate radio button, seen on the lower right of the user interface in the figure; this resulted in the appearance of a pop-up menu into which specific observational parameters were entered. Two other important instrument control functions, invoked from the keyboard and represented on the user interface only by a notice on the bottom, were *hard reset* and *soft reset*. The *hard reset* functioned as an emergency stop feature and terminated operation of the control program immediately. It could be invoked at any time and returned the user to DOS. The *soft reset* terminated data acquisition activity after the currently executing cycle and returned the user to the currently running data acquisition mode. This later function

was useful for backing out of an observation with incorrectly specified parameters (wrong integration time, for example) without shutting down the session.

During the operation of any of the modes a data record was written to a disk file and contained all acquired data, a time stamp and a log of all instrument activity (mode changes, parameter settings etc.). The acquired data differed in format depending on observational mode and consisted primarily of the radiometer signal as a function of time or zenith angle, but included the pressure transducer voltage, temperature sensor data, and all instrument control signals. During operation of any of the data acquisition modes, the radiometer signal was displayed in real time on the user interface, in both graphical and digital form, in addition to being logged to disk. A right click on the mouse when the cursor was in the graphical display area caused the cursor to transform into a crosshair and the coordinates of the screen to be displayed numerically. Several other data such as current time and the status of any currently running data acquisition modes can be seen on the lower part of the user interface in Figure 3.17. Details of the operation of each observational mode are now given in turn.

3.6.2 The *Stare* Mode

In the *stare* mode the instrument pointed to a user-specified zenith angle at which the radiometer signal was acquired as a function of time. Figure 3.18 shows the *stare* mode pop-up menu accessed via the appropriate radio button seen on the lower right of the figure. The user selected the zenith angle from which data was to be acquired and the integration

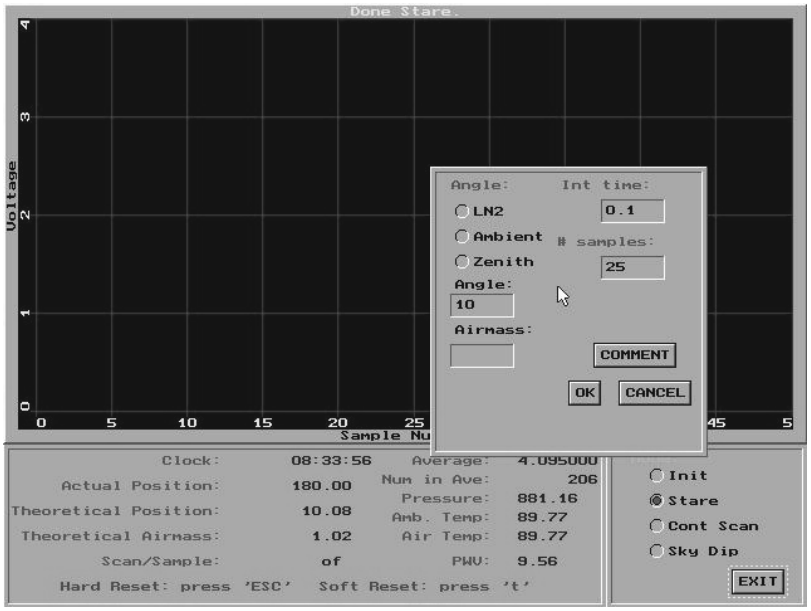

Figure 3.18: The *stare* mode menu.

time for each measurement. The zenith angle could be specified in terms of the angle, in degrees, from zenith or the equivalent airmass where airmass=1 / cos(zenith angle). Radio buttons were provided to specify predefined zenith angles corresponding to the frequently accessed positions of *zenith* (0 degrees), *ambient*, meaning the *ambient* blackbody reference (located at 128^o) and LN_2, meaning the LN_2 blackbody reference (located at 180^o).

3.6.3 The *Continuous Scan* Mode

In the *continuous scan* mode, the instrument was pointed to a user-specified starting zenith angle and then acquired the detector signal as a function of increasing zenith angle using the highest possible resolution (0.18^o/ step) until a lower user-specified zenith

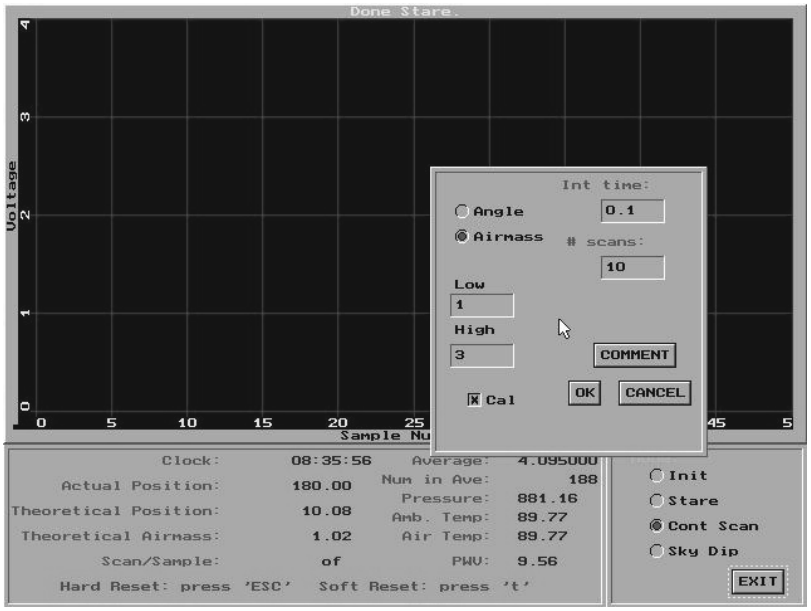

Figure 3.19: The *continuous scan* mode menu.

angle was reached. Once again, the angle could be specified in terms of the equivalent airmass, if desired. The user also specified the number of scans and the integration time. Figure 3.19 shows the *continuous scan* pop-up menu in which these observational parameters were entered. Observations using this mode consisted of *cycles* wherein a scan of the specified range of zenith angles was followed, if selected, by measurements from each of the reference blackbodies. This selection was done via the **Cal** (calibration) radio button, seen in the lower left of the pop-up menu.

3.6.4 The *Skydip* Mode

The *skydip* observational mode performed the same function as the *continuous scan* mode in that atmospheric emission could be observed over a user-specified range of zenith

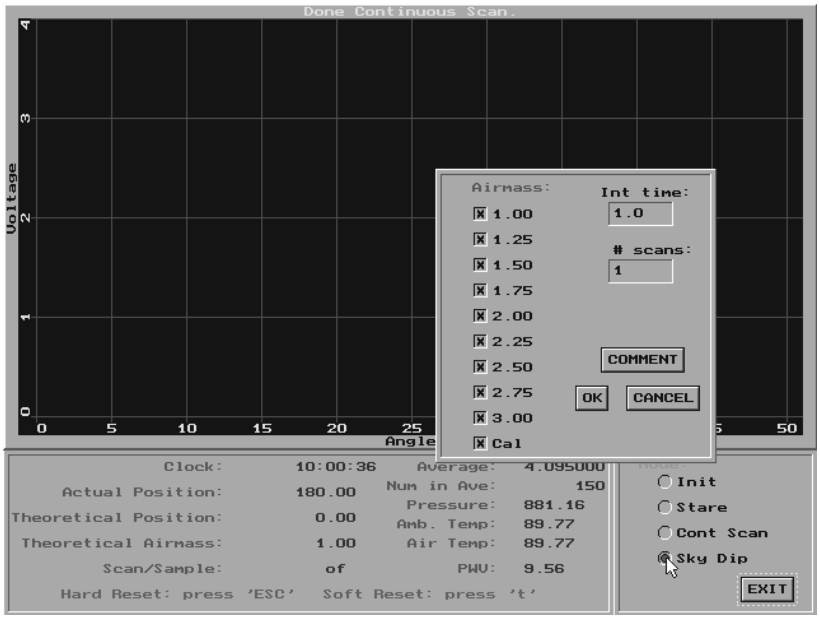

Figure 3.20: The *skydip* mode menu.

angles, but differed in that airmass increments in steps of 0.25 are selected or deselected via radio buttons in the *skydip* mode pop-up menu, as shown in Figure 3.20. While the *skydip* mode provides a faster measurement cycle than the *continuous scan* mode, the latter was used exclusively to provide all data at the highest possible angular resolution, the form most useful for radiometer calibration. The extra time involved in the acquisition of *continuous scan* datasets was not considered an important factor.

Chapter 4

Results

4.1 Overview

This chapter presents the results of the observations taken with the prototype radiometer at the James Clerk Maxwell Telescope (JCMT) on the summit of Mauna Kea, Hawaii. A description of the observing run conducted at the JCMT, including comments regarding observational conditions, is given in Section 4.2, and includes photographs showing the radiometer in operation. Section 4.3 briefly reviews the instrumentation which was discussed in detail in Chapter 3. Section 4.4 explains how the instrument was operated and describes the form of the data records produced during the observing run.

Data from the instrument was acquired in either the *stare* or a *continuous scan* mode (Section 3.6) of operation. The instrument could acquire *stare* data from arbitrary zenith angles using a wide range of sampling times but in practice data was obtained from only the zenith position at a sampling rate of 10 Hz. The *stare* mode of operation was

also used to acquire data simultaneously with the 183 GHz JCMT water vapor monitor, and these data provide a direct comparison with the alternate radio frequency approach to water vapor measurement. Section 4.5 presents the results from the *stare* mode of operation.

The *continuous scan* mode of operation acquired data over a continuous range of zenith angles from 0 to 70.38^o ($1-3$ airmasses) which were used to construct a *curve-of-growth*. Data records from this mode of operation also contained measurements from the blackbody references which enabled the instrument to be calibrated in terms of radiance. These results, including a theoretical analysis of the calibration process, are described in Section 4.6. Section 4.7 describes the characterization of the field of view of the instrument as determined by taking *continuous scan* measurements across the moon. Section 4.8 presents the analysis of *continuous scan* datasets containing atmospheric (water vapor) emission measurements and a discussion of the theory behind the analysis. This section culminates in the determination of the column abundance resolution of the instrument, Δw, in micrometers of precipitable water vapor ($\mu \mathrm{m}\, pwv$). An additional result obtained using the *continuous scan* mode of operation was the observation of the time evolution of a cloud bank passing over the summit of Mauna Kea.

4.2 Observations

Data were collected during an observing run at the James Clerk Maxwell Telescope (JCMT) atop Mauna Kea from December 9 to 18, 1999. Rain and fog on the summit prevented operation of the instrument for the first four days. The data presented in this

Figure 4.1: A view of the prototype radiometer showing the instrument platform at the center of the skirt of the JCMT and the instrumentation located some distance away.

thesis were obtained over a five day period from December 13 to 17. During this time the local relative humidity, as measured by the JCMT relative humidity sensor, ranged from a maximum of 50 % on the 13th to a minimum of 14% on the 17th as the effects of the inclement weather gradually diminished. Typically, the observations were conducted from approximately 6 p.m. to 12 a.m., local Hawaiian time, and contemporaneously with a JCMT observing run conducted by other members of Dr. Naylor's group. The sky conditions were generally clear with some scattered high cirrus cloud usually present during the early evening. A significant cloud bank was observed near the horizon on the evening of December 15th.

Figure 4.1 shows a photograph of the prototype radiometer at the center of the

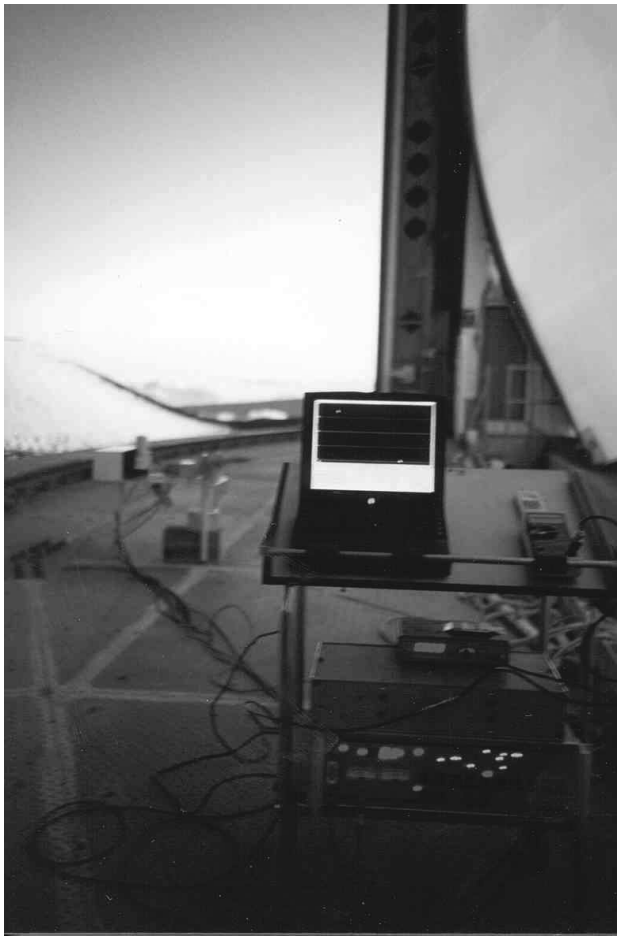

Figure 4.2: A view of the prototype at the beginning of a typical evening observing run.

apron of the JCMT with the electronic instrumentation located some distance away on a cart. Figure 4.2 shows the prototype in operation at the JCMT taken at the beginning of a typical evening of observation. Snow can be seen on a nearby cinder cone in the background, evidence of the recent inclement weather.

4.3 A Brief Review of the Instrumentation

The instrument consisted of an LN_2-cooled detector that alternately viewed the atmosphere, and ambient and LN_2 blackbody references by means of a stationary parabolic mirror and a scanning plane mirror. The optical input to the detector was chopped at 200 Hz by a reflective chopper blade, mounted immediately in front of the detector, so that the detector was alternately presented the throughput from the atmosphere (or the blackbodies) and a reflected view of its own cold environment. The modulated detector signal was amplified by a factor of 2000 by a low noise preamplifier (Section 3.4.7) and then synchronously detected by means of a lock-in amplifier with an additional gain of 100 and a ratiometric output from -10 to +10 V. The output from this amplifier was digitized by a 12-bit A/D converter and logged to a data file.

A C++ program, running under DOS on a laptop computer, was responsible for instrument control and data acquisition. Since the embedded temperature sensor gave anomalous readings (Section 3.4), the temperature of the ambient blackbody reference was taken to be equal to values recorded by the JCMT ambient temperature sensor and assigned to the data on a file-by-file basis, where the acquisition time of a typical data file was on the order of 20 minutes. The temperature of the cold blackbody at the reduced atmospheric pressure on the summit of Mauna Kea was taken as $73\,K$ for the duration of the observing run.

4.4 Instrument Operation and Description of Data Records

The instrument was operated in one of two observing modes, *stare* or *continuous scan* (Section 3.6). Upon power-up, the instrument created an observing session data file into which were recorded atmospheric pressure, observing parameters, session start and end times, and all the acquired data. Exiting the control program then closed the file and terminated the session. Any number of *stare* and/or *continuous scan* operations could be performed as a single session, but, in practice, observing sessions were restricted to only one type for simplicity.

In the *stare* mode, the scanning mirror pointed at a fixed zenith angle and measurements of atmospheric radiance were obtained as a function of time. The user specified the integration time and the number of measurements to be taken. The integration time used for *stare* mode measurements was set at 0.1 s for all data in this thesis. In contrast to the *continuous scan* mode of operation, calibration measurements from the blackbodies could not be selected automatically as part of a *stare* operation. Instead, measurements from the blackbodies were acquired in the same way as any other *stare* operation (i.e., by entering target angles of 128^o and 180^o corresponding to the locations of the ambient and LN_2 references, respectively).

In the *continuous scan* mode, the scanning mirror first pointed to the zenith (1 airmass) where the signal was integrated for the requested time. The zenith angle was then increased in 0.18^o increments and the process repeated until the upper limit of 70.38^o (3 airmasses) was reached. The scanning mirror then pointed to the ambient blackbody

and subsequently to the LN_2 blackbody for calibration measurements. The above sequence is termed a *cycle*. The instrument was able to scan between any two requested angles within the range of 0^o and 70.38^o but in practice only full range scans were obtained. The integration time for each measurement (as well as calibration measurements from the blackbody references) could be arbitrarily specified from a lower limit of 0.01 s but, as in the *stare* mode, integration times of 0.1 s were used exclusively. A full *continuous scan* cycle then consisted of 391 ($70.38^o \div 0.18^o$) measurements from the atmosphere followed by two reference measurements. One *continuous scan* session then produced one corresponding data file composed of one or more *continuous scan* operations. A typical file contained between 10 to 20 cycles and thus 10 to 20 independent calibration measurement pairs.

The control program logged all acquired data to a file suitably labelled as being composed of *stare* or *continuous scan* operations. Table 4.1 shows an excerpt from the data file log showing the supplementary data associated with each file. The first column shows the day on which the file was created along with any brief comments. Data files are labeled as 1, 2, etc. as shown in the second column and each represents an observing session. The third column gives the start and end times for the session. The fourth and sixth columns specify the type of session, i.e. *continuous scan* or *stare*. In the case of a *continuous scan*, the fourth and fifth columns indicate how many *continuous scans* were performed and the range of angles used, respectively. In the case of a *stare* mode, the sixth and seventh column show the number of samples taken and the angle at which they were taken, respectively. Column eight shows the local atmospheric pressure, P, in millibars, as measured by the on-board pressure transducer. As mentioned in Section 3.4, the temperature of the ambient

Table 4.1: An excerpt from the data log showing supplementary data associated with each data file. The excerpt shown includes only full *continuous scan* types of datasets.

Date comments	data file	Start time End time	Continuous Scan	Range	Stare	angle	P mbar	T C	H %
Thurs, Dec16									
	40	7:40 pm	25	full	-	-	625.6	2.3	23.5
		8:10 pm					625.9	1.3	27.0
	41	8:15 pm	25	full	-	-	625.8	1.1	26.9
		8:37 pm					626.0	1.3	22.8
Fri, Dec17									
	55	8:51 pm	-	-	3000	9	624.9	0.8	18.7
		8:57 pm					624.9	0.8	18.7
	56	8:58 pm	-	-	6000	9	624.9	0.9	16.9
		9:12 pm					624.9	0.9	16.9

blackbody was set equal to that provided by the JCMT ambient temperature sensor located on the apron of the JCMT; this value of T_{amb} is recorded in column nine. Column ten shows the local relative humidity, H, as recorded from the JCMT humidity sensor.

4.5 Analysis of *Stare* Data

The primary value of the *stare* mode was to obtain high speed observations of the variation of water vapor emission as a function of time along an arbitrary line-of-sight. This mode of observation was also valuable in the gathering of atmospheric emission data contemporaneously with the JCMT 183 GHz water vapor monitor and allowed a comparison between the data obtained from the prototype radiometer with that from the radio frequency approach. *Stare* mode data from the prototype radiometer was in the form of signal voltage vs. time and, due to the relatively high sample rate (10 Hz), these data revealed the rapid variation of water vapor emission as a function of time.

4.5.1 Water Vapor Variation in the Atmosphere

In the early morning of Thursday, December 16, between the hours of 12:30 a.m. and 1:15 a.m., the *stare* mode was used to acquire data from the zenith under the conditions of an apparently clear and cloudless sky. The instrument was set to sample at a rate of 10 Hz for a period of approximately 40 minutes. Figure 4.3 shows the results of this observation. In order to keep the data files to a reasonable size, the complete *stare* observation was composed of three individual *stare* operations. A time of approximately 10 s separated the *stare* operations as one operation was ended, stored to disk and another initiated, and accounts for the two discontinuities in the data seen in the figure at 1150 s and 2300 s.

This dataset is significant as it revealed the passage of a section of atmosphere containing an increased amount of water vapor, even though the sky remained clear to the eye. The data is shown at several magnifications, and at the highest resolution, the individual data points are seen. The instrumental error, to be derived in Section 4.6.3 from the stability of the signals from the LN_2 blackbody reference, is included in the figure. Given the instrumental error, fine scale variation of the signal on the order of 0.1 s cannot be taken as real variations in water vapor abundance since these structures lie within the error bar. Due to optical spillover at the LN_2 flask, the stability of the readings from the LN_2 blackbody reference, given in Section 4.6.3, represents an over-estimate of the instrumental error, and in light of this, it is likely that the variation between individual samples seen in the lower graph of Figure 4.3 represent real variations in water vapor abundance. In any case, trends on the order of 1 s are clearly discernible from these data.

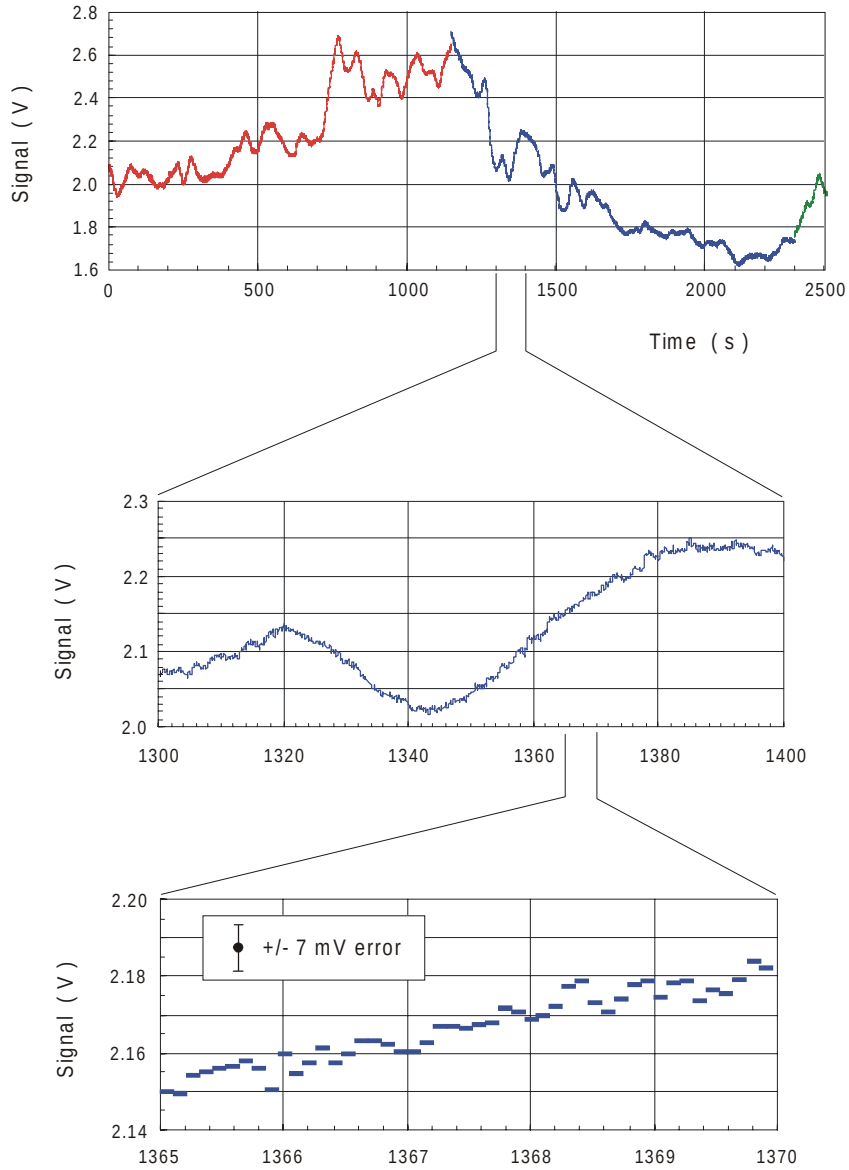

Figure 4.3: Stare data acquired from zenith under the conditions of an apparently clear and cloudless sky. Data were obtained using a sample rate of 10 Hz and are shown at multiple resolutions.

4.5.2 Comparison with the 183 GHz JCMT Water Vapor Monitor

On the evening of Friday, December 17, Professor Richard Hills of the University of Cambridge, UK, kindly allowed us to use his 183 GHz water vapor monitor simultaneously with our own. For a period of approximately one hour the prototype instrument acquired *stare* mode data from the same direction as the 183 GHz system which utilizes the JCMT antenna itself. The elevation of both instruments corresponded to a zenith angle of 9^o. Since the prototype radiometer was located on the apron of the JCMT, as shown in Figure 4.1, and the apron rotation is only adjusted periodically to follow the more precise azimuthal antenna rotation, the azimuth coordinates of the two data sets did not correspond exactly.

Upon examination, it was found that there was a high degree of correlation between the two datasets and that a simple shift in the horizontal axis allowed them to be brought into alignment. Figure 4.4 displays the simultaneous observations after the time shift. The lower curve is the 183 GHz data, sampled at a rate of 0.1 Hz. The upper curve is the raw *stare* data from the prototype, while the middle curve is the same data smoothed by a factor of 10 to an effective resolution of 1 s. The local time shown on the horizontal axis, and the precipitable water vapor scale of the vertical axis, in mm *pwv*, are taken from the 183 GHz data record. The data from the prototype was overlaid, displaced horizontally and rescaled vertically to give the best correlation. These data sets are shown displaced vertically by 0.1 units for clarity. Using the time stamp provided in the prototype data files, a delay of a few minutes was observed between the data sets due to the difference in azimuth between the two instruments.

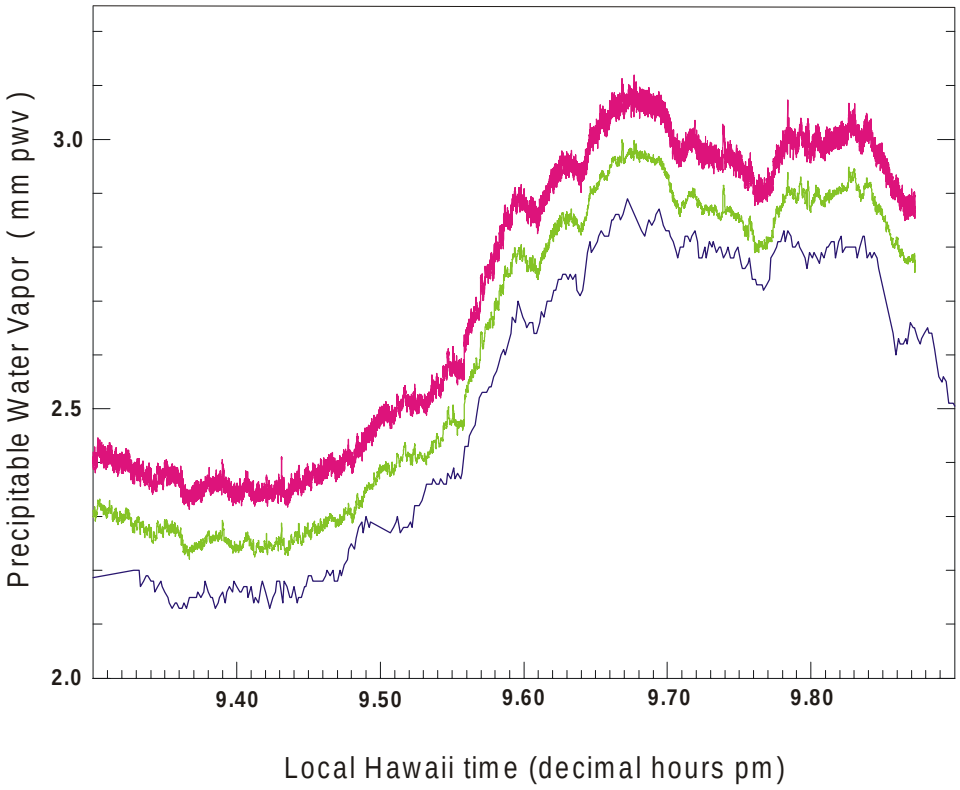

Figure 4.4: Datasets obtained simultaneously using the prototype radiometer and JCMT water vapor monitor show good agreement in water vapor abundance as a function of time. The bottom (blue) curve is the JCMT 183 GHz water vapor monitor data. The upper two curves are data from the prototype at 0.1 s (red) and 1 s (green) resolution. The vertical axis labeled in *pwv* refers to the 183 GHz data.

Although not shown in the figure, the vertical axis, labeled in mm *pwv*, has an alternate scale in signal voltage corresponding to the data from the prototype. Assuming that the highest and lowest signal values of the two data sets correspond to observations of the same atmospheric feature, the signal voltage of the prototype then corresponds to the precipitable water vapor as determined by the previously calibrated 183 GHz water vapor monitor at these times (9.40 and 9.67 LHT).

Prior to evaluation of the respective values of *pwv* and signal voltages at these

points using an IDL procedure (*Comparison_with_183GHz*), the two data sets were each smoothed by an additional factor; the prototype data was smoothed by a factor of 200 (to an equivalent 20 s integration interval) and the 183 GHz data was smoothed by a factor of 2 (also to an equivalent 20 s integration interval). These data points, which establish a conversion between signal voltage (or, after intensity calibration, radiance) and water vapor column abundance, w, proved superior to radiosonde calibration data and were therefore used as the primary means of calibrating the prototype. These calibration points are summarized in Table 4.2.

Table 4.2: The relation between prototype radiometer signal voltage and precipitable water vapor as determined by the JCMT water vapor monitor.

Signal from prototype (V_{rms})	Precipitable Water Vapor as determined by 183 GHz radiometer (mm pwv)
1.61	2.03
1.94	2.87

4.6 Calibration of Instrumental Responsivity

Detector responsivity, R_{det}, is usually defined as the detector output signal voltage per unit Watt of incident optical power with units of VW^{-1}. We defined an overall *instrumental* responsivity, R_{inst}, expressed in $\mathrm{V\,W^{-1}m^2\,sr}$, relating instrument output voltage to incident *radiance.* Measurements of the two blackbody references allowed this conversion factor between radiometer signal voltage and source radiance to be determined.

This aspect of instrument calibration corresponds to conversion between different

scales on the vertical axis of the *curve-of-growth* and is distinct from a second calibration procedure, discussed in Section 4.8, wherein a conversion factor is established between precipitable water vapor (horizontal axis of continuous scan datasets) and radiometer signal using the data from Table 4.2.

As previously described, calibration measurements were recorded only in *continuous scan* data files. Not all the *continuous scan* files contain useful calibration data, however, as some of the data were obtained before the settings of the electronic instrumentation had been finalized and, on occasion, the LN_2 reservoir ran low. Sixteen *continuous scan* files, containing calibration measurements taken after the instrumental configuration had been optimized, were selected for use in the determination of the instrumental responsivity. Specifically, these data files were numbers 20, 21, 22, 23, 24, 35, 40, 41, 43, 44, 45, 50, 51, 52, 60 and 62. An IDL routine (*Extract_Data*) was used to extract the blackbody calibration measurements from each *continuous scan* data file. Each file contained one ambient and one LN_2 blackbody measurement per *continuous scan* cycle with typically 15 cycles per file. The routine calculated a mean and a standard deviation of the signals from the ambient and cold blackbodies for each file.

4.6.1 Intensity Calibration Theory

The calibration procedure given below describes how the instrumental responsivity is determined from observations of the blackbody references. Due to the design of the radiometer, knowledge of the characteristics of the optical elements was not required for an accurate determination of R_{inst} since the optical train was the same when the instrument

viewed the atmosphere or the calibration sources; the efficiencies and emissivities of the optical elements were common to all measurements.

The infrared bandwidth of the prototype was determined by the spectral bandpass of the infrared filter. The integrated spectral radiance of the atmosphere, over the filter bandwidth, $\Delta\sigma = 462 - 505\,\mathrm{cm}^{-1}$, can be written

$$L_{\,atm} \;=\; \int_{462}^{505} \epsilon_{\sigma_{atm}} B_\sigma\left(T_{atm}\right)\, d\sigma \qquad 4.6.1$$

where T_{atm} is the temperature of the atmosphere, $\epsilon_{\sigma_{atm}}$ is the emissivity of the atmosphere and $B_\sigma(T)$ is the spectral radiance given by the Planck function, equation 2.3.31. Similar expressions hold for the radiance of the cold blackbody, L_{LN_2}, the ambient blackbody, L_{amb}, the scanning flat mirror, L_s, the parabolic mirror, L_p, the reflective chopper blade, L_c, the polypropylene window, L_w, and the optical filter, L_f, using their corresponding temperatures. The detector also sees the radiance of its own LN_2-cooled environment, L_e, when its field of view is interrupted by the reflective chopper blade.

For the narrow spectral band under consideration the various emissivities of the optical components are taken as constant but unknown quantities. The emissivities of the blackbodies are also taken as constants with values of $\epsilon_{ambient} = 1$ and $\epsilon_{LN2} = 1$. The spectral emissivity of the atmosphere, $\epsilon_{\sigma_{atm}}$, is a complicated function of wavenumber, representing the spectral emission of water vapor, and depends on the column abundance, and both the temperature and pressure profiles of the atmosphere.

The optical signal powers incident on the detector when the instrument is taking (chopped) measurements of the atmosphere, $\Phi_{\,sky}$, the ambient blackbody, $\Phi_{\,amb}$, and the

LN_2 blackbody, Φ_{LN_2}, are

$$\begin{aligned}\Phi_{atm} &= [\, t_f\, t_w\, r_p\, r_s\, L_{atm} + t_f\, t_w\, r_p\, L_s + t_f\, t_w\, L_p \\ &\quad + t_f\, L_w + L_f - (\, t_f^2\, t_w^2\, r_c\, L_e + t_f\, t_w\, L_c)\,]\, A\Omega \qquad 4.6.2\,a\end{aligned}$$

$$\begin{aligned}\Phi_{amb} &= [\, t_f\, t_w\, r_p\, r_s\, L_{amb} + t_f\, t_w\, r_p\, L_s + t_f\, t_w\, L_p \\ &\quad + t_f\, L_w + L_f - (\, t_f^2\, t_w^2\, r_c\, L_e + t_f\, t_w\, L_c)\,]\, A\Omega \qquad 4.6.2\,b\end{aligned}$$

$$\begin{aligned}\Phi_{LN_2} &= [t_f\, t_w\, r_p\, r_s\, L_{LN_2} + t_f\, t_w\, r_p\, L_s + t_f\, t_w\, L_p \\ &\quad + t_f\, L_w + L_f - (\, t_f^2\, t_w^2\, r_c\, L_e + t_f\, t_w\, L_c)\,]\, A\Omega \qquad 4.6.2\,c\end{aligned}$$

where t is the transmittance and r is the reflectance of the subscripted optical components; s refers to the scanning plane mirror, p refers to the parabolic mirror, c refers to the reflective chopper blade, w refers to the polypropylene window and f refers to the infrared filter. The various terms involving t and r, as with the emissivities of the optical components, are taken as constant but unknown functions of σ. The above equations can be written as

$$\Phi_{atm} = (\, \eta\, L_{atm} + L_{optics} - L_{reflected}\,)\, A\Omega \qquad 4.6.3\,a$$

$$\Phi_{amb} = (\, \eta\, L_{amb} + L_{optics} - L_{reflected}\,)\, A\Omega \qquad 4.6.3\,b$$

$$\Phi_{LN_2} = (\, \eta\, L_{LN_2} + L_{optics} - L_{reflected}\,)\, A\Omega \qquad 4.6.3\,c$$

where the efficiency of the optical train is

$$\eta = t_f\, t_w\, r_p\, r_s \qquad 4.6.4$$

and where the radiances associated with the optics and that associated with the chopper and detector environment are collected into the following terms:

$$L_{optics} \;=\; t_f\, t_w\, r_p\, L_s + t_f\, t_w\, L_p + t_f\, L_w + L_f \qquad 4.6.5$$

$$L_{reflected} \;=\; t_f^2\, t_w^2\, r_c\, L_e \;+\; t_f\, t_w\, L_c \qquad 4.6.6$$

Dividing equations 4.6.3 by $A\Omega$ turns the left hand sides into radiances and allows the subsequent calibration analysis to be carried out in terms of the radiance of the sources rather than their flux. Subtraction of equation $4.6.3\,c$ from $4.6.3\,b$ and division by $A\Omega$ then yields a chopped radiance ΔL_d at the detector of

$$\Delta L_d \;=\; \eta\,(\,L_{amb} - L_{LN_2}\,) \qquad 4.6.7$$

The rms voltage signals from the lock-in amplifier associated with a chopped observation of the ambient and LN_2 blackbodies are, respectively, V_{amb} and V_{LN_2}. The instrumental responsivity can be written as

$$R_{inst} \;=\; (\;\Delta V \;/\; \Delta L\;) \;=\; (V_{amb} - V_{LN2}) \;/\; (L_{amb} - L_{LN_2}) \qquad 4.6.8$$

with units of $\mathrm{V\,W^{-1}m^2sr}$ and where

$$\Delta L \;=\; \tfrac{\Delta L_d}{\eta} = (\,L_{amb} \;-\; L_{LN_2}\,) \qquad 4.6.9$$

R_{inst} was determined using values of V_{amb} and V_{LN_2} provided by the IDL routine ($Extract\_Data$) and the corresponding L_{amb} and L_{LN_2} obtained via the Planck function using the source temperatures T_{amb}, from the JCMT ambient temperature sensor, and T_{LN_2}.

Given the responsivity of the MCT detector element, R_d, provided by the manufacturer, a value for η, the overall optical efficiency of the prototype radiometer can be defined as

$$\eta = R_{inst} \,/\, R_d \qquad 4.6.10$$

An accurate knowledge of this efficiency could be used in future feasibility calculations (Section 3.2).

Using the instrumental responsivity, R_{inst}, atmospheric emission data collected by the instrument can be transformed into a graph whose vertical axis is given in terms of radiance rather than signal voltage. Figure 4.5 shows three *continuous scan* datasets. The upper graph shows the raw data with signal voltage plotted as a function of zenith angle. The lower graph shows the intensity calibrated data expressed in terms of radiance as a function of airmass (1/cos(zenith angle)). The signals from the ambient and LN_2 blackbody references which are included in *continuous scan* datasets can be seen immediately to the right of the curves.

It will be noticed from Figure 4.5 that the LN_2 reference signal voltage has a value of ~ 0.6 V. Considering the almost negligible radiance of the LN_2 source at a wavelength of 20 μm (Section 1.3.3), it was expected that this signal should have been nearly zero. Since care was taken to ensure that the lock-in amplifier was correctly phased during all observations, the only plausible explanation for this offset was an optical spillover occurring at the LN_2 blackbody. Prior to the observing run, a 150 mm diameter copper disk, coated with the same blackened epoxy surface used on the ambient blackbody (Section 3.4), was to have been immersed at the bottom of a LN_2 flask. Unfortunately, the only LN_2 flasks available at the JCMT were slightly undersized; this resulted in an optical spillover and accounts for the DC offset seen in the data. Further evidence supporting this explanation

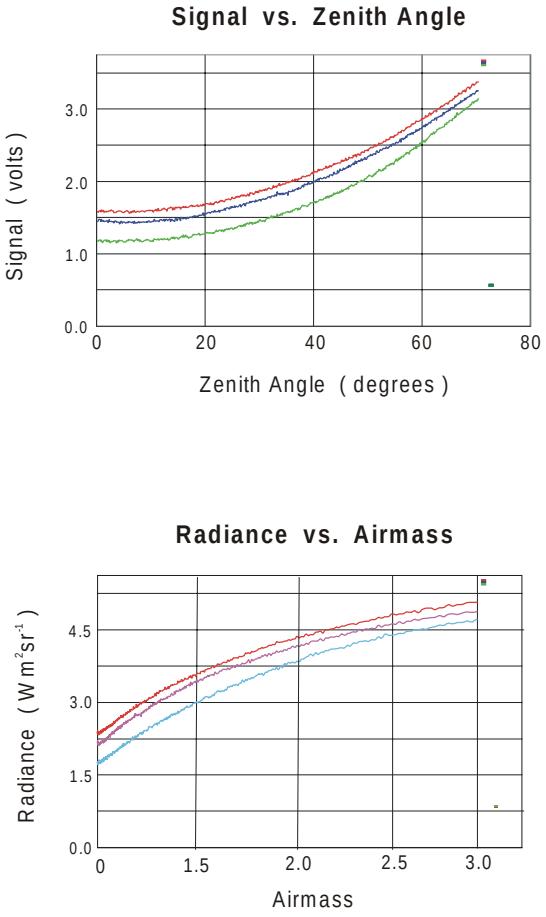

Figure 4.5: Three typical continuous scan datasets shown with the vertical axis in signal voltage (top) and, after conversion via the instrumental responsivity, radiance (bottom). The effect of transforming the horizontal axis from zenith angle to airmass is evident.

has been provided by recent results from an upgraded version of the radiometer which show zero signal voltage when the radiometer views the calibration source.

In the analysis of the data presented in this thesis, the constant offset voltage, resulting from the optical spillover, was subtracted from all datasets. The instrumental responsivity and the radiometer sensitivity derived in the subsequent analysis will therefore represent lower performance limits of the prototype radiometer.

4.6.2 Calculation of Instrumental Responsivity

Equation 4.6.8 was used to obtain the instrumental responsivity, R_{inst}, using the data from the ambient and LN_2 blackbodies, located in *continuous scan* data files. Since a single temperature (from the JCMT ambient temperature sensor) was assigned to the ambient blackbody for each data file (containing ~ 20 ambient blackbody readings per file), a responsivity was also calculated for each file; the signal voltages from the LN_2 and ambient blackbodies, used in equation 4.6.8 on a file-to-file basis, was an average of all LN_2/ambient blackbody readings within the file. The standard deviation of each of these values was also calculated. The result was an average responsivity, with associated error, for each file. Table 4.3. gives a summary of these calculations.

Table 4.3: Summary of average responsivity calculations.

Data File	T_{amb} (K)	L_{LN2} (W/m^{2}sr)	L_{amb} (W/m^{2}sr)	V_{LN2} (V)	V_{amb} (V)	R (V/W/m^{2}sr)	ΔR (V/W/m^{2}sr)	ΔR* (V/W/m^{2}sr)
20	276.0	4.3E-3	5.056	0.584	3.941	0.664	6.8E-3	1.5E-3
21	276.0	4.3E-3	5.056	0.577	3.916	0.661	7.0E-3	2.4E-3
22	276.2	4.3E-3	5.069	0.579	3.900	0.656	6.8E-3	2.0E-3
23	276.2	4.3E-3	5.069	0.585	3.891	0.653	6.6E-3	1.1E-3
24	275.3	4.3E-3	5.024	0.588	3.876	0.655	6.9E-3	2.3E-3
35	274.5	4.3E-3	4.981	0.574	3.883	0.665	6.9E-3	1.7E-3
40	275.3	4.3E-3	5.024	0.564	3.881	0.661	7.1E-3	2.5E-3
41	274.4	4.3E-3	4.976	0.560	3.866	0.665	6.8E-3	1.4E-3
43	274.1	4.3E-3	4.966	0.552	3.855	0.666	7.1E-3	2.4E-3
44	274.3	4.3E-3	4.971	0.561	3.828	0.658	6.9E-3	1.9E-3
45	273.8	4.3E-3	4.946	0.568	3.830	0.660	7.2E-3	2.8E-3
50	274.4	4.3E-3	4.976	0.587	3.899	0.666	7.0E-3	1.9E-3
51	274.2	4.3E-3	4.996	0.575	3.928	0.672	7.0E-3	2.0E-3
52	274.0	4.3E-3	4.956	0.573	3.911	0.674	7.2E-3	2.4E-3
60	274.1	4.3E-3	4.961	0.577	3.884	0.667	7.0E-3	1.9E-3
62	274.1	4.3E-3	4.961	0.589	3.856	0.659	7.0E-3	2.1E-3

From each of the 16 *continuous scan* data files listed in Section 4.6.1, and again in the first column of the Table 4.3, the IDL program (*Extract_Data*) provided the averaged

voltage readings from the LN_2 and ambient blackbodies, V_{LN_2} and V_{amb}, respectively; these are listed in the fifth and sixth columns of Table 4.3. This IDL routine also calculated standard deviations, ΔV_{LN_2} and ΔV_{amb}, for V_{LN_2} and V_{amb}, respectively (not included in table). The temperature of the LN_2 reference, T_{LN_2}, was assumed to be constant at 73 K. The temperature assigned to the ambient blackbody for each file, T_{amb}, is listed in the second column. Another IDL routine (*Planck_Power_462_505*) computed the integral of the Planck radiance (equation 2.3.31) over the spectral range $462 - 505\,\mathrm{cm}^{-1}$ for both the LN_2 and ambient blackbodies, i.e., L_{LN_2} and L_{amb}, using their respective temperatures, T_{LN_2} and T_{amb}. These radiances are listed in the third and fourth columns, respectively. The calculated file-by-file instrumental responsivity is given in the seventh column.

To estimate the error on R_{inst}, errors must be assigned to the voltages and radiances in the responsivity formula, equation 4.6.8. The IDL routine (*Extract_Data*) provided the standard deviations, ΔV_{amb} and ΔV_{LN_2}, for the error on V_{LN2} and V_{amb}, respectively. With regard to the error in ambient blackbody radiance, ΔL_{amb}, it was noted that the local temperature variations occurring over the duration of one data file were on the order of $\sim$ 1K, and thus an error of ± 1 K was assigned for ΔT_{amb}. This error in temperature was translated to an error in radiance, ΔL_{amb}, by computing the spectral integration of the Planck function using temperatures of $T_{amb} \pm 1$ K:

$$\Delta L_{amb} \;=\; \tfrac{1}{2}\,[\; L_{amb}(T_{amb} + 1\,\mathrm{K}) \;-\; L_{amb}(T_{amb} - 1\,\mathrm{K})\;] \qquad 4.6.11$$

The error in the radiance of the LN_2 blackbody, ΔL_{LN2}, was taken to be zero since the temperature of LN_2 on the summit is stable (atmospheric pressure variations during the observing run were ± 3 mb). Furthermore, as shown in Section 1.3.3, the radiance of a

73 K source is approximately three orders of magnitude smaller than an ambient (273 K) source, and thus does not contribute significantly to the propagated error.

Considering equation 4.6.8, and taking $\Delta L_{LN2} = 0$, the error in the responsivity is given by

$$\Delta R_{inst} = |R_{inst}| \sqrt{\left(\frac{\Delta L_{amb}}{L_{amb} - L_{LN2}}\right)^2 + \left(\frac{\sqrt{(\Delta V_{amb})^2 + (\Delta V_{LN2})^2}}{V_{amb} - V_{LN2}}\right)^2} \qquad 4.6.12$$

and was calculated for each data file; these values are listed in column eight of Table 4.3. Since the spectral region $462 - 505\,\mathrm{cm}^{-1}$ lies near the peak of the Planck function when evaluated at the temperature of the ambient blackbody (see Figure 1.3), the ± 1 K error assigned to ΔT_{amb} makes ΔL_{amb} the dominant error in the responsivity calculation.

The error associated with the uncertainties in the temperature, and hence radiance, of the ambient blackbody is one that can be easily reduced by more accurate thermometry. In order to give a better representation of the true performance of the prototype radiometer, the error in the instrumental responsivity was recalculated using equation 4.6.12 with $\Delta T_{amb} = \pm 0.1$ K; the results are listed in column nine of Table 4.3 as ΔR^*_{inst}.

The average of the averaged file-by-file responsivities (column 7 in Table 4.3) gave the final instrumental responsivity:

$$R_{inst} = 0.663 \quad \mathrm{V\,W^{-1}m^2sr} \qquad 4.6.13$$

The average of the errors in instrumental responsivity using $\Delta T_{amb} = \pm 1$ K (column 8 of Table 4.3) was

$$\Delta R_{inst} = 7 \times 10^{-3} \qquad \mathrm{V\,W^{-1}m^2sr} \qquad 4.6.14$$

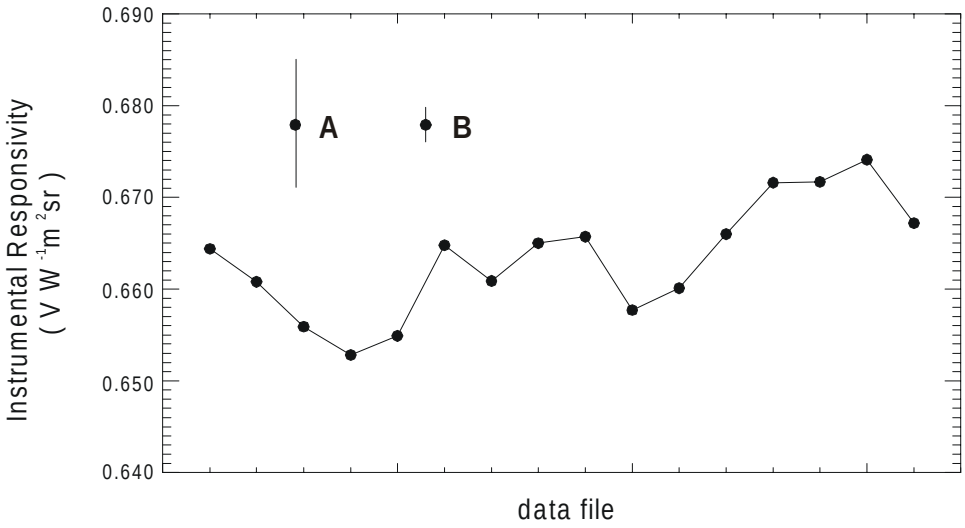

Figure 4.6: The instrumental responsivity as calculated for each data file. Also shown is the error in responsivity due to a +/- 1 K (A) and +/- 0.1 K error in ambient blackbody temperature.

whereas the average of the errors using $\Delta T_{amb} = \pm 0.1\,\mathrm{K}$ was

$$\Delta R^{*}_{inst} \;=\; 2 \times 10^{-3} \;\; \mathrm{V\,W^{-1}m^{2}sr} \qquad 4.6.15$$

Taking the worst case error, the final instrumental responsivity became

$$R_{inst} = \; 0.663 \;\; \pm 7 \times 10^{-3} \;\; \mathrm{V\,W^{-1}m^{2}sr} \qquad 4.6.16$$

Figure 4.6 shows a graphical summary of the instrumental responsivity calculations. Given sufficient readings from the blackbody references, the error in the responsivity, in principle, could be reduced to a point where it becomes negligible in comparison to the instrumental noise. In any case, the *pwv* resolution of the radiometer is derived solely from the instrumental noise, which, in turn, is derived from an analysis of the stability of the signals from the blackbody references.

4.6.3 Stability of the References

The instrumental noise was determined from an analysis of the file-to-file standard deviations of the signals from the blackbodies, ΔV_{amb} and ΔV_{LN_2}, introduced in the previous section; typically there were $15 - 20$ independent blackbody measurements in each standard deviation calculation. This noise, or voltage signal error, corresponds to an error in measured pwv, Δw, by projection of the instrumental noise onto the horizontal axis of the *curve-of-growth* as discussed in Section 2.4.2.

The temperature of the ambient blackbody followed changes in outside temperatures over the duration of each data file, and hence the scatter in each ΔV_{amb} was expected to be greater than that in the corresponding ΔV_{LN_2}, since the temperature of the LN_2 was constant. For the same reason, the file-to-file variability of ΔV_{amb} was also expected to be greater than that of ΔV_{LN_2} to an even larger degree, since the temperature changes over the course of an evening were greater than those over the acquisition time of a single file. It is then reasonable to take the average of ΔV_{LN_2}, without consideration of ΔV_{amb}, as representative of the noise performance of the radiometer.

As discussed in Section 4.6.1, the undersized LN_2 flask resulted in an optical spillover of the radiometer beam. The signals from the LN_2 blackbody would therefore be subject, at a low level, to variations in the ambient temperature. It is therefore also reasonable to assume that the minimum file-to-file standard deviation, ΔV_{LN_2}, rather than the average of all the file-to-file standard deviations, as the true instrumental noise. This minimum value simply represented the standard deviation of LN_2 blackbody signals taken

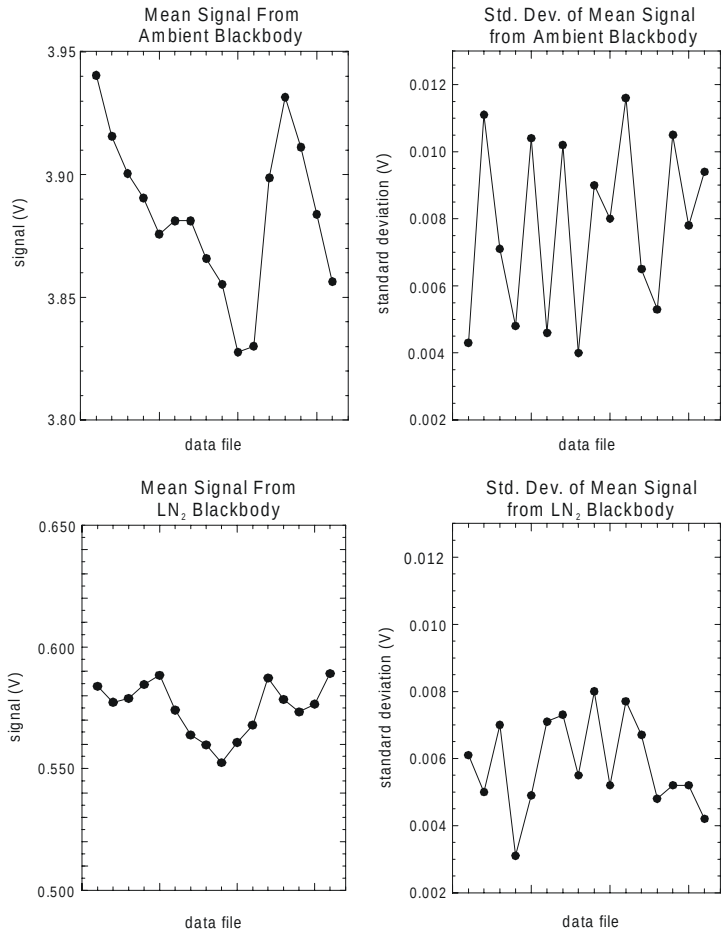

Figure 4.7: The stability of the signals from the blackbody references. The mean of the signals from the blackbody references are shown in the left hand graphs on a file-to-file basis. The corresponding standard deviations of these averages are shown in the right hand graphs.

over a period during which the temperature of the JCMT apron floor changed the least.

The results of the analysis of the signals from the blackbody references are shown in Figure 4.7. The greater file-to-file stability of the LN_2 reference, as compared with the ambient reference, is apparent in the left hand figures which are shown to the same scale. The expected lower scatter in the signals from the LN_2 reference as compared with the ambient reference, is also seen in the right hand figures which are plotted using the same

vertical range. The minimum standard deviation, $\Delta V_{LN_2} = 3.1\,\mathrm{mV}$, is seen with the fourth data file in the lower right hand graph corresponding to data file 23 (Section 4.6.1). The average of the standard deviations from this graph, on the other hand, was $\Delta V_{LN_2} = 5.8\,\mathrm{mV}$. Since the sample time used for all data collected in this thesis was 0.1 s, the noise in a 1 second integration became

$$V_{noise} = \frac{5.8 \times 10^{-3}}{\sqrt{10}} = 1.8\,\mathrm{mV} \qquad 4.6.17$$

using the average standard deviation, and

$$V_{noise} = \frac{3.1 \times 10^{-3}}{\sqrt{10}} = 0.98\,\mathrm{mV} \qquad 4.6.18$$

using the minimum standard deviation. Both of these values will be used in Section 4.8 in the discussion of the *pwv* resolution of the radiometer.

As a final note, the 0.575 V subtracted from all datasets to account for the optical spillover (Section 4.6.1) was determined from the average of the signals from the LN_2 reference, V_{LN_2}, shown in the lower left hand graph of Figure 4.7.

4.7 Characterization of Instrument Field of View

The moon was visible on every evening of the observing run, and normally, care was taken to avoid the vicinity of the moon when taking observations. On the evening of Friday, Dec. 17, however, the instrument was deliberately made to scan across the moon

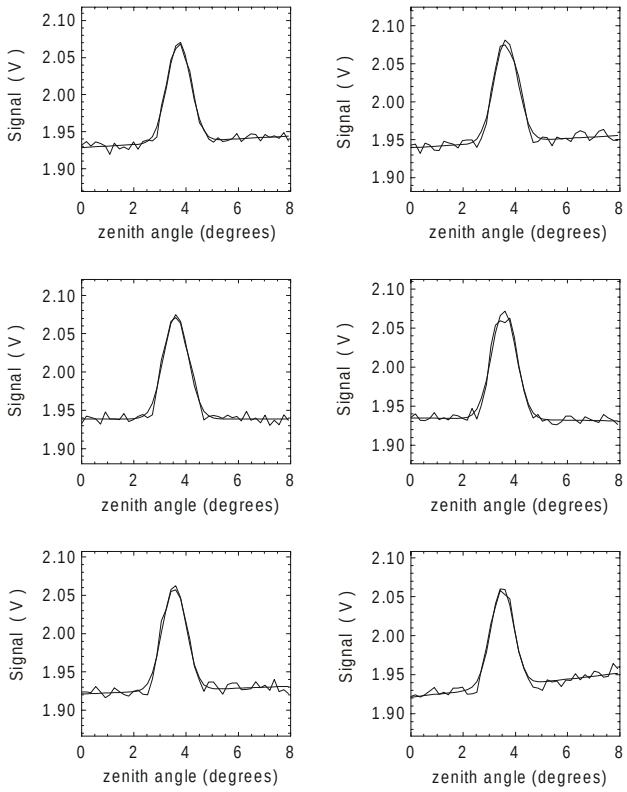

Figure 4.8: Gaussian fits to the moon scans produced by IDL.

in an attempt to determine the field of view of the instrument. These data were obtained using the *continuous scan* mode of operation and the results recorded in file 51a.

The full moon subtends an angle of $\sim 0.5^o$. The moon was approximately half full, however, during the observation and thus it did not represent a uniformly illuminated source. The data obtained from the moon scans represent a convolution of the instrumental field of view (FOV) with the moon. These scans appeared Gaussian in shape as shown in Figure 4.8. For simplicity, therefore, it was assumed that both the beam profile of the radiometer and the moon were Gaussian in shape. Since the convolution of two Gaussian profiles

Table 4.4: Results of the IDL Gaussian fit program.

Scan number	FWHM (degrees)
1	1.05
2	1.07
3	1.10
4	1.12
5	1.07
6	1.12
average	1.09

produces another Gaussian profile, with a resulting FWHM obtained by a quadrature sum of the component FWHM's, it was a simple matter to extract the beam profile from the data. An IDL routine (*Moon_Scan*) was written to extract the moon scan data from file 52 and fit a Gaussian+linear profile to the six individual scans. Figure 4.8 shows the original scans and the Gaussian+linear fits. The resulting FWHM's are summarized in Table 4.4, and include an average value.

The FWHM of the instrument was determined to be

$$FWHM_{inst} = \sqrt{FWHM^{\,2}_{data} - FWHM^{\,2}_{moon}}$$
$$= \sqrt{1.09^2 - 0.5^2} = 0.97^o \qquad 4.7.1$$

As the optical system was designed to have a FOV of $\sim 0.5^o$ (1/117 rad, Section 3.4.1), the measured FOV of 0.97^o indicated that the instrument was slightly out of focus. As discussed in Section 3.4.6, the focus of the instrument was determined by placing a hot copper plate of diameter 150 mm at a distance of $\sim$ 4 m followed by maximization of the output signal by adjustment of the X-Y dewar platform. Due to the low F number of the

parabolic mirror, this process was prone to small errors in dewar placement. It was only in the subsequent data analysis that this focus error was discovered. In retrospect, a larger source−radiometer distance should have been used. Since, however, the result of being slightly out of focus was to sample a slightly larger patch of atmosphere than was intended, this did not seriously impact the project.

4.8 Analysis of Continuous Scan Data

As described in Section 2.4.1, a *curve-of-growth* represents the spectrally integrated emission from an absorbing molecular species as the total amount of that species is varied in a known way. *Continuous scan* datasets obtained by the prototype radiometer were in the form of signal voltage vs. airmass (after conversion of the zenith angles). In order to produce *curves of growth* from these datasets, it was necessary to rescale the horizontal axes (parametrized from $1-3$) to reflect the absorber amount in the atmosphere at the time of observation. This was done by establishing a relation between the observed airmass, A, and the absorber amount, u, in units of $\mathrm{kg\,m^{-2}}$. In the case of atmospheric water vapor, when $A = 1$, the radiometer was viewing the zenith and the absorber amount, u, becames the vertical water vapor *column abundance*, w, in units of $\mathrm{kg\,m^{-2}}$, or, equivalently, *millimeters of precipitable water vapor*, (mm *pwv*).

At any moment the total absorber amount, u, viewed by a radiometer is

$$u = \int_0^\infty \rho(l)\, dl \qquad 4.8.1$$

If the atmosphere can be considered to be horizontally homogeneous and plane parallel then the integrated absorber amount along any line-of-sight, at any given instant, is equal to that integrated along the zenith multiplied by the current airmass,

$$u = wA \tag{4.8.2}$$

The signal voltage, V, from a radiometer, in the general case, can be written as

$$V = G(u) = G(wA) \tag{4.8.3}$$

where w represents the current value of column abundance and G is, in general, a non-linear function representing the integrated radiance due to a given absorber amount, u. For a single emission line, for example, G is the Ladenberg-Reiche function (equation 2.3.49) whose non-linearity represents the transition from a weak to a saturated regime as depicted in Figure 2.9. When many lines, of varying strength, are considered, G has no analytical representation. Nonetheless, G would be expected to have the same general form as Figure 2.9, as evidenced by the experimentally obtained data in the lower graph of Figure 4.5.

As seen from equation 4.8.3, the radiometer output signal is a function of the product of w and A, and is therefore insensitive to how this product is distributed among w and A. Consider two different atmospheric conditions represented by column abundances w_1 and w_2, where $w_2 > w_1$. *Continuous scan* datasets obtained under these two conditions can be written, using equation 4.8.3, as

$$V_1 = G(u_1) = G(w_1 A) \tag{4.8.4}$$

$$V_2 = G(u_2) = G(w_2 A) \tag{4.8.5}$$

where A is the same in both cases since both datasets were necessarily obtained over the same range of zenith angles. If the datasets were each acquired over a short time interval then w_1 and w_2 can be considered as constants and hence V_1 and V_2 are functions of A alone. As far as the radiometer is concerned, the second of these equations could be written as

$$V_2 = G(u_2) = G(w_1 \times \tfrac{w_2}{w_1} \times A) = G(w_1 A') \qquad 4.8.6$$

where $A' > A$ since $w_2 > w_1$. *Continuous scan* datasets obtained under different column abundance conditions, but over an identical airmass range, can thus be interpreted as having been obtained under the same column abundance conditions but over a larger airmass range. The two datasets lie vertically displaced from one another when plotted on the same graph with the common airmass parameter, A, on the horizontal axis (see Figure 4.5). In light of the above discussion, either one of the two datasets can then be rescaled horizontally to coincide with the *curve-of-growth* of the other.

This process may then be applied to many datasets obtained over a wide range of conditions. The vertically displaced curves, plotted on a common graph, could then be interpreted as being different components of a single *curve-of-growth*, obtained by expanding the horizontal scales of subsequently higher curves to produce an overlap with the next lower curve. This observation then suggests that all *continuous scan* datasets, obtained over an airmass range of $1-3$, but at times corresponding to different vertical water vapor column abundance, may alternately be viewed as parts of a single *curve-of-growth.* The horizontal (*pwv*) range of this composite *curve-of-growth* extends from a minimum equal to the lowest atmospheric column abundance encountered over the observing run (times

one) to a maximum equal to the highest atmospheric column abundance encountered times three.

For example, consider two datasets representing atmospheres with column abundances of 1 and 2 mm *pwv*, respectively, as shown in Figure 4.9. The *continuous scan* datasets then lie vertically displaced from one another when plotted on a graph using airmass on the horizontal scale. When plotted using absorber amount on the horizontal axis, however, the first *continuous scan* dataset would have coordinates from 1 mm *pwv* to 3 mm *pwv*, and the second from 2 mm *pwv* to 6 mm *pwv*. It then follows that, if the upper dataset is rescaled horizontally, it can be made to overlap the first (lower) curve over the range of 2 to 3 mm *pwv*, as shown in the Figure 4.9. The range of overlap between any two datasets is then a reflection of the similarity of the atmospheric conditions during each measurement.

4.8.1 Creation of a Composite *Curve-of-Growth*

Many of the data sets produced a *curve-of-growth* that deviated markedly from the smooth and featureless curves expected from a homogeneous atmosphere. From the data record, seven *continuous scan* datasets (data files 21, 22, 41, 44, 45, 50 and 60) were chosen to generate a composite *curve-of-growth*. These datasets were first plotted on the same graph to ensure that the highest signal voltage on any given curve was higher than the lowest signal voltage of the curve immediately above it, and would therefore, with proper scaling, overlap to a reasonable degree. When plotted using the common airmass

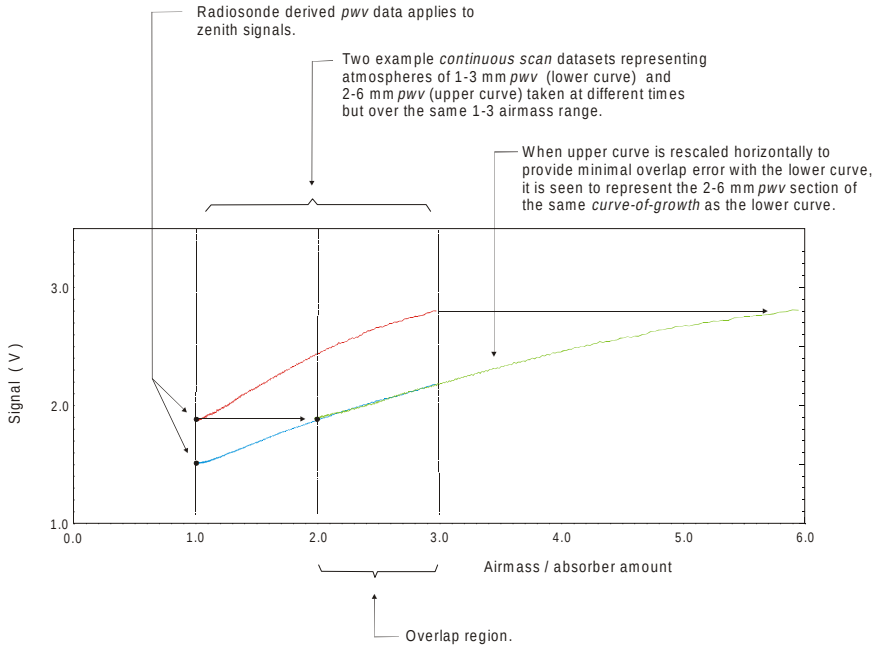

Figure 4.9: Two *curves-of-growth,* representing different states of the atmosphere but taken over the same airmass range, can be interpreted as as components of a single *curve-of-growth* over an extended airmass range. If the lower curve is assumed to have been obtained during conditions of 1 mm *pwv*, then the airmass values of the horizontal axis are equivalent to absorber amount in mm *pwv.*

coordinate, A, each dataset is represented by

$$V_n = G(w_n\, A) \tag{4.8.7}$$

The procedure to construct the composite *curve-of-growth* begins by leaving the lowest curve undisturbed; this dataset can be represented as

$$V_1 = G(w_1\, A) \tag{4.8.8}$$

After the process of stretching each subsequently higher dataset horizontally, to produce an overlap with the previous one, the second curve is described by

$$V_2 = G(w_1\, \tfrac{w_2}{w_1}\, A) \tag{4.8.9}$$

and the n^{th} dataset of the composite curve is

$$V_n = G(w_1 \frac{w_2}{w_1} ... \frac{w_n}{w_{n-1}} A) \qquad 4.8.10$$

The horizontal stretching factor connecting any dataset to its predecessor is the ratio of the (unknown) column abundances of the atmosphere at the time of their acquisition. From equations 4.8.9 and 4.8.10 it is seen that the composite *curve-of-growth* relates the radiometer signal under column abundance conditions from a minimum of $w_{\min} = w_1$ to a maximum of

$$w_{\max} = w_1 \times \frac{w_2}{w_1} ... \frac{w_n}{w_{n-1}} \times 3 \qquad 4.8.11$$

To construct the composite *curve-of-growth* from the seven selected datasets, an IDL routine (*Stretch_and_Splice*) was developed to determine the scale factors connecting any two datasets. The transformation of the uniformly-spaced zenith angles into airmass ($A = 1/\cos(\text{zenith angle})$) results in *continuous scan* data which lie on a nonuniform grid. Furthermore, the stretching of the individual curves in the generation of the composite *curve-of-growth* further distorts the grid of airmass values. To facilitate the numerical procedure, each *continuous scan* dataset was first re-gridded onto a uniform airmass grid, of spacing $\Delta A = 0.01$, using spline interpolation. Inspection of the *continuous scan* datasets showed that, when combined, the composite *curve-of-growth* covered a range from 1 to ~ 10 airmasses; the grid range for the *Stretch-and-Splice* routine was chosen to be $0 - 10$.

The scaling factor between any two successive curves, $\frac{w_n}{w_{n-1}}$, was found by iteratively adjusting a trial scaling factor, f, to minimize the overlap error given by

$$\chi^2 = \frac{\sum [\, a(i) - b(j) \,]^2}{N} \qquad 4.8.12$$

where $a(i)$ are the signal data of the lowest curve of the pair (taken as the reference for the *Stretch-and-Splice* procedure), $b(j)$ are the signal data of the upper curve and N is the number of grid points in this region. The summation is taken over the overlap region of the two curves ($i \equiv j$). For the case of data taken over an airmass range of $1-3$, and a grid spacing of 0.01, equation 4.8.12 becomes

$$\chi^2 = \frac{\sum_{100f}^{300} [\, a(i) - b(fi) \,]^2}{(3-f)100} \qquad 4.8.13$$

The scaling factor, f, was varied over a range from 1 to 3, in steps of 0.01, and the corresponding χ^2 was evaluated at each step. The scale factor corresponding to the minimum χ^2 value then becomes $\frac{w_n}{w_{n-1}}$. Figure 4.10 shows a screen shot of the IDL program executing the above procedure for two successive curves. The upper left graph shows two raw continuous scan datasets plotted over the $1-3$ airmass range (where a is the lower reference curve and b is the upper curve). In the upper right graph, curve b has been rescaled by increasing amounts. The χ^2 of the overlap region (equation 4.8.12) is shown in the lower left graph and exhibits a well defined minimum. The lower right graph shows curve b over-plotted with curve a using the scaling factor $f = \frac{w_n}{w_{n-1}}$, corresponding to the minimum χ^2 value. Also shown in this figure is the overlap error between curves a and b, multiplied by a factor of 10, and offset vertically by 2 V.

Repeating the above process on curve-by-curve basis resulted in the generation of a single, composite *curve-of-growth,* representing the full range of atmospheric conditions encountered during the observing run. Figure 4.11 shows the final composite curve and is

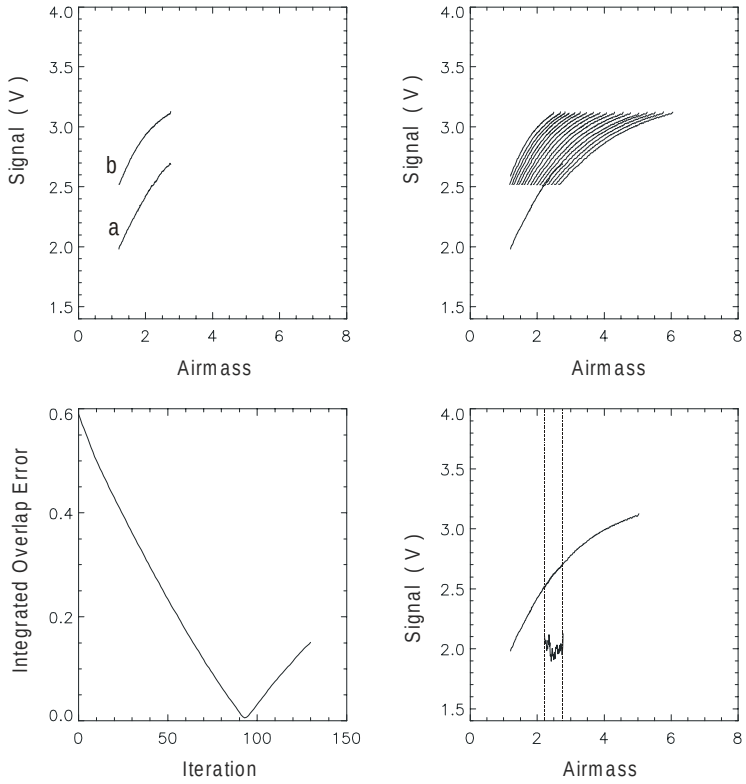

Figure 4.10: A screen shot of the IDL procedure *Stretch_and_Splice* iteratively adjusting the horizontal scale factor of the upper *continuous scan* dataset to produce the best overlap with the lower dataset. Upper left graph shows the two datasets as obtained over the same 1-3 airmass range but representing different column abundances. Upper right graph shows the iterative horizontal rescaling of curve b. Lower left graph shows the overlap error with a well defined minimum. Lower right graph shows the spliced curves, the overlap region and the overlap error within this region (multiplied by 10 and displaced vertically by 2 V).

seen to be composed of several re-scaled individual *continuous scan* datasets. Two of the component curves in the figure (purple and blue) have been displaced vertically by ± 0.05 V to show more clearly the regions of overlap. The red curve has been left undisturbed and extends to the maximum value of 10 airmasses.

Finally, a Chebyshev polynomial was fitted to this composite *curve-of-growth*, and included the point (0,0). A Chebyshev polynomial was chosen because of its ability to

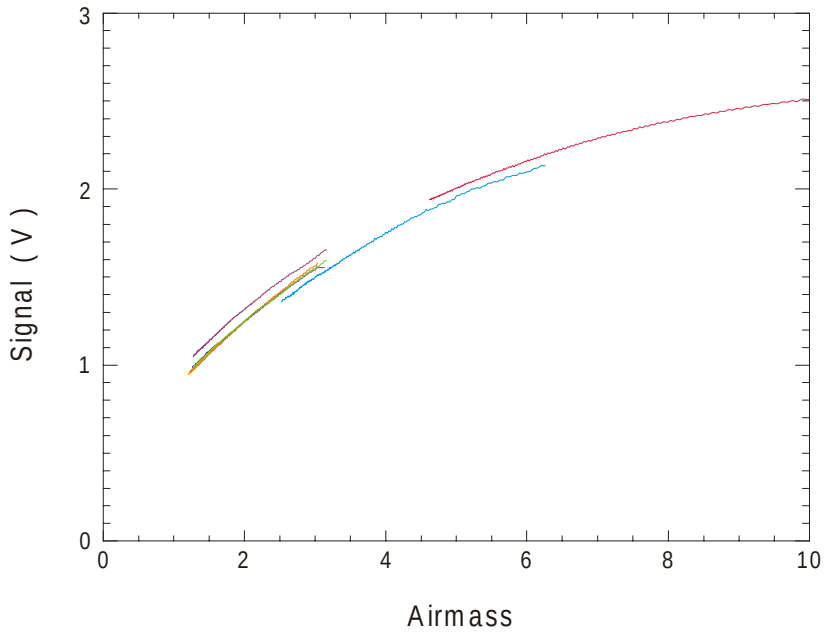

Figure 4.11: The composite curve is constructed fron seven individual curves. The purple and blue components were displaced upward and downward, respectively, by 0.05 V for clarity. The red component lies undisturbed on the *curve-of-growth* profile.

provide a higher order fit than can be obtained using standard polynomial fitting routines which tend to diverge. Furthermore, the Chebyshev polynomial can be easily differentiated to provide the radiometer column abundance resolution.

4.8.2 Calibrating the Composite Curve

At this point, the composite *curve-of-growth* gives the radiometer signal voltage function as a function of airmass. If column abundances, w_n, were measured by an independent means at the time each dataset was acquired, then the horizontal axis of each dataset, and hence the composite curve as a whole, could be rescaled from airmass into absorber amount using $u_n = w_n A$. Each dataset would then become a calibrated *curve-of-growth*

relating radiometer voltage to column abundance over the range w_n to $3\,w_n$, i.e.,

$$V_n = G(u_n) \tag{4.8.14}$$

Three independent methods of determining the water vapor column abundance were available. The first method was to use data from the simultaneous observation of water vapor emission with the 183 GHz JCMT water vapor monitor discussed in Section 4.5.3. The advantage of this method was that the data represented observations from essentially the same atmosphere at the same time. The disadvantage was that the calibration of the 183 GHz radiometer was uncertain.

The second method was to use measurements of atmospheric opacity as recorded by the California Submillimeter Observatory (CSO). The CSO has two monitors of atmospheric opacity, one operating at 225 GHz and another at a wavelength of 350 μm. Previous work has shown that a simple relation exists between the atmospheric opacity at 225 GHz, τ_{225GHz}, and the column abundance of water vapor, w, in mm pwv [18]:

$$w = 20(\tau_{225GHz} - 0.016) \tag{4.8.15}$$

Unfortunately, the 225 GHz monitor was not operational during the observing run. The 350 μm monitor was, however, operational during this period, and Dr. Richard Chamberlin has kindly made this data available to us. Information regarding the CSO monitors is available at http://puuoo.submm.caltech.edu/, where it is shown that

$$\tau_{350\mu m} = 23 \times \tau_{225GHz} \tag{4.8.16}$$

and thus equation 4.8.15 becomes

$$w(\mathrm{mm}\,pwv) = 20\,(\tfrac{\tau_{350_{\mu m}}}{23} - 0.016) \qquad 4.8.17$$

While the CSO opacity measurements, like those of the 183 GHz monitor, are obtained from the summit of Mauna Kea, there are two principal disadvantages to their use as calibration points: the measurements are obtained from a fixed azimuthal angle (different from the data obtained with the prototype) and are provided at 20 minute intervals.

The third method was to use data provided by the radiosondes launched twice daily from Hilo airport at 0:00 and 12:00 UT (2:00 p.m. and 2:00 a.m. LHT). There are three principal disadvantages of radiosonde measurements: they occur only once a night, the launch site is $\sim$ 43 km to the east of the summit of Mauna Kea and, more importantly, they tend to carry moisture aloft from the tropical launch site which tends to yield elevated column abundance data.

In light of the above, it was decided to calibrate the prototype radiometer using the data obtained from the 183 GHz monitor. Data from the other two methods, being of a more questionable nature, were used to confirm the calibration. The red curve in Figure 4.12 shows the Chebyshev-fitted composite *curve-of-growth.* This curve was transformed into a calibrated *curve-of-growth* by rescaling its horizontal axis to provide consistency with lowest of the 183 GHz calibration points given in Table 4.2 (represented by the lower red square) and resulted in the blue curve in Figure 4.12. The second independent 183 GHz calibration point from Table 4.2 is seen to fall directly on the calibrated curve. The horizontal axis calibration scale factor used to transform airmass into column abundance was

$$w = 0.616\,A \qquad 4.8.18$$

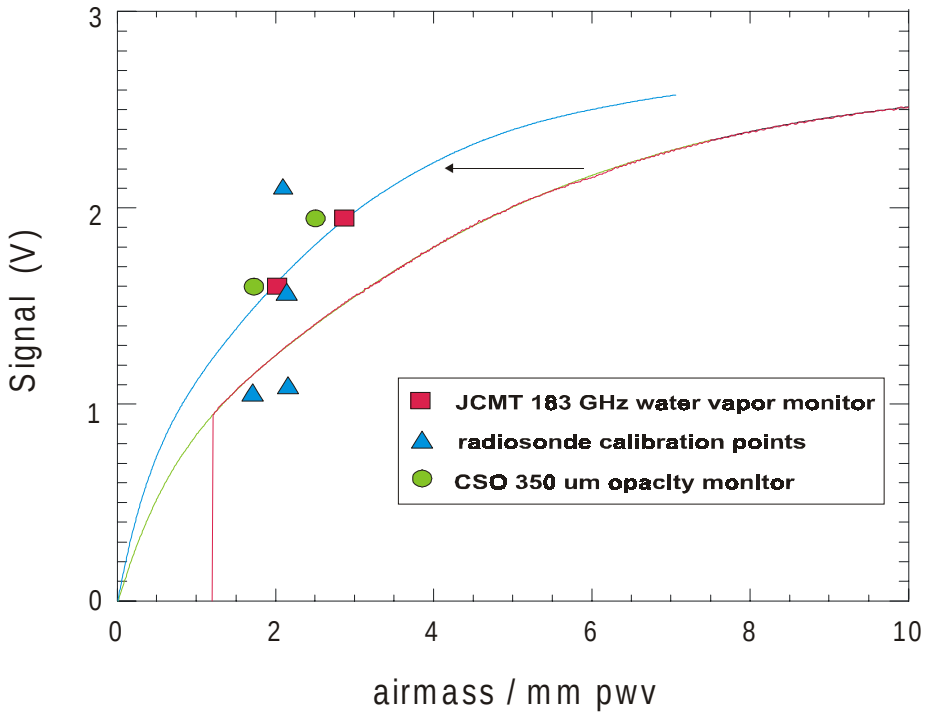

Figure 4.12: Calibration of the composite curve-of-growth in terms of pwv. The red curve is the Chebyshev-fitted composite curve representing an airmass range from 1-10. The green portion of this curve is an extrapolation into a low column abundance region unobserved at Mauna Kea. The blue curve is the Chebyshev-fitted composite curve rescaled horizontally to be consistent with the 183 GHz calibration data. The CSO 350 μm calibration points are seen to suggest a slightly lower column abundance calibration than that of the 183 GHz. The radiosonde data suggests the opposite.

and the nearness of this scale factor to unity allows the same horizontal scale to be used for both airmass and column abundance (in mm pwv) in Figure 4.12.

The CSO 350 μm data, corresponding to the times of the two 183 GHz calibration measurements in Table 4.2, were converted to mm pwv using equation 4.8.17. The resulting values of 1.73 and 2.50 mm pwv, obtained at 9:20 and 9:40 p.m., LHT, December 17, corresponded to radiometer signal voltages of 1.61 V and 1.94 V, respectively. These two data points are plotted in Figure 4.12 as green circles and show good agreement with the 183

GHz data. In fact, the composite *curve-of-growth* could equally have been calibrated using these two data points had they been of less questionable quality.

Finally, the radiosonde calibration data are displayed in Figure 4.12 as blue triangles. Only data obtained near the end (∼midnight) of the five observing sessions could be expected to reasonably correlate with the *pwv* readings from the radiosonde launched two hours later. Furthermore, on only four of these occasions was the stability of the atmosphere (as revealed by the consistency of successive *continuous scan* datasets obtained at the end of the night) sufficient to justify the use of radiosonde data. These four data points show a wide scatter and a trend toward a larger column abundance than that indicated by the JCMT and CSO data. It was later discovered that the model of radiosondes launched from Hilo are among the oldest in use in the United States and, due to their capacitive sensors, tend to carry moisture up from lower altitudes. The scatter shown by the radiosonde points underline the need for the accumulation of a large database of radiosonde data if these are to be used for calibration purposes.

The (optional) final step in the calibration process was to transform the signal axis into radiance via division by the responsivity (equation 4.6.16). The result is the *curve-of-growth* shown in Figure 4.13 with units of radiance on the vertical axis. Due to the effects of the optical spillover identified in the prototype (Section 4.6.1), the responsivity calculated in Section 4.6 is unreliable and hence the radiance given on the vertical axis in Figure 4.13 is only approximate. For this reason the column abundance resolution of the prototype radiometer will be calculated using the derivative of the calibrated composite *curve-of-growth* expressed in terms of signal voltage.

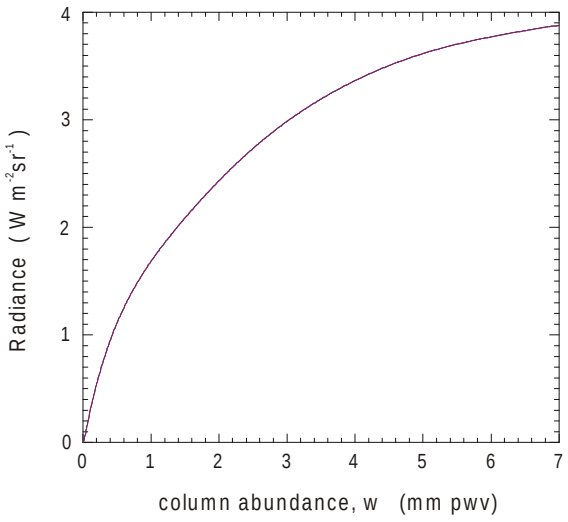

Figure 4.13: The composite curve-of-growth in the form of column abundance vs. radiance.

4.8.3 Prototype Performance

The slope of the calibrated composite *curve-of-growth* (blue curve in Figure 4.12) was then used to derive the column abundance resolution of the prototype radiometer by projecting the voltage noise of the instrumentation onto the column abundance axis using the slope of the *curve-of-growth*. Since the derivative is a function of column abundance, the performance of the radiometer is also a function of column abundance. Clearly, therefore, the best performance of the prototype will be obtained at low column abundance levels where the derivative is large. Figure 4.14 shows a plot of this derivative.

Since the infrared radiometer is intended for use at high altitude observatories, the column abundance resolution performance of the prototype will be evaluated for column abundances of 0.5 and 1.0 mm pwv. Furthermore, since there was reason to believe that

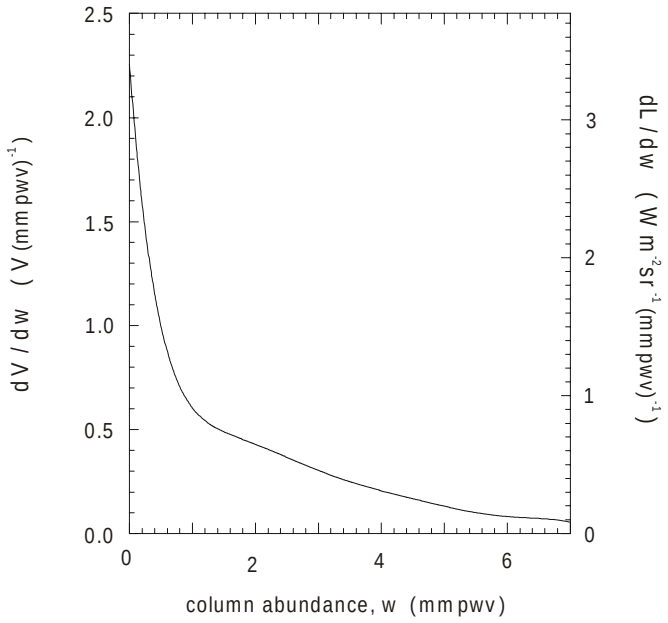

Figure 4.14: The derivative of the calibrated *curve-of-growth* given in terms of both dV/ dw and dL / dw. The evaluation of the performance of the prototype radiometer uses values of the derivative at 0.5 and 1.0 mm *pwv*.

the minimum rather than the average instrumental noise represents the true noise performance of the prototype, as discussed in Section 4.6.3, the instrumental performance will be evaluated using both of these values. From equations 4.6.17 and 4.6.18, the average and minimum instrumental noises for a 1 s integration are, respectively,

$$\Delta V_{av} \ = 1.8 \times 10^{-3} \ V \tag{4.8.19}$$

$$\Delta V_{\min} = 0.98 \times 10^{-3} \ V \tag{4.8.20}$$

The derivative of the composite *curve-of-growth* at column abundances of 0.5 and 1.0 mm *pwv* are, respectively,

$$\tfrac{dV}{dw}(0.5 \,\mathrm{mm}\, pwv) = 0.99 \ V \,(\mathrm{mm}\, pwv)^{-1} \tag{4.8.21}$$

$$\tfrac{dV}{dw}(1 \,\mathrm{mm}\, pwv) = 0.60 \ V \,(\mathrm{mm}\, pwv)^{-1} \tag{4.8.22}$$

Table 4.5: Summary of the water vapor column abundance resolution of the prototype radiometer (using 1 s integrations) for atmospheric conditions of 0.5 and 1.0 mm pwv.

atmospheric column abundance condition	0.5 mm pwv	1.0 mm pwv
resolution using average instrumental noise	1.8 μm pwv	3.0 μm pwv
resolution using minimum instrumental noise	1.0 μm pwv	1.6 μm pwv

Table 4.6: Summary of the resolution of the prototype radiometer in terms of the excess electromagnetic path length (using 1 s integrations) for atmospheric conditions of 0.5 and 1.0 mm pwv.

atmospheric column abundance condition	0.5 mm pwv	1.0 mm pwv
resolution using average instrumental noise	12 μm	20 μm
resolution using minimum instrumental noise	6.4 μm	11 μm

The column abundance resolution of the prototype radiometer is then calculated by

$$\Delta w = \frac{\Delta V}{\frac{dV}{dw}} \tag{4.8.23}$$

using the values given in equations 4.8.19 - 4.8.22. These results, collected in Table 4.5, summarize the pwv measurement resolution of the prototype radiometer using 1 s integrations.

As discussed in Section 1.2, a factor of 6.5 is used to convert the column abundance resolution, Δw, into excess electromagnetic path length resolution, Δd, where the units of w and d are the same. A summary of the excess electromagnetic path length resolution of the prototype, using 1 s integrations, is given in Table 4.6.

It is seen from this table that the target electromagnetic path length resolution set out for ALMA has been achieved by the prototype radiometer for atmospheric column

abundance conditions below 1 mm pwv if the minimum instrumental noise is taken as its true noise performance.

4.8.4 Cloud Bank Evolution

Among the *continuous scan* datasets displaying artifacts or other anomalous structures was a dataset taken in the early evening just after sunset, that recorded the time evolution of a significant cloudbank as it passed over Mauna Kea and moved to the west. The clouds were much lower and thicker than the cirrus observed at other times.

Figure 4.15 shows this data as a 3-D plot and indicates the time order of the scans. The features in the data seem to dissipate and reassemble more so than moving as a whole. The cloud bank was composed of more than one structure; it is seen to be an evolving entity with structures that can evaporate and reform in directions opposite to the overall motion. These scans again used a sampling time of $0.1\,s$ and a single scan took on the order of 30 seconds to complete. The elapsed time from scan 1 to 10 was then ~ 5 minutes.

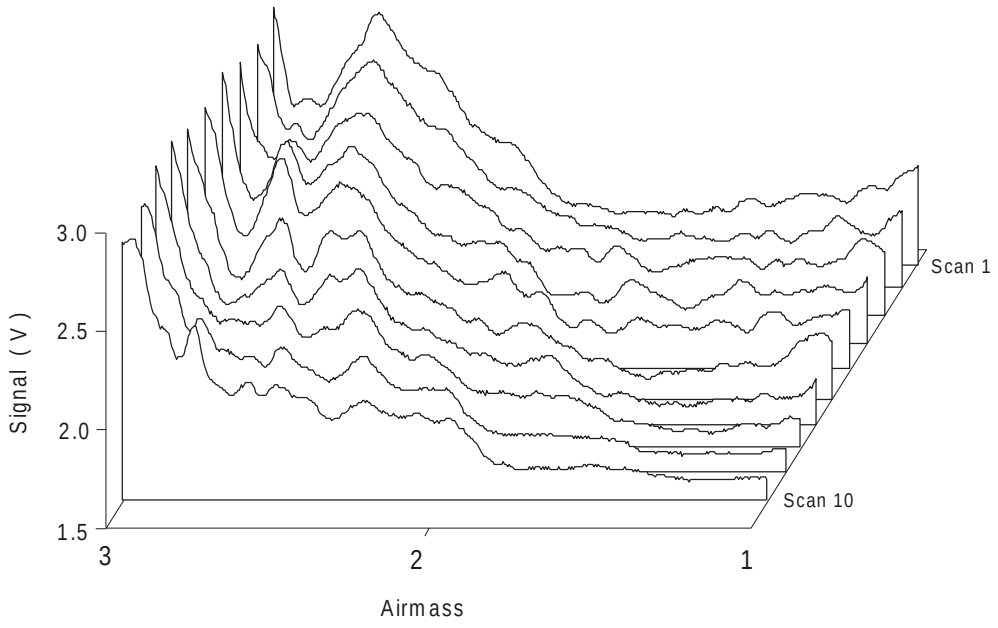

Figure 4.15: The time evolution of a cloud bank as revealed by ten consecutive *continuous scans*.

Chapter 5

Conclusions and Future Directions

This thesis has presented the design, construction and results from the first field test of a prototype infrared radiometer designed to measure, both rapidly and accurately, the water vapor column abundance above high altitude sites. The prototype system provided a proof-of-concept of an infrared approach to water vapor column abundance measurement.

The results presented in Chapter 4 show that, under conditions of 1 mm *pwv*, which represents the average column abundance at the Chajnantor site, the prototype has shown the ability to resolve at least ± 3 μm *pwv* ($1\,\sigma$ in a 1 s integration), equivalent to ± 20 μm of excess electromagnetic path length. As discussed in Section 4.6.3, there is good reason to believe that the resolution of the prototype is closer to ± 1.6 μm *pwv* ($1\,\sigma$ in a 1 s integration), equivalent to ± 11 μm of excess electromagnetic path length. These results already virtually meet the challenging requirements for phase correction of the new generation of radio interferometers such as ALMA. More impressive is the fact that they were obtained on the trial run of a new methodology.

These encouraging results have provided the impetus for further development of this technique. Several areas of improvement identified during the course of this thesis have been incorporated into a second generation (Phase II) instrument named *IRMA* - an Infrared Radiometer for Millimeter Astronomy. These improvements, and their impact on instrument performance, are discussed in this chapter.

5.1 Improved Detector

A new mercury-cadmium-telluride infrared detector has been obtained from Kolmar Technologies Inc., identical to the earlier detector, but having a higher detectivity and responsivity, 5.11×10^9 cm Hz$^{-1/2}$ W^{-1} and 136 V W^{-1}, respectively, compared with 2.88×10^9 cm Hz$^{-1/2}$ W^{-1} and 45 V W^{-1} in the earlier detector. The signal-to-noise ratio of an infrared detector is defined as

$$\frac{S}{N} = \frac{PD^*}{\sqrt{A}} \qquad 5.1.1$$

where P is the input signal power, D^* is the specific detectivity and A is the detector area. The expected signal-to-noise improvement is then

$$\frac{S/N\,(new)}{S/N\,(old)} = \frac{5.11\times10^9}{2.88\times10^9} = 1.77 \qquad 5.1.2$$

The noise voltage density of the new device is

$$e_n = \frac{R_{new}\sqrt{A}}{D^*} = \frac{136(0.1)}{5.11\times10^9} = 2.7\,\text{nV Hz}^{-1/2} \qquad 5.1.3$$

but since this detector noise is specified at 10 kHz, the corresponding value at 200 Hz will be higher. As was shown in Section 3.4.8, the dominant source of noise in the preamplifier

circuit was that due to the LT 1028 op-amp ($1\,\mathrm{nV\,Hz^{-1/2}}$); it should thus be easier to achieve detector limited performance in the new system.

5.2 Improved Infrared Filter

Infrared filters are notoriously difficult to fabricate for use at $\sim 20\,\mu$m. The filter used in the prototype was not an optimal match to the spectral region of interest, but was the only one available. Professor Peter Ade, Queen Mary and Westfield College, University of London, UK, has recently extended his filter fabrication technology from $\sim 50\,\mathrm{cm^{-1}}$ to $\sim 500\,\mathrm{cm^{-1}}$. While still in the development phase, Dr. Ade has provided two filters using resonant capacitive and inductive micro-elements that provide a better match with both the new detector and the spectral region of interest. The higher efficiency ($\sim 80\%$), and better band selection, are expected to provide at least a factor of two improvement in detection efficiency over the prototype instrument.

5.3 Improved Instrumentation

The improvements in electronic instrumentation include the use of a 24-bit, delta-sigma A/D converter which is currently operated at an equivalent 18 bit resolution with a 0.3 s integration time. With a voltage reference of 2.5 V, 1 LSB corresponds to a voltage of 9.5 μV. Recent results from *IRMA* show that the currently observed noise floor of the instrumentation is approximately 250 μV in a 0.3 s integration and typical maximum signals

(from the ambient blackbody) are on the order of 2.4 V. Compared with the corresponding prototype measurements, the result is an approximately seven-fold increase in signal-to-noise.

The malfunctioning temperature sensor circuitry has been replaced and currently provides temperature readings with an accuracy of $\pm 0.1\,\mathrm{K}$.

5.4 Elimination of Optical Spillover

The optical spillover of the LN_2 blackbody (Section 4.6.1) occurring in the prototype has been corrected by use of a larger flask. The signals from the LN_2 blackbody observed with the lock-in amplification in *IRMA* actually reverse in polarity when this source is viewed and hence indicate that the LN_2 flask appears colder than a reflected view of the detector environment. These signals lie near the noise floor of the instrumentation ($250\,\mu\mathrm{V}$) and hence provide a well defined and stable calibration point.

5.5 Remote Operation

The most dramatic improvement of the prototype radiometer has been the implementation of web based control. *IRMA* has now been installed, semi-permanently, on the apron of the JCMT and is remotely operated over the web from Lethbridge. This remote, and automatic, control of *IRMA* enables the instrument to collect water vapor measurements simultaneously with radiosonde launches and thus Phase II will include the

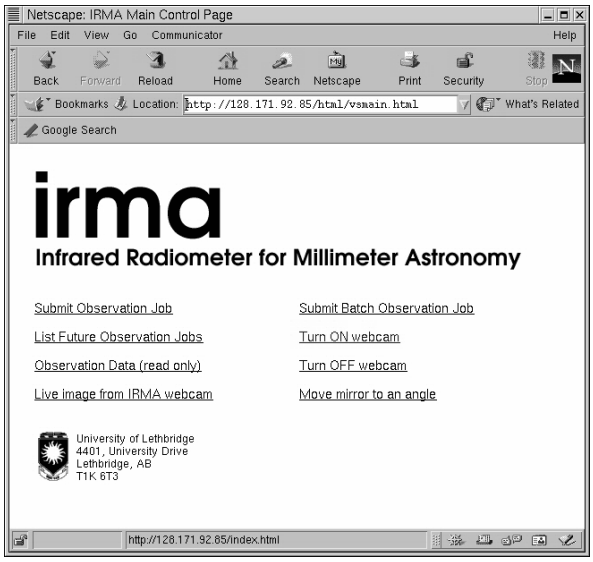

Figure 5.1: The web based remote control interface for IRMA.

compilation of a large database of radiosonde-correlated measurements. In addition, measurements from the JCMT 183 GHz water vapor monitor, CSO 225 GHz / 350 μm opacity monitor and SCUBA sky-dips, will also be included in this database.

IRMA was deployed in late August, 2000, and operates on any night that the JCMT is open for operation and the CSO opacity monitor indicates less than 2 mm pwv. *IRMA* can be scheduled to perform *continuous scan*, *skydip*, *stare* or *calibration* measurements, or any combination thereof, as either a single or multi-component observation. Currently, the biggest drawback to operation is the requirement for a telescope operator to fill the detector dewar every few hours. In the Phase III development, which will begin in early 2001, closed cycle refrigeration will be incorporated into the *IRMA* design, obviating the need for cryogens. Two such units will be built for Phase III and it is anticipated that they will be mounted on two antennae of the Smithsonian Millimeter Array (SMA) allowing the

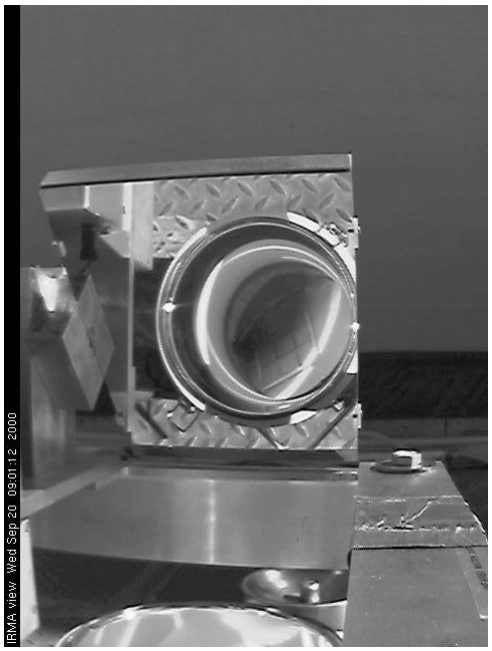

Figure 5.2: A view from IRMA's web-cam showing the LN_2 flask reflected in the downward facing scanning mirror.

infrared approach to phase correction to be tested, for the first time, on an astronomical source.

The website for *IRMA* is located at http://irma.jcmt.jach.hawaii.edu but, currently, a password is required for access. In future, the results from *IRMA* will be posted on the JCMT website. Figure 5.1 shows the web interface for IRMA and Figures 5.2 and 5.3 show views obtained by *IRMA*'s on-board 'web-cam'. The web-cam is oriented toward the JCMT antenna from IRMA's position on the apron and the $gortex^{TM}$ windscreen of the JCMT will be noticed in the background.

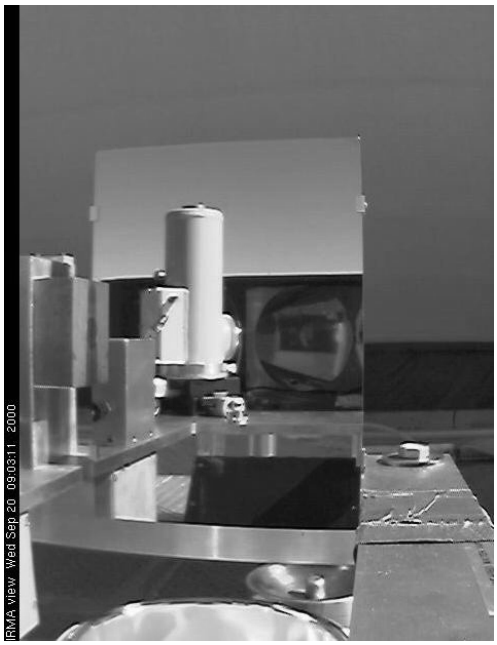

Figure 5.3: With the scanning mirror in the directly vertical position, a reflected image of the detector dewar is visible.

Chapter 6

CD ROM Software Archive

The CD ROM included with this thesis contains the IDL^{TM} analysis software, raw data files (in the form of IDL .sav files) and the C++ instrument control program (named 'Felix'). With the CD-drive designated as d:\, the directory structure is as follows

d:\IRMA

\IDL_Software

\Raw_Data

\Control_Program

\Felix

\includes

with the IDL procedures stored in the directory \IDL_Software, the raw data files in \Raw_Data and the control program in \Felix.

6.1 IDL Routines

Some of the IDL procedures stand alone, whereas others operate on raw data files (.sav files) which contain the data obtained with the prototype radiometer. The procedures that operate on *.sav* files contain a directory pathway in the IDL code that assumes that the CD-drive is designated as drive d:\. If the CD-drive designation is different, the programs will have to be changed accordingly. In order for the procedures to execute from the CD, the IDL search pathway, found in the 'file\preferences' menu within IDL, must include the directory pathway d:\IRMA\IDL_Software\. IDL version 5.2 is needed to run the procedures. Short descriptions of the IDL procedures referenced in the body of the thesis are given below.

6.1.1 *Planck_Power_*462_505, *Planck_Curves*, *Planck_Curves_X*, *Planck*

The procedure *Planck_Power_*462_505 evaluates the integrated radiance of a blackbody, in units of $\mathrm{W\,m^{-2}sr^{-1}}$, for a given blackbody temperature, over the passband of the prototype radiometer (i.e., $462 - 505\ \mathrm{cm^{-1}}$). The function *Planck_Curves* is used to plot the Planck radiance as a function of wavenumber for arbitrary number of curves and temperatures. The function *Planck* evaluates the spectral radiance for arbitrary wavenumber in units of $\mathrm{W\,m^{-2}sr^{-1}(cm^{-1})^{-1}}$ and is called as a function from *Planck_Curves*. A version of *Planck_Curves*, called *Planck_Curves_X*, is also included in the archive and is identical to the former except that it uses an XWindows graphical interface.

6.1.2 *Curve_of_Growth*

This procedure was used to simulate the *curve-of-growth,* obtained with a Lorentz broadened emission line, by calculating the integrated emission as a function of column abundance, ρl. The analysis also includes a calculation of the Ladenberg-Reiche formula, the theoretical form of the *curve-of-growth.*

6.1.3 *Parabola_Design*

This procedure was used to generate the optical design of the parabolic mirror and uses mirror diameter, angle of off-axis throw and focal length as input parameters.

6.1.4 *Extract_Data*

This procedure extracted data from files saved as $mkXX.sav$ where XX designates a *continuous scan* data file number. These *.sav* files are in the form of a structure (matrix) called *array*, and holds all the *continuous scan* data from a single session with zenith angles from 0^o to 70.38^o listed vertically in the first column (column 0) and each *continuous scan* dataset of the session listed in subsequent columns (columns 1 to *cols*). Blackbody measurements taken at the end of each *continuous scan* appear in the last two rows of this array at angles of 128^o and 180^o. Since a full *continuous scan* dataset consists of 391 readings (for a zenith angle range from 0^o to 70.38^o, in steps of 0.18^o), the array has dimensions of 393 rows $\times$ (number of *continuous scans* $+1$) columns.

The procedure *Extract_Data* combined all the *continuous scan* datasets within the session into a single averaged *continuous scan* dataset including the readings from the blackbody references. In addition, the routine calculated the standard deviations of all continuous scan/LN_2blackbody/ambient blackbody readings within the file. The procedure then produced another *.sav* file with the name *av_mkXX.sav* which consisted of an array identical to the original *mkXX.sav* array except with two additional columns containing the averaged data, and associated standard deviations, appended as $cols + 1$ and $cols + 2$.

6.1.5 *Responsivity*

This routine plots the file-by-file instrument responsivity and associated error calculated by *Extract_Data*.

6.1.6 *Stability_of_References*

This procedure plots the average and standard deviations of the signals from the blackbody references calculated in *Extract_Data*.

6.1.7 *Comparison_with_183GHz*

This procedure analyzed the data obtained simultaneously with the JCMT 183 GHz water vapor monitor. The procedure plots both datasets in their raw form, and with different amounts of smoothing. In addition, the procedure prints out the maximum and

minimum values of each dataset, i.e., corresponding values of prototype signal voltage and 183 GHz-derived pwv values.

6.1.8 *Moon_Scan*

This procedure was used to determine the field of view of the prototype radiometer by producing a Gaussian + linear fit for the datasets containing moon profiles.

6.1.9 *Best_Seven*

Seven *continuous scan* datasets were selected for use in the compilation of a composite *curve-of-growth.* These datafiles were numbers 21, 22, 41, 44, 45, 50 and 60. This procedure plots these selected datasets on a common graph.

6.1.10 *Stretch_and_Splice*

This procedure was central to the data analysis as it determined the scale factor between any two input datasets necessary to splice the datasets together as a single *curve-of-growth,* on a common airmass scale. The procedure takes in *continuous scan* .sav files two at a time and then stretches out the x scale factor of the higher of the two curves recursively to find the factor which produced the best spliced fit to the lower curve.

6.1.11 *pwv_Calibration*

This is the final analysis procedure and begins by assembling the various individual *continuous scan* datasets into a composite *curve-of-growth* using the scale factor determined by *Stretch_and_Splice*. A Chebyshev polynomial is then fitted to this composite curve. The pwv calibration data points derived from the JCMT 183 GHz water vapor monitor, the CSO 350 μm opacity monitor and radiosonde are then plotted on the same graph as the composite curve. The composite curve is then rescaled horizontally to agree with the lowest of the 183 GHz points listed in Table 4.2. Finally, the derivative of the rescaled composite curve is computed, which allowed the determination of the pwv resolution performance, Δw, of the prototype radiometer.

6.1.12 *cheby_calc*, *cheby_fit*, *cheby_der*

The IDL procedure *pwv_Calibration* fitted the composite curve to a Chebyshev polynomial using the function *cheby_fit*, which itself used the function *cheby_calc*. The derivative of the polynomial was calculated with the function *cheby_der*.

6.2 Control Program

While the C++ instrument control program is specific to the hardware used with the prototype instrument, and is therefore of limited usefulness, it is included in the software archive for completeness. It may be run for demonstration purposes provided nothing is

connected to the computer parallel port. The program will display the user interfaces discussed in Section 3.6, and will be fully operational, except that all analog data will be read and displayed as 4.096 V.

Bibliography

[1] C. L. Carilli and M. A. Holdaway, "Tropospheric Phase Calibration in Millimeter Interferometry," http://www.arXiv:astro-ph/9904248 (1999).

[2] M. Wiedner, *Atmospheric Water Vapour and Astronomical Millimeter Interferometry* (PhD Thesis, Cambridge, UK, 1998).

[3] J. Callaway, *Quantum Theory of the Solid State.* (Academic Press, London, 1991).

[4] D. C. Hogg, F. O. Guiraud, and M. T. Decker, "Measurement of Excess Radio Transmission Length on Earth-Space Paths," Astron. Astrophys. **95,** 304–307 (1981).

[5] O. P. Lay, "ALMA Memo number 209: 183 GHz Radiometric Phase Correction for the Millimeter Array," http://www.mma.nrao.edu/memos (1998).

[6] D. A. Naylor, R. T. Boreiko, T. A. Clark, R. J. Emery, B. Fitton, and M. F. Kessler, "Atmospheric emission in the 20-micron window from Mauna Kea," pasp **96,** 167–173 (1984).

[7] C. Carilli, O. Lay, and E. Sutton, "ALMA Memo 210: Radiometric Phase Correction," http://www.mma.nrao.edu/memos (1998).

[8] D. Delgado, A. Otarola, V. Belitsky, D. Urbain, R. Hills, and P. Martin-Cocher, "ALMA Memo 271.1: The Determination of Precipitable Water Vapor at Chajnantor from Observations of the 183 GHz Water Line," http://www.mma.nrao.edu/memos (1999).

[9] W. Wolfe, *Introduction to Radiometery* (SPIE Press, New York, 1990).

[10] G. Rybicki and A. Lightman, *Radiative Processes in Astrophysics* (John Wiley and Sons, New York, 1979).

[11] L. Rothman and et. al., "The HITRAN Molecular Spectroscopic Database, 1996 Edition," J. Quant. Spec. Rad. Trans. **60,** 665–710 (1998).

[12] K. Kondratyev, *Radiation in the Atmosphere* (Academic Press, New York, 1969).

[13] G. Herzberg, *Molecular Spectra and Molecular Structure Volume I* (Van Nostrand Reinhold, New York, 1950).

[14] E. McCartney, *Absorption and Emission by Atmospheric Gases* (John Wiley and Sons, New York, 1983).

[15] Eccosorb, Emerson and Cuming, 604W 182 St, Gardena, CA 90248, USA .

[16] P. Ade, "Private communication," (2000).

[17] Kolmar Technologies Inc., 1400 E General Arts Rd., Conyers, GA 30012, USA .

[18] G. R. Davis, M. J. Naylor, D. A. Griffin, T. A. Clark, and W. S. Holland, "Broadband Submillimeter Spectroscopy of HCN, NH_3 and PH_3 in the Troposphere of Jupiter," Icarus **130,** 387–403 (1997).